RESEARCH ARTICLE SUMMARY

MOLECULAR BIOLOGY

Gene syntax defines supercoiling-mediated transcriptional feedback

Christopher P. Johnstone, Kasey S. Love, Sneha R. Kabaria, Ross D. Jones, Albert Blanch-Asensio, Deon S. Ploessl, Emma L. Peterman, Rachel Lee, Jiyoung Yun, Conrad G. Oakes, Christine L. Mummery, Richard P. Davis, Brandon J. DeKosky, Peter W. Zandstra, Kate E. Galloway*

Full article and list of author affiliations: https://doi.org/10.1126/science.adw1925

INTRODUCTION: Native gene networks require coordination of multiple transcriptional units to robustly pattern cell fate. Although precise control of gene expression is crucial for this process, the coupling between closely colocalized genes, including both native regulatory circuits and size-limited, synthetic gene circuits, is not fully understood. We aimed to uncover how transcription of a single gene affects expression of adjacent genes through the over- and undertwisting of DNA caused by RNA polymerase motion. This twisting of DNA is known as DNA supercoiling and arises from the directionality of transcription. Supercoiling impacts transcription of adjacent genes by altering RNA polymerase binding, forming a feedback loop. Supercoiling has been studied in silico, in vitro, and genome wide, but perturbative, locus-specific supercoiling measurements in living cells are more difficult, limiting mechanistic dissection of this phenomenon and its impact on gene expression.

RATIONALE: We measured the impact of supercoiling on gene expression by building and integrating synthetic two-gene reporter circuits in mammalian cell lines. These synthetic circuits allowed us to probe how gene syntax, the relative order and orientation of genes, determines supercoiling-mediated feedback while holding gene identity, circuit copy number, genomic location, and other parameters constant. By inducing expression of one of the genes with a small molecule, we directly varied transcription-generated supercoiling. We measured single-cell protein and mRNA levels using flow cytometry, allowing us to calculate both the mean and variability of each reporter gene across a population of cells. Using circuits integrated at a fixed safe harbor locus, we quantified the local epigenetic state using CUT&Tag assays, the positive supercoiling density using GapRUN, and the chromatin folding behavior using Region Capture Micro-C. These measurements provided a high-resolution view of chromatin behavior at the circuit locus and the response to induction of the inducible gene.

RESULTS: We found that gene syntax shapes expression profiles in a syntax- and induction-dependent manner. Pairs of genes with divergent syntax show amplified, correlated expression, whereas pairs with tandem syntax have reduced expression from the downstream gene. These syntax-dependent behaviors generalize well across both integration method and cell type. Expression patterns also co-occur with changes in chromatin state. Both direct measurements of positive DNA twist and indirect correlates of chromatin structure suggest that supercoiling contributes to these syntax-dependent behaviors. Applying our observations to engineer synthetic circuits, we improved antibody production yield, tuned stoichiometric expression ratios, and optimized the function of all-in-one inducible circuits by changing only gene syntax.

CONCLUSION: Supercoiling-mediated feedback couples genes spaced within a few kilobases. This phenomenon may contribute to the coordination of native transcriptional programs. Applying the design rules suggested by our work can enhance the predictability, performance, and functional range of engineered gene circuits. □

*Corresponding author. Email: katiegal@mit.edu Cite this article as C. P. Johnstone *et al.*, *Science* **392**, eadw1925 (2026). DOI: 10.1126/science.adw1925

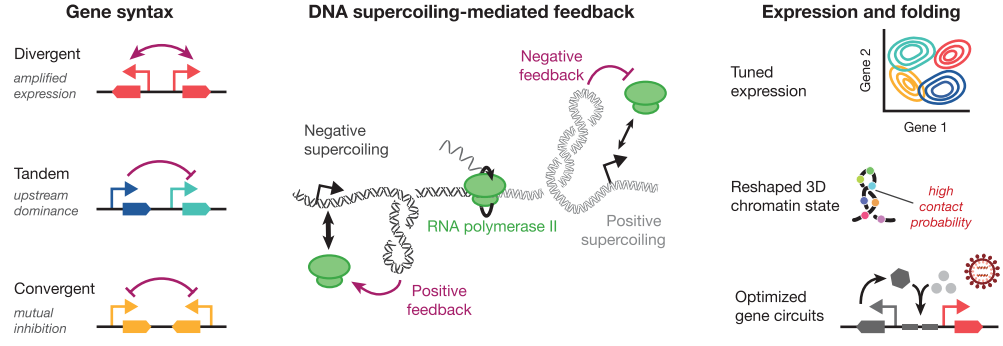

Supercoiling-mediated feedback and gene syntax couple the expression of adjacent genes. Supercoiling couples the motion of elongating RNA polymerases to the transcriptional initiation rate of adjacent genes. Influenced by this supercoiling-mediated feedback, the different gene syntaxes show distinct patterns of expression and chromatin states. Using supercoiling-informed design rules, engineered gene circuits can be optimized for robustness and performance. 3D, three dimensional.

MOLECULAR BIOLOGY

Gene syntax defines supercoiling-mediated transcriptional feedback

Christopher P. Johnstone[1], Kasey S. Love[2], Sneha R. Kabaria[1], Ross D. Jones[3,4], Albert Blanch-Asensio[1], Deon S. Ploessl[1], Emma L. Peterman[1], Rachel Lee[1], Jiyoung Yun[3,4], Conrad G. Oakes[5], Christine L. Mummery[6,7], Richard P. Davis[6,7], Brandon J. DeKosky[1,8], Peter W. Zandstra[3,4], Kate E. Galloway[1]*

Gene syntax—the order and arrangement of genes and their regulatory elements—shapes the dynamic coordination of both natural and synthetic gene circuits. Transcription at one locus perturbs the transcription of adjacent genes, but the molecular basis of this effect remains poorly understood. In this work, we show that supercoiling-mediated feedback arises from transcription and regulates expression of adjacent genes in a syntax-specific manner. Using a suite of assays, we measured syntax- and induction-dependent formation of chromatin structures in human induced pluripotent stem cells. Applying syntax as a design parameter, we built and improved compact gene circuits, tuning the expression mean, noise, and stoichiometry across delivery methods and cell types. Integrating supercoiling mediated feedback into models of gene regulation will expand our understanding of native and synthetic systems.

Native gene circuits coordinate transcriptional programs that orchestrate complex cellular processes across space and time. Circuits that require precise transcriptional regulation in development, such as *Hox* genes (*1*, *2*) and segmentation clocks (*3*), colocalize multiple transcriptional units within tens of kilobases. By harnessing local chemical and physical forces, the organization of these neighboring genes may support their coordinated expression (*4*–*6*). Gene syntax specifies the relative order and orientation of adjacent genes. Pairs of genes can adopt a tandem, divergent, or convergent syntax, which are predicted to generate distinct profiles of gene coupling and dynamics (Fig. 1A) (*7*). These predicted profiles differ in both mean expression and levels of transcriptional noise. In native genomes, syntaxes are not equally represented across gene pairs (Fig. 1B and fig. S1). For example, in the human genome, closely spaced gene pairs more commonly adopt a divergent syntax. Potentially, gene syntax may couple expression of adjacent genes and tune transcriptional noise.

Gene syntax affects expression of colocalized genes through biophysical forces such as DNA supercoiling (*7*, *8*). DNA supercoiling, or the over- and undertwisting of double-stranded DNA, both influences and is generated by transcription in a directional manner. Mechanistically, transcribing RNA polymerases induce waves of supercoiling by melting the double-helical DNA polymer to read the underlying base pairs. According to the twin domain model, polymerases generate negative supercoiling upstream and positive supercoiling downstream (*9*, *10*). This supercoiling can take the form of twist, where supercoiling changes the average rotation per base pair, or writhe, where supercoiling forms large-scale intertwined loops. In turn, supercoiling impacts gene expression by influencing transcriptional bursting (*11*–*13*), polymerase stalling (*14*, *15*), topoisomerase activity (*16*–*21*), and chromatin folding (*22*–*25*). In particular, supercoiling may alter RNA polymerase binding; negative supercoiling reduces the binding energy and facilitates polymerase loading, whereas positive supercoiling increases the energy barrier and reduces binding rates (*26*).

As supercoiling diffuses along the DNA polymer, the directionality of transcription sets the energy landscape for subsequent polymerase binding events (Fig. 1A). Thus, models of supercoiling predict that transcription-induced changes in chromatin structure feed back into changes in transcriptional activity at adjacent genes (*27*–*30*), a phenomenon we define as supercoiling-mediated feedback (*7*). Because polymerase directionality governs supercoiling generation, gene syntax defines supercoiling-mediated feedback, setting syntax-specific profiles of gene expression (*7*). Patterns of supercoiling around actively transcribed genes have been observed and averaged genome wide in bacteria (*31*, *32*), eukaryotes (*11*, *22*, *24*, *31*, *33*), and human cells (*17*, *22*, *25*). However, the impact of transcription-induced supercoiling on fine-scale chromatin structure and syntax-specific patterns of expression remain uncharacterized in human cells.

DNA supercoiling is often studied through broad perturbations, including the loss or inhibition of topoisomerases and polymerases (*11*, *17*, *25*, *33*, *34*), which induce large changes in cellular physiology and limit observations to acute treatments and short timescales. Alternatively, synthetic two-gene systems offer a well-controlled test bed to independently vary gene syntax while keeping gene identity, circuit copy number, genomic location, and other parameters constant. Modulating the transcriptional activity of a single transgene within this genetically uniform background offers the precise control required to examine the predictions of supercoiling-mediated feedback using chromatin structure techniques.

Beyond advancing our understanding of native gene regulation, defining syntax-specific expression profiles may enhance design of synthetic gene circuits. Synthetic circuits offer programmable control of therapeutic cargoes, genome editors, and cell fate (*35*–*43*). However, predictable forward design of gene circuits remains challenging, requiring iterative "design-build-test" loops to achieve desired functions. Synthetic circuits on the length scale of ~10 kb are regularly integrated into the genome and thus are subject to biophysical forces, including DNA supercoiling, that may rapidly couple expression of their components (*7*, *8*). Harnessing syntax as an explicit design parameter may improve the predictability and performance of genome-integrated synthetic circuits (*7*).

In this work, we used synthetic two-gene circuits as a model system to examine how transcription of a single gene is coupled to the expression and chromatin structure of adjacent genes in human cells. Leveraging the control and orthogonality of inducible systems, we demonstrate that transcription-induced coupling generates syntax-specific profiles of expression across a range of human cell types and integration methods. To investigate the corresponding changes in chromatin, we used a suite of genomics techniques to characterize the structural and biochemical properties of the region surrounding the locus of circuit integration in human induced pluripotent stem cells (hiPSCs). Induction of transcription perturbs chromatin structure both at the circuit and hundreds of kilobases away, substantially altering the insulation, RNA polymerase II binding profile, and histone marks across the locus. Applying these principles of supercoiling-mediated feedback, we designed compact synthetic gene circuits for efficient delivery, tunable expression levels and noise, and robust induction across a variety of cells. These techniques allowed us to optimize production of a therapeutic antibody without substitution of genetic parts. Overall, we demonstrate how supercoiling-mediated feedback

[1]Department of Chemical Engineering, Massachusetts Institute of Technology, Cambridge, MA, USA. [2]Department of Biological Engineering, Massachusetts Institute of Technology, Cambridge, MA, USA. [3]School of Biomedical Engineering, University of British Columbia, Vancouver, BC, Canada. [4]Michael Smith Laboratories, University of British Columbia, Vancouver, BC, Canada. [5]Department of Bioengineering, California Institute of Technology, Pasadena, CA, USA. [6]Department of Anatomy and Embryology, Leiden University Medical Center, Leiden, Netherlands. [7]The Novo Nordisk Foundation Center for Stem Cell Medicine, reNEW, Leiden University Medical Center, Leiden, Netherlands. [8]The Ragon Institute of Mass General, MIT, and Harvard, Cambridge, MA, USA. ***Corresponding author. Email: katiegal@mit.edu**

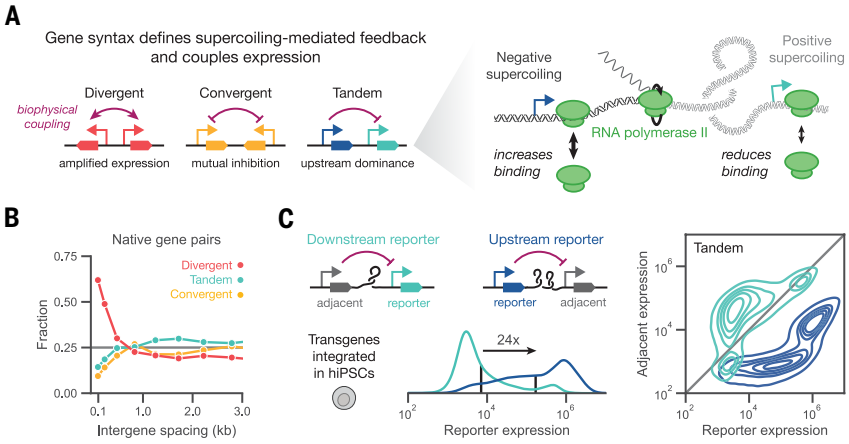

Fig. 1. Supercoiling-mediated feedback couples expression of adjacent genes. (**A**) Gene pairs can be arranged in divergent, convergent, or tandem syntax, which specifies the biophysical coupling (purple arrows) between genes through supercoiling-mediated feedback. DNA supercoiling modifies the energy required for polymerases to bind and locally melt DNA, leading to increased or decreased polymerase initiation. Transcribing polymerases generate negative supercoiling upstream and positive supercoiling downstream, which can diffuse to nearby genes. This supercoiling takes the form of twist, where supercoiling changes the average rotation per base pair, or writhe, where supercoiling forms large-scale twisted loops. These two forms freely interconvert. Together, transcription affects and is affected by supercoiling, forming a biophysical feedback loop that depends on the direction of transcription and thus on gene syntax. (**B**) Using Ensembl annotations for the human genome, gene extents were identified using the maximum extent of all annotated exons, then the gene syntax and intergene spacing were determined for each pair of adjacent genes. Gene pairs were split into equal-quantile bins based on intergene spacing, and the fraction of gene pairs with each syntax was computed for each bin. (**C**) Owing to accumulation of positive supercoiling at the downstream promoter, expression from an upstream gene is predicted to decrease expression of a downstream gene. Two-gene constructs expressing fluorescent proteins were integrated using PiggyBac in hiPSCs, where the adjacent gene is expressed from a weak PGK promoter and the reporter gene is expressed from a strong EF1α promoter. (Left) For a representative biological replicate, the distribution of reporter expression is shown as a function of position in the circuit. Geometric means are shown as black vertical lines, and the fold change between the two circuits is annotated. (Right) Distributions of reporter and adjacent gene expression for representative replicates of the same tandem circuits. The gray diagonal represents equal adjacent and reporter signal; the two circuits are approximately symmetric to each other across this line.

influences expression of adjacent genes, providing insights into native gene regulation and informing the design of synthetic systems.

Upstream dominance defines expression profiles of constitutive tandem transgenes

In native genes, upstream transcription can reduce expression of downstream genes (*44*–*46*). Models of supercoiling-mediated feedback predict that positive supercoiling generated by transcription at the upstream gene reduces the rate of transcription and thus expression at the downstream locus, resulting in upstream dominance (Fig. 1A) (*7*). To examine upstream dominance in a synthetic system, we constructed two-gene systems in tandem. Each gene was paired with a promoter and a polyadenylation signal (PAS) to form a transcriptional unit. The modularity of these synthetic systems allowed us to independently switch gene positions and regulatory elements.

To measure expression, we integrated these tandem two-gene systems into hiPSCs through PiggyBac transposase. We switched the positions of the tandem genes to isolate the effect of position on expression level. We quantified expression of the fluorescent reporter genes by flow cytometry, providing single-cell resolution needed to measure expression distributions. We found that gene position strongly influences the expression of the reporter. Even when pairing a strong promoter with a weak promoter, we saw clear upstream dominance with a large, 24-fold shift in expression based on position (Fig. 1C). Potentially, genetically encoded sequences, such as binding sites for the CCCTC binding factor (CTCF) (*47*, *48*) and the cHS4 insulator (*49*), that restrict chromatin-mediated interactions may reduce upstream dominance. To examine this hypothesis, we inserted tandem-oriented CTCF binding sites, native motifs previously identified to reduce enhancer-promoter interactions (*48*, *50*). These sequences have been used to flank integrated synthetic circuits to minimize impact of the integration site on circuit expression. Flanking the upstream gene, the downstream gene, or the entire two-gene construct with these sites did not eliminate upstream dominance (fig. S2A). Further, placing CTCF sites in several orientations between the two genes did not reduce upstream dominance relative to an inert spacer (fig. S2B). Instead, addition of these sites generally reduced expression of one or both genes.

The identity of regulatory elements, such as promoters and PASs, may influence coupling between genes (*51*, *52*). In testing a panel of common constitutive promoters, we consistently observed upstream dominance in PiggyBac-integrated human embryonic kidney (HEK) 293T cells (fig. S3, A and B), lentivirally integrated HEK293T cells (fig. S3C), and PiggyBac-integrated hiPSCs (fig. S4). In exchanging the PAS, we found that the choice of PAS has a minimal effect on the shape of expression distributions, mildly tuning the levels of gene expression (fig. S5). Thus, trends in syntax-specific expression are robust across a range of genetic parts for the tandem syntax.

Transcription of an adjacent gene induces syntax-specific coupling

Expression patterns of constitutively expressed tandem gene pairs suggest that syntax influences expression. However, these constitutive systems do not support dynamic control of transcription of a single adjacent gene, making it difficult to parse the transcription-driven mechanism of supercoiling-mediated feedback. To allow controlled induction of a single adjacent gene, we generated monoclonal HEK293T cell lines containing a doxycycline (dox)–inducible two-gene system in different syntaxes (Fig. 2). To build these lines, we placed a constitutive reporter gene under the control of a strong constitutive promoter (EF1α) and an adjacent inducible gene under the control of a dox-inducible promoter, TRE (Fig. 2A). Using PiggyBac, we delivered the dox-inducible two-gene systems encoded in tandem, convergent, and divergent syntaxes, which were predicted to show different transcription-induced couplings (*7*). The constitutively expressed dox-responsive activator, rtTA, was integrated from a separate PiggyBac donor. We sorted single cells to establish monoclonal lines of each syntax.

Upon dox addition, all syntaxes showed strong induction of the TRE-driven inducible gene (fig. S6, A and B). To quantify changes in expression of the constitutive reporter upon induction of the adjacent gene, we normalized reporter expression to the uninduced condition for each line. In the tandem syntax, induction of the upstream gene reduced expression of the downstream reporter gene (Fig. 2B and fig. S6, C and D). Conversely, induction of the divergent syntax strongly up-regulates expression from the constitutive reporter, matching predictions of amplification in divergent syntax (*7*). The convergent syntax shows a near-invariant profile of reporter expression. For the tandem and divergent syntaxes, induction of the adjacent gene results in a unimodal shift in the geometric mean (Fig. 2C). Unimodal shifts indicate

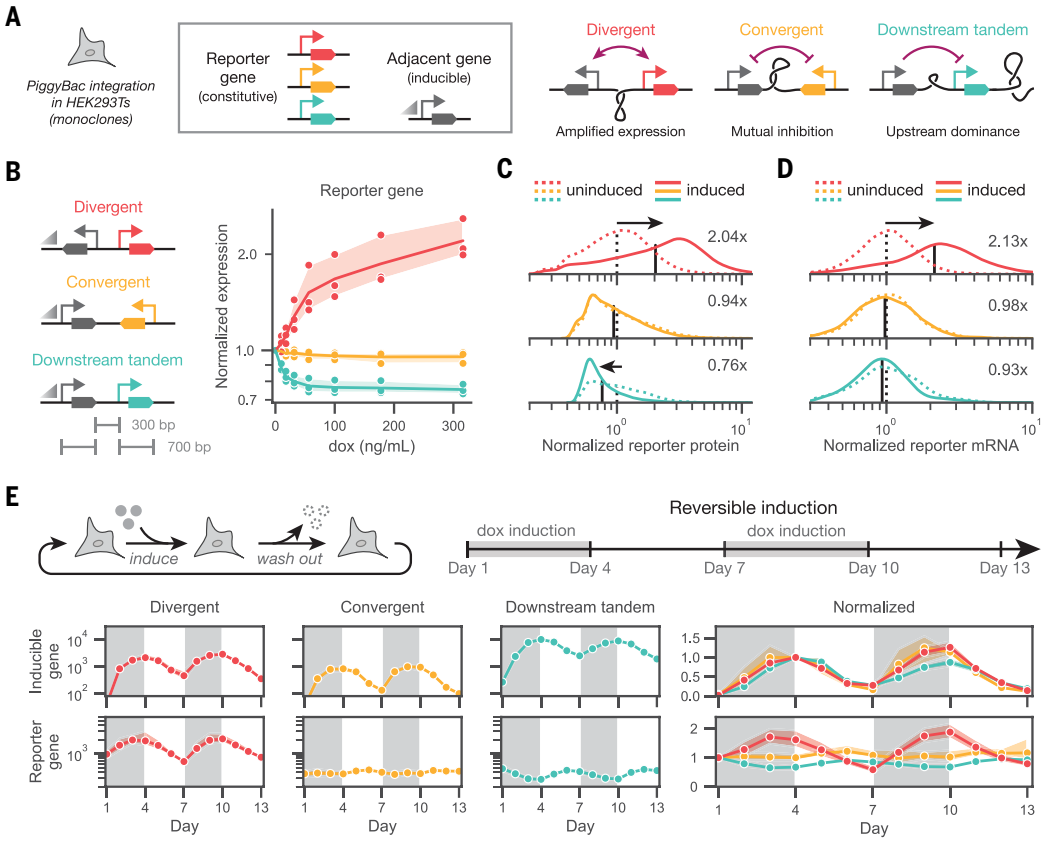

Fig. 2. Transcription induces syntax-specific coupling of expression of adjacent genes. (**A**) Two-gene systems consisting of a dox-inducible gene (~700 bp, TRE promoter) and a constitutively expressed gene (~700 bp, EF1α promoter) spaced ~300 bp apart were integrated into HEK293T cells using PiggyBac. The resulting cell lines were flow-sorted to single cells and expanded as monoclonal populations. (**B**) The geometric mean reporter expression, normalized to the uninduced condition, is shown as a function of dox concentration for the three different syntaxes. Geometric mean and associated 99% confidence interval are shown for three separately passaged and maintained replicates of the monoclonal cell lines. (**C** and **D**) Full reporter protein (C) and mRNA (D) distributions are shown in the uninduced case and the second-highest dox induction state. Geometric means are shown as black vertical lines, and the fold changes upon induction are annotated. (**E**) Dox was sequentially introduced and removed to measure the turn-on and -off dynamics of the integrated systems. The systems respond reversibly to the presence of dox. Geometric mean and associated 99% confidence interval are shown for four separately passaged and maintained replicates of the monoclonal cell lines.

a general mechanism of regulation, such as changes in the transcription rate, that is not restricted to a subpopulation of cells.

As a transcription-based process, supercoiling-mediated feedback should manifest in the distributions of mRNAs. To measure the mRNA distributions, we used single-cell hybridization chain reaction RNA fluorescence in situ hybridization (HCR RNA-FISH) (*52*, *53*) to quantify the transcriptional profiles of both the constitutive reporter gene and the dox-inducible gene (Fig. 2D and figs. S6, E and F, and S7). As expected, mRNA profiles generally match the syntax-specific profiles of proteins (Fig. 2C). For the convergent syntax, the inducible gene exhibits bimodal mRNA expression (figs. S6E and S7), matching modeling predictions of bimodality that may be obscured by stable protein reporters (*7*). Bimodality in mRNA expression for the constitutive reporter may not be visible due to the overall low expression of this gene in convergent syntax. Overall, the mRNA profiles align with the models of supercoiling-mediated feedback that predict that syntax influences transgene expression by altering rates of transcription.

DNA supercoiling-mediated coupling is predicted to be rapid and reversible. To test the reversibility of syntax-specific coupling, we sequentially induced and removed dox for 3-day periods over 13 days. We observed repeatable induction- and syntax-specific coupling of the inducible and reporter genes. Over 13 days, we observed minimal hysteresis, indicating that the trends in coupling are reversible and are not due to permanent changes in the chromatin state (Fig. 2E).

Transcription induces syntax-specific structures in the neighborhood of synthetic circuits

Transcription and transcription-induced supercoiling drive genome folding (*54*). Just as we used synthetic inducible circuits to probe how gene syntax affects gene expression (Fig. 2), these circuits provide a facile mechanism to regulate transcriptional activity and measure transcription-induced chromatin structures (Fig. 3A).

Measuring both one-dimensional (1D) and 3D chromatin profiles requires site-specific, homozygous integration of the synthetic circuit for downstream next-generation sequencing (NGS) assays. Site-specific integration allows circuits to be measured at a fixed location, and homozygous integration ensures reads can be accurately interpreted without allelic heterogeneity. Using the STRAIGHT-IN Dual allele platform (*55*), we integrated dox-inducible circuits placed in all four possible two-gene syntaxes into both alleles of a genomic safe harbor region located in intron 2 of the citrate lyase beta-like (*CLYBL*) gene (*56*) in hiPSCs, generating homozygous cell lines (fig. S8A). These circuits include the activator within the constitutively expressed gene. We confirmed that all four syntaxes showed reversible, syntax-specific profiles of expression, including divergent-mediated amplification and tandem-mediated upstream dominance, similar to those observed in the dox-inducible two-gene systems integrated into HEK293T cells (Fig. 3B and fig. S8B). Examining the single-cell mRNA distributions (fig. S8, C, D, and E), we found that most transcript levels matched the observed

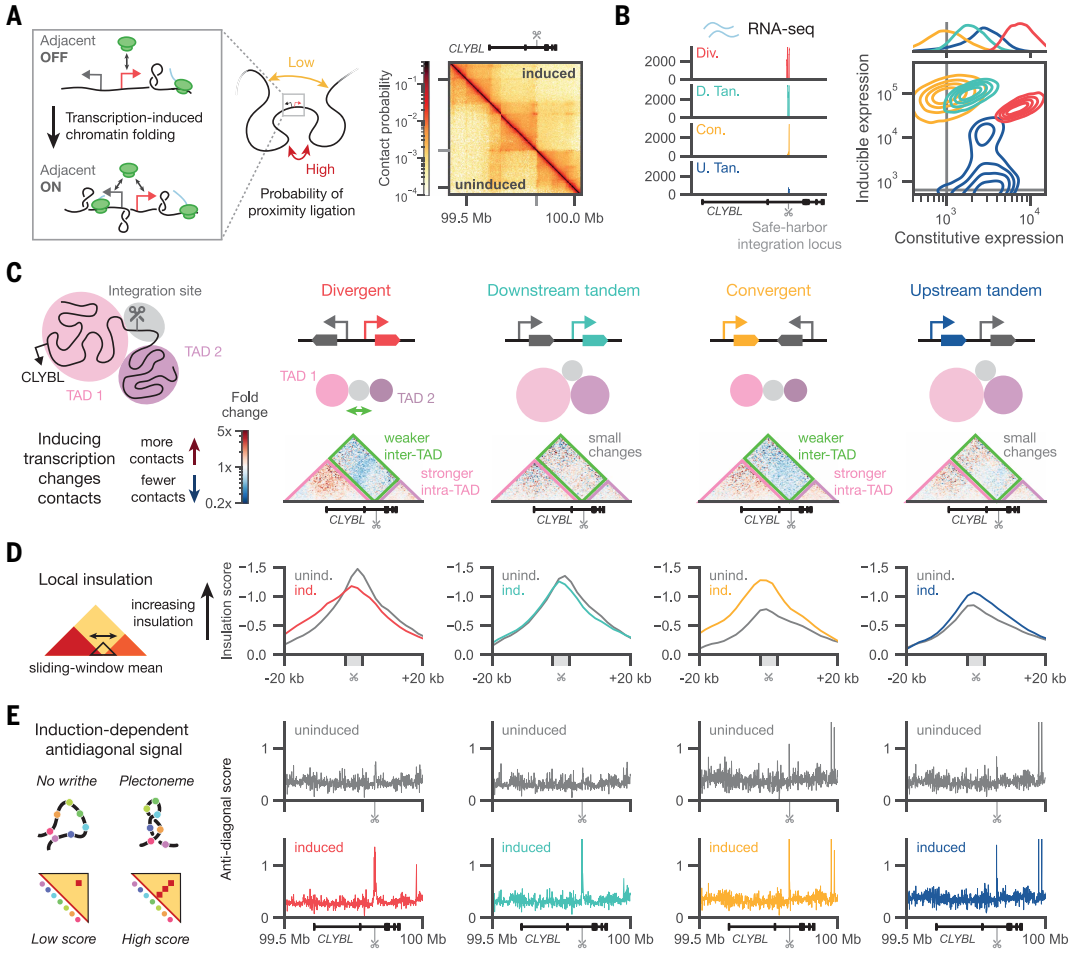

Fig. 3. Transcription induces syntax-specific chromatin structures across synthetic gene circuits and the surrounding locus. (**A**) Inducing transcription of an adjacent gene alters chromatin folding at the integration location and the surrounding region. 3D chromatin structure can be measured through RCMC, which uses proximity ligation and downstream sequencing to quantify contact probability. We performed RCMC on uninduced and induced conditions for all four syntaxes of two-gene circuits. The circuits were homozygously integrated into a landing pad at the *CLYBL* locus in hiPSCs (fig. S8A). A representative contact map for the divergent uninduced and induced conditions is shown. Gray ticks indicate the integration location. (**B**) (Left) Bulk RNA-seq tracks are shown for the induced condition of the cell lines in (A). (Right) Joint distributions of protein expression for the constitutive and inducible genes are shown for the same conditions. Histograms for constitutive expression are also shown (top). Gray lines indicate expression thresholds set by the nonintegrated, parental population. (**C**) RCMC data was binned at 5-kb resolution and iteratively balanced within the capture region. For each syntax, the fold change in contact probability upon induction was computed. We observed that in the divergent and convergent syntaxes, inter-TAD contacts decreased, whereas intra-TAD contacts increased. (**D**) Using a sliding-window insulation score (window size, 6 kb), the local insulation around the integration site was computed. Stronger insulation gives a more negative insulation score. The divergent and convergent syntaxes showed weaker and stronger local insulation, respectively. The tandem syntaxes only showed small changes in local insulation. Unind., uninduced; ind., induced. (**E**) The antidiagonal score, calculated as the sum of antidiagonal contact probabilities out to a distance of 5 kb, is shown across the entire capture region. A high antidiagonal score may indicate the presence of plectonemes, structures that form when DNA supercoiling twist converts to writhe. Strong antidiagonal scores are present at the integration locus upon induction for all four gene syntaxes. No chromatin outside of the integration region shows a comparable induction-dependent antidiagonal score.

protein level trends. However, the induced downstream tandem syntax showed high levels of RNA and low protein expression for the constitutive gene, potentially indicating a large fraction of unproductive transcripts (fig. S8E). To control for locus-specific effects, we integrated these constructs into another common safe harbor locus, *AAVS1*. *AAVS1* is also located within the intron of a transcriptionally active native gene (fig. S9, A and B). Like at the *CLYBL* locus, we observed syntax-specific profiles of expression at *AAVS1*, including both divergent-mediated amplification of the constitutive gene and poor expression from the downstream inducible gene in the upstream tandem syntax (fig. S9C). We attribute the approximately twofold drop in inducible gene expression at the *AAVS1* locus to interference from upstream native expression.

To understand how transcriptional activity and syntax affect the chromatin structure of our two gene circuits, we used Region Capture Micro-C (RCMC) (*57*) to measure the contact probability between genomic locations within a targeted region of interest (Fig. 3A). Notably, the *CLYBL* safe harbor integration site is located at the boundary of two topologically associating domains (TADs) (Fig. 3A). By computing the fold change in contact probability, we found that induction increases intra-TAD contacts and reduces inter-TAD contacts in the divergent and convergent syntaxes (Fig. 3C and fig. S10). Induction does not alter these contacts in the tandem syntaxes. Using a common sliding-window insulation score (*58*, *59*) that becomes more negative at strong TAD boundaries, the overall change in contact probability in the divergent and convergent syntaxes occurred alongside a substantial

weakening and strengthening, respectively, of the local TAD boundary (Fig. 3D). No substantial change in this boundary was observed in the tandem syntaxes. This change in the local insulation may be caused by perturbation of a loop domain present at the integration site. Visible as a "corner dot," the loop domain moves upon induction of the divergent and convergent syntaxes (fig. S11). In the divergent case, the loop domain splits to form a dual-loop domain. Putatively, this double loop may be an averaged interaction between two stochastic loop domains influenced by polymerases traveling upstream from the divergent promoter.

Beyond changes in TAD strength, we looked for other induction-dependent signals in the contact probability dataset. Specifically, both overwound and underwound supercoiled DNA can buckle, forming "figure eight" structures called plectonemes as DNA twist converts to writhe. Plectonemes facilitate the loading of chromatin loop extruders (*60*) and should appear as small-scale regions of high contact probability perpendicular to the diagonal, similar in shape to that of the large-scale "jets" generated by cohesion loop extrusion (*61*). Quantifying these structures using an antidiagonal score that sums contact probabilities along the antidiagonal over 5 kb, we observed strong, induction-dependent plectonemic signals at the integrated locus in all four syntaxes (Fig. 3E). Indeed, this signal correlates with the appearance of red antidiagonal stripes in the contact matrix (fig. S12 and movie S1). The magnitude of these induction-dependent, putatively plectonemic signals was not seen elsewhere in the capture region (fig. S13), strongly suggesting that transcription reshapes chromatin folding around our synthetic circuit.

Transcription drives syntax-specific profiles of supercoiling and changes in chromatin state

Supercoiling-mediated changes in gene expression coincide with changes in chromatin structure. In bacteria and in yeast, these 3D chromatin structures correlate with supercoiling density (*34*, *62*). Supercoiling-dependent structures should be accompanied by changes in both local supercoiling density and in epigenetic profiles demarcating active transcription. Our measurement of the antidiagonal score (Fig. 3E) is a suggestive but indirect measurement of supercoiling, as other structures, such as chromatin jets, also appear as antidiagonal contacts. Thus, we used GapRUN to measure positive supercoiling density (*17*, *34*), bulk RNA sequencing (RNA-seq) to measure productive transcripts, and CUT&Tag to measure the concentration of both actively elongating RNA polymerases and of various transcription-linked histone marks (Fig. 4).

Specifically, to complement our putative measurement of plectonemes (positive and negative writhe) through RCMC, we measured the amount of positive supercoiling twist. GapRUN uses the bacterial protein GapR to identify regions of positive supercoiling twist through an micrococcal nuclease (MNase)–based NGS readout (*17*, *34*). Because supercoiling freely interconverts between twist and writhe in the regime where plectonemes form, the presence of both antidiagonal RCMC contacts and GapR signal indicates overall positive supercoiling. We generally observed the formation of positive supercoils at the 3′ ends of active genes. In particular, positive supercoiling accumulates in the intergenic regions of tandem syntaxes (Fig. 4 and fig. S14), putatively the cause of upstream dominance. Measuring the polyadenylated transcripts through RNA-seq, we observed readthrough transcripts for the inducible gene, where the transcript extends past the polyadenylation signal and, for the downstream tandem and convergent syntaxes, into the intron of the constitutive gene (fig. S15). In the convergent syntax, these putative readthrough polymerases may be responsible for the small increase in GapR signal at the start of the constitutive gene, eliminating the predicted accumulation of positive supercoiling in the intergenic region. For the downstream tandem syntax, we observed unproductive constitutive transcripts, as measured by both RNA-seq (fig. S15) and RNA FISH (fig. S8E), that did not contribute to constitutive protein expression (Fig. 3B). This readthrough effect, although not observed in our randomly integrated constructs (Fig. 2), may explain some of the upstream dominance.

To quantify the transcriptional state of the locus, we measured the concentration of actively elongating RNA polymerase II (serine 2 phosphorylation) of two active histone marks H3K27ac and H3K4me3 (histone H3 lysine 27 acetylation and histone H3 lysine 4 trimethylation) and the heterochromatin mark H3K27me3 (histone H3 lysine 27 trimethylation). As a control, these transcription-linked signals were present at low levels in the distal, unedited *AAVS1* locus (fig. S16), but appeared at other highly transcribed loci (fig. S17). At our synthetically integrated locus, we detected elongating RNA polymerase II and active histone marks at actively transcribed genes (Fig. 4). Specifically, we observed that the actively transcribed genes have high H3K27ac signal in the promoter region; have H3K4me3 distributions that span sequences included in properly polyadenylated transcripts, as measured with RNA-seq; and show polymerases elongating both at the 5′ end and putatively after cleavage. Induction strongly increased signs of activity across the locus for the divergent and downstream tandem syntaxes. The upstream tandem and convergent syntaxes showed only minimal changes in these marks of active transcription upon induction (fig. S14), consistent with their poor expression of the circuit (Fig. 3B). Across syntaxes, we observed small changes in the heterochromatin mark H3K27me3, indicating that epigenetic silencing does not explain the low expression in the upstream tandem and convergent syntaxes.

Our direct and indirect supercoiling measurements complement each other (Figs. 3E and 4 and fig. S18). Although limited by the coarse 500-bp resolution of the antidiagonal score, the indirect RCMC-based measurement of positive and negative supercoiling overlaps with our GapR measurement of positive supercoiling in regions where this state is expected (fig. S18). In these regions, the observed positive supercoiling co-occurs with induction-dependent changes in the transcriptional state of the edited locus. The combination of these measurements suggests that the supercoiling mechanism drives syntax-specific profiles of expression.

Syntax-based tuning optimizes circuit expression and biologic production without part substitution

Synthetic circuits and other transgenic systems, such as biologic producer lines, are often optimized through selection of transcription factors, promoters, stoichiometric ratios, copy number, and integration locus (*63*–*65*). However, as each element may affect the dynamics of gene expression, forward design through simple exchange of parts remains iterative. Given that syntax modulates expression to a similar degree as genetic element selection (*52*), we proposed using syntax to tune the relative levels of expression without changing the sequences of these elements or their relative copy number. To test this syntax-based tuning scheme, we explored optimization of two common biotechnological tools: a monoclonal antibody producer line and an inducible lentivirus system.

Low-cost production of antibodies, especially for those against infectious and tropical diseases (*66*), can improve worldwide access to these antibody drugs. Increasing antibody titers offers a simple way to reduce the cost of production and enhance affordable access. To demonstrate the promise of syntax-based optimization, we integrated two-gene constructs encoding the heavy and light chains of an anti–yellow fever monoclonal antibody into a landing pad HEK293T cell line. Previous reports (*65*, *67*–*69*) suggest that excess light chain translation can increase titers. Thus, based on the principle of upstream dominance, we would expect that by setting a high ratio of light chain to heavy chain, the downstream tandem syntax would outperform the upstream tandem syntax. In measuring total human immunoglobulin G (IgG) titer through both a sandwich enzyme-linked immunosorbent assay (ELISA) (Fig. 5A) and a bead agglutination assay (fig. S19), we found a nearly fourfold difference in antibody titer as a function of syntax, with the downstream tandem and divergent syntaxes providing the highest titers, as expected.

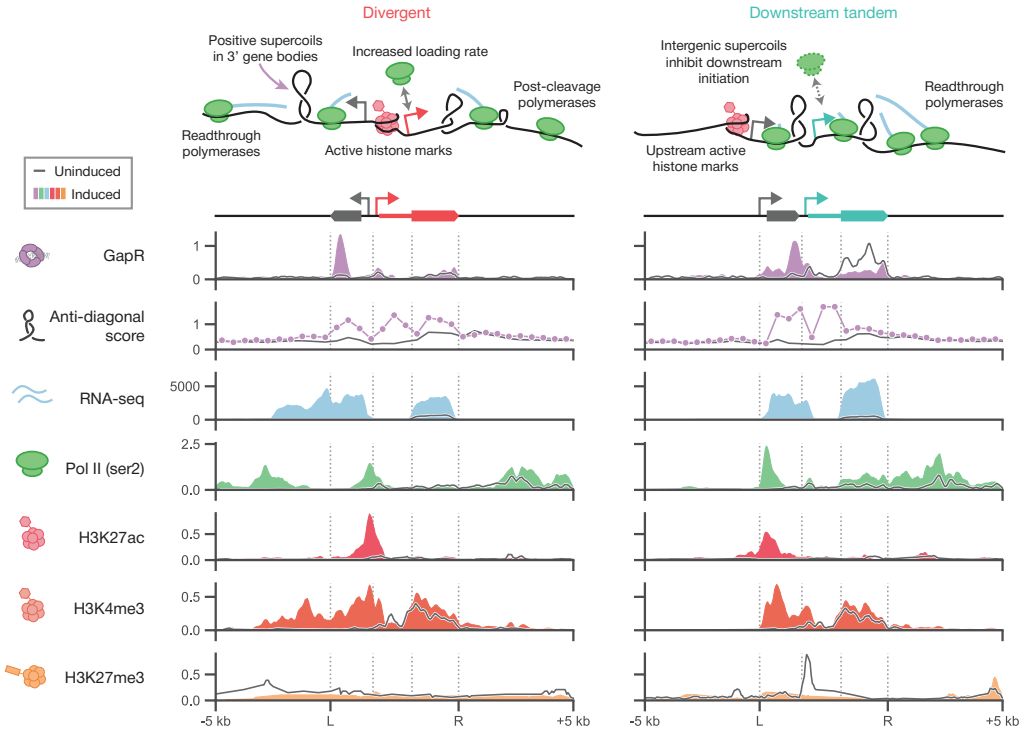

Fig. 4. Local chromatin state shows transcription-linked supercoiling generation. 1D genomics tracks are shown for the divergent and downstream tandem two-gene syntaxes, integrated homozygously into the *CLYBL* locus in hiPSCs as described in Fig. 3. Tracks are shown for the integration region and the surrounding 5 kb to the left and right. Vertical lines show the start and end of the synthetic circuit, the middle of the intergenic region, and the start of the constitutive gene exon. The GapR track was measured with GapRUN, a CUT&RUN-derived technique, and is shown as reads per million. The antidiagonal score track was computed as a 1D track from the 2D RCMC data and is a nondimensional quantity that is directly proportional to contact probability. The RNA-seq track was spike-in normalized and is shown as reads per million. The polymerase (Pol) II (ser2), H3K27ac, H3K4me3, and H3K27me3 tracks were measured with CUT&Tag, spike-in normalized, and shown as reads per million. All tracks are shown for the uninduced (gray line) and induced (colored fills and lines) conditions. Active histone marks, polymerase motion (including polymerases reading past the polyadenylation signal), and supercoiling combined to form a dynamic feedback loop that gave rise to the observed patterns of divergent amplification and tandem upstream dominance. Using the bacterial protein GapR, which binds to positive supercoiling (writhe), strong positive supercoiling was observed downstream of active transcription. Notably, positive supercoiling accumulated at either end of the divergent construct and in the intergenic region of the downstream tandem construct. These regions of positive supercoiling co-occurred with strong antidiagonal scores (RCMC) and in regions of active RNA polymerase II elongation (CUT&Tag). Further comparing the positive supercoiling signal with three histone marks quantified by CUT&Tag, we observed that positive supercoiling accumulated downstream of active transcription start sites and co-occurred with active transcriptional histone marks. Upon induction, the level of the repressive mark H3K27ac decreased across the integration region.

Lentiviruses offer efficient delivery of transgenes to diverse primary cells for therapeutic applications such as ex vivo engineering of CAR-T therapies and ex vivo immune cell reprogramming (*70*). Gene circuits and inducible systems offer safe, clinically guided control and the ability to target specific cell states (*35*). However, ensuring robust co-expression of multiple genes in these systems remains challenging. To explore syntax-based tuning of expression from an inducible lentivirus, we tested all four possible two-gene syntaxes transduced into HEK293T cells. Only the divergent and downstream tandem syntaxes displayed an appreciable double-positive population at maximum induction (Fig. 5B and fig. S20). Expression of the constitutive gene in the upstream tandem and convergent syntaxes strongly inhibited induction across all inducer concentrations (Fig. 5C and fig. S21). In the two syntaxes with strong induction, syntax sets the stoichiometric ratio between the two genes (Fig. 5D). Weak coupling between the two genes in the tandem syntax allows a wide range of stoichiometries upon induction, varying stoichiometry sevenfold (Fig. 5D). Conversely, the strong positive coupling between genes in the divergent syntax maintains a narrower ratio of expression. Tuning the ratio of expression between elements can substantially shift the behavior of gene circuits, potentially supporting or impeding desired functions (*71*, *72*). Together, our results demonstrate that syntax can tune expression levels in diverse synthetic circuits without requiring part substitution.

Syntax augments performance of compact gene circuits across cell types

Compact gene circuits support efficient delivery of therapeutic cargoes through size-restricted vectors, such as lentiviruses and adeno-associated viruses. However, the close proximity of multiple genes in these vectors introduces the potential for physical coupling between transcriptional units. To harness supercoiling-mediated feedback for improved circuit performance, we focused on optimizing a compact, lentivirally delivered "all-in-one" inducible circuit.

Unlike the inducible circuits in Figs. 2 and 5, all-in-one designs include the dox-responsive activator on the same construct, resulting in both biophysical and biochemical coupling (Fig. 6A). In the divergent syntax, positive supercoiling-mediated feedback should generate high, correlated expression. For both tandem syntaxes, negative feedback should reduce the degree of correlation between genes. Despite negative feedback, we expect that the downstream tandem syntax will support induction, provided that activator levels remain sufficient (*55*).

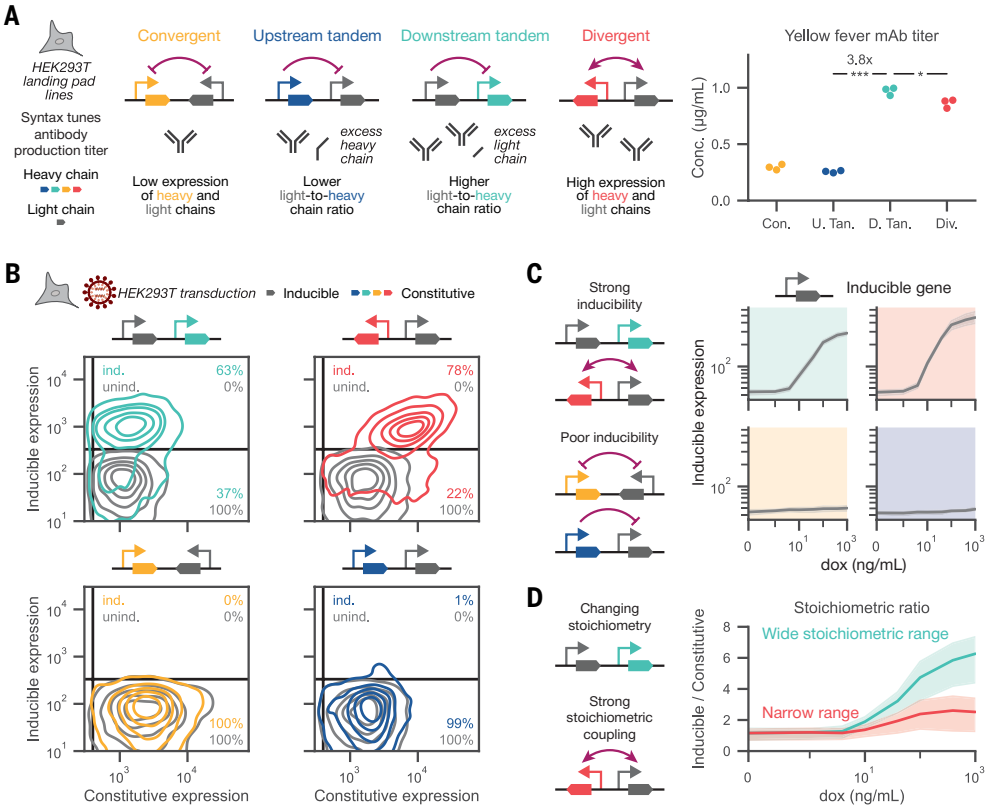

Fig. 5. Syntax-based tuning optimizes circuit expression and biologic production without part substitution. (**A**) The light and heavy chains of an anti–yellow fever monoclonal antibody (mAb) are expressed from two-gene constructs (dual CMV promoters) integrated at a landing pad at the Rogi2 locus in HEK293T cells. Antibody titer, as measured through sandwich ELISA, differs across syntaxes. Points depict three biological replicates. Statistics are from two-sided Student's *t* tests. $*P < 0.05$; $***P < 0.001$. (**B**) Two-gene circuits, consisting of a constitutive gene (EF1α promoter) and an inducible gene (TRE promoter), were lentivirally transduced into HEK293T cells with a second vector expressing the activator rtTA (EF1α-short promoter). Joint distributions in the absence (uninduced, gray) or presence (induced, colored) of 1 μg/mL dox are shown. Percentages refer to the proportion of cells expressing (top) or not expressing (bottom) the inducible gene, as indicated by manual thresholds (black lines). (**C**) The geometric mean of the inducible gene (gray) is shown as a function of dox concentration. Light gray shading represents the 95% confidence interval across four biological replicates. (**D**) The stoichiometric ratio between inducible and constitutive gene expression is shown as a function of dox concentration. Strong coupling of expression reduces the change in this ratio. Colored shading represents the 95% confidence interval across four biological replicates.

Transducing hiPSCs, we observed robust induction from the divergent and downstream tandem syntaxes (Fig. 6, B and C). These trends were mirrored for transduction in HEK293T cells and mouse embryonic fibroblasts (fig. S22). Expression of the synthetic activator in the downstream tandem syntax was more than an order of magnitude lower than in the divergent syntax. However, for all syntaxes, expression of the activator increased relative to the uninduced case (Fig. 6D). This increase may reflect a local increase in transcriptional resources that affects circuits with the activator in cis but not those in trans (i.e., with a separately integrated activator, as in Figs. 2 and 5) (*55*).

Supercoiling-mediated feedback is predicted to couple the probabilities of transcriptional bursting (*7*). Even for stable protein reporters, changes in correlated bursting may be visible in the variance of coexpression. Variance between two genes across a population of cells can be decomposed into two components: intrinsic noise, which quantifies the variability within individual single cells, and extrinsic noise, which reflects differences between cells, such as cell size (*73*, *74*). Conceptually, this decomposition of the variance is related to the "width" of the distribution along the main diagonal (extrinsic) and off-diagonal (intrinsic) when relating expression of the two genes. Dividing the intrinsic noise by the extrinsic noise gives a noise ratio that represents the relative contribution of intrinsic noise. Computing this metric, we observed that the divergent syntax consistently generates the lowest noise ratio (Fig. 6E); this generalizes across integration method, cell type, and circuit type (all-in-one and trans-located activator). With the exception of the trans-located activator circuit, these results generalize when the noise metric is computed both in logarithmic space (Fig. 6E), where noise is unaffected by shifts in mean expression, and in linear space (fig. S23), where noise is affected by shifts in mean expression. These observations align with our previous modeling predictions, where transcriptional coboursting in the divergent syntax dramatically reduced intrinsic noise relative to extrinsic noise (fig. S24A) (*7*). In all cases, we observed that syntax affects both the intrinsic and extrinsic noise (fig. S24, B to F). Lastly, placing the synthetic activator in trans to the main circuit increased the noise ratio relative to that of the all-in-one circuits (Fig. 6E). However, the trans circuits had lower extrinsic noise (fig. S24D), suggesting that placing the synthetic activator distal to the two-gene circuit dramatically increases the intrinsic noise.

Insulator sequences are used in synthetic circuits to reduce coupling between integrated transgenes (*75*–*77*), potentially mitigating the effects of supercoiling-mediated feedback. To test this hypothesis, we added cHS4 insulator sequences to the intergenic region in the all-in-one circuit. For all syntaxes, addition of the cHS4 core or full insulator sequence did not substantially change expression levels or noise profiles (Fig. 6F and fig. S25). Similarly, noninsulator spacer sequences ranging from 300 bp to 1.8 kb did not change the observed syntax-dependent trends (fig. S26).

In contrast to intergene spacer length, both gene length and average transcription rate are expected to influence the amount of generated supercoiling according to prior modeling. Longer genes generally generate more supercoiling for the same transcription rate (*7*). Integrating two-gene circuits into hiPSCs at the *CLYBL* locus with differing inducible gene lengths (fig. S27), we observed that protein expression of the inducible gene decreases monotonically with length. However, some of this reduction in expression may be due to inefficient 2A peptide skipping, poor expression of long intronless genes (*78*), or changes in mRNA stability. Thus, even though the expression of the constitutive gene remains largely the same as a function of inducible gene length, which could suggest that the enhanced supercoiling from longer genes compensates for the reduction in expression, future work is needed to control these other variables. Together, these data indicate that syntax offers a powerful design parameter for coupling and tuning profiles of expression that can be harnessed to dampen or amplify noise (*79*, *80*).

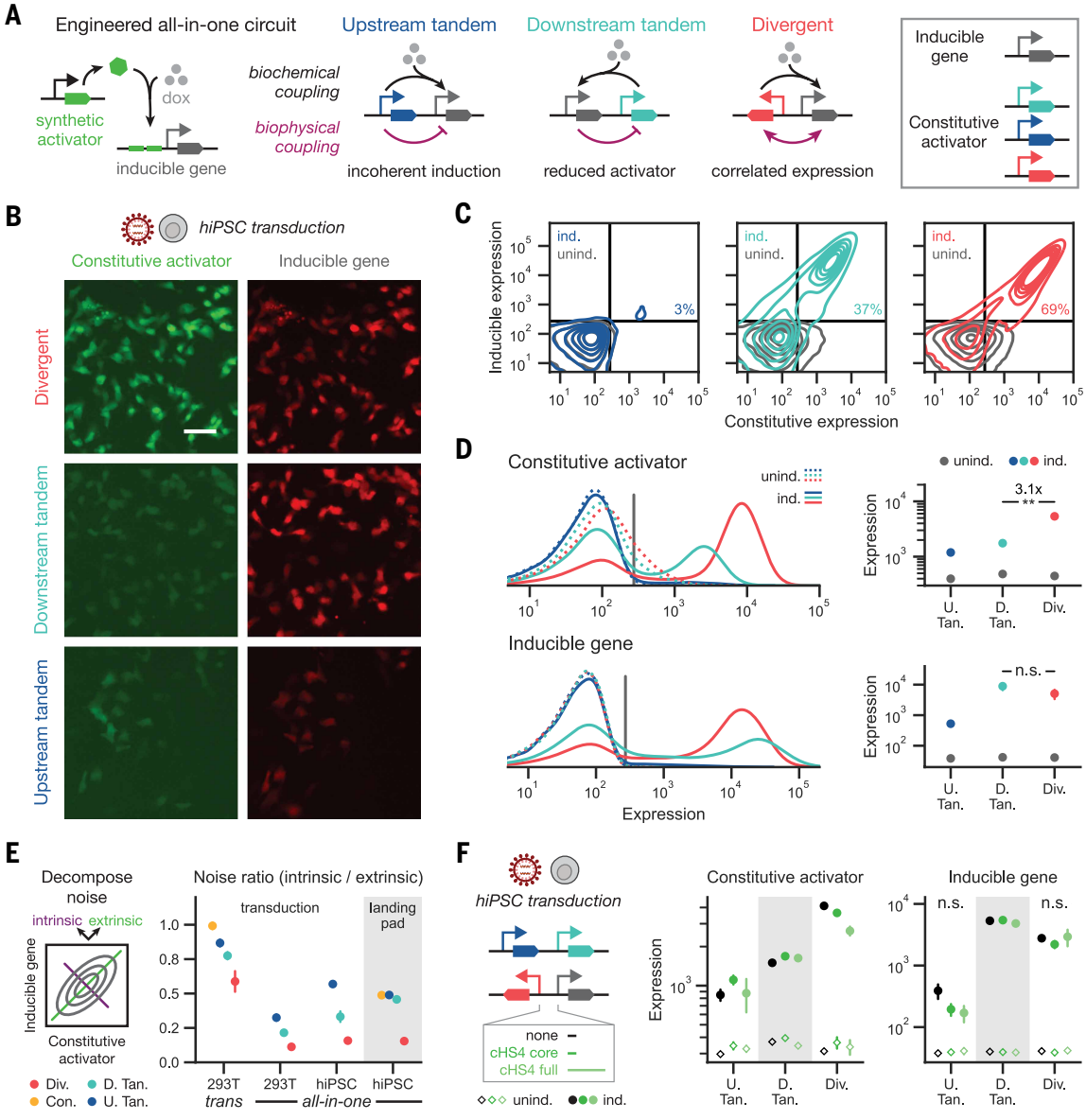

Fig. 6. Syntax augments performance of compact gene circuits across cell types. (**A**) A dox-inducible circuit relies on expression of a synthetic activator (rtTA) to activate the TRE promoter; an "all-in-one" circuit places both the activator (coexpressed with a fluorescent protein from the EF1α-short promoter) and the inducible gene of interest in the same cassette. The performance of the system is determined by the interplay between the biochemical coupling (black arrows) and the supercoiling-dependent biophysical coupling (purple arrows). (**B**) Representative microscopy images show the expression of the constitutive activator (left) and the inducible gene (right) for the circuit in (A) transduced into hiPSCs and induced with 300 ng/mL dox. Scale bar, 50 μm. (**C**) Joint distributions of activator and inducible gene expression are shown for each syntax when induced (colored) or uninduced (gray). Black lines depict expression thresholds set by the untransduced population. Percentages refer to the proportion of double-positive cells in the induced condition. (**D**) (Left) Expression distributions for the constitutive activator and inducible gene in the uninduced (dashed) and induced (solid) conditions. Vertical gray lines represent the expression thresholds from the untransduced population. (Right) Geometric mean expression of the constitutive activator and inducible gene are shown for uninduced (gray) and induced (colored) populations. Fold change is annotated for the divergent (Div.) syntax relative to the downstream tandem (D. Tan.) syntax when induced. U. Tan., upstream tandem. (**E**) Joint distributions can be decomposed into intrinsic (off-diagonal) and extrinsic (on-diagonal) noise. Noise is related to the variance in the log-transformed distributions of the two genes (see materials and methods). Ratios were computed for the trans-inducible or all-in-one circuits in HEK293T cells or hiPSCs integrated through transduction or a landing pad. (**F**) The cHS4 core (300 bp) or full (1300 bp) insulator sequence was placed in the intergenic region of the all-in-one circuit. The no insulator condition (none, 300 bp) is the same as the circuit in (D). Geometric mean expression levels of each gene are shown for hiPSCs lentivirally transduced with these circuits and induced with 300 ng/mL dox (circles) or uninduced (diamonds). Points represent the mean ± standard error for three biological replicates transduced with separate batches of lentivirus. Statistics are from two-sided Student's *t* tests. Not significant (n.s.), $P > 0.05$; *$P < 0.05$; **$P < 0.01$; ***$P < 0.001$; ****$P < 0.0001$.

Discussion

Transcription forms a dynamic feedback loop mediated by gene syntax and DNA supercoiling. In this work, syntax couples adjacent genes across diverse promoters, polyadenylation sequences, cell types, integration loci, and integration methods. Syntax-specific expression profiles persist with intergenic spacers up to 1.8 kb and even in the presence of putative insulator sequences such cHS4 and CTCF-binding motifs (*47*–*49*), suggesting that these features do not serve as barriers to supercoiling-induced coupling. As supercoils have been observed to spread over 2 kb (*81*) but are predicted to affect expression up to 10 kb

away (*7*), future work with longer spacers is needed to resolve the limits of supercoiling-mediated coupling.

Our findings with synthetic circuits align with previous observations. Upstream dominance affects transgenes (*82*, *83*), and synthetic circuits increasingly use divergent syntax for delivery to primary cells (*35*, *36*, *84*–*86*). In the native context, tandem arrays of *Hox* genes (*87*) and adjacent interactions of noncoding (*44*, *88*–*90*) and coding (*3*, *44*, *89*) genes tune cell fate in a syntax-specific manner. As native systems and therapeutic circuits require robust performance, choice of syntax may reflect the selection of functional circuits supported by supercoiling-mediated feedback.

Supercoiling-mediated feedback offers an extremely rapid mechanism of transcriptional coupling (*7*, *11*). Our work provides evidence that this phenomenon induces reversible, syntax-specific profiles of expression of adjacent genes, tuning both the mean and variance. Dynamic circuits that require coordinated expression of multiple genes, such as pulse generators, toggle switches, and oscillators, may benefit from the fast-timescale feedback of supercoiling. Supercoiling-mediated feedback may be especially useful to buffer noise in RNA-based control systems, supporting perfect adaptation and dosage control (*36*, *85*, *91*). As noise and small changes in expression can direct cell fate (*44*, *79*, *92*, *93*), syntax-based tuning offers a simple method to explore the stability of cell fate by perturbing native networks. Further, as an orthogonal design principle, syntax-based tuning can optimize circuit activity even when parts are constrained (*55*), complementing library-based approaches for circuit design (*64*, *94*, *95*).

Our findings are consistent with both biophysical predictions of DNA-supercoiling-mediated feedback (*7*) and in vitro studies (*26*, *96*–*98*), which used GapR to measure positive supercoiling (*17*, *34*) or small-molecule intercalators, such as psoralen, to measure negative supercoiling (*22*, *81*, *99*–*101*). Our work links strong antidiagonal scores measured with RCMC, an indirect measurement of negative or positive supercoiling, with the presence of positive supercoiling measured directly with GapR. The colocalization of these signals and the presence of active transcription in this region suggest the formation of plectonemes, though definitive observation of these structures in cells would be challenging. As we do not directly measure negative supercoiling, we can only infer that behaviors such as amplified divergent expression result from negatively supercoiled intergenic regions. Lastly, it is possible that changes in GapR signal upon induction coincide with changes in chromatin accessibility that alter GapR binding. However, the changes in GapR signal we observe are focal, suggesting differences in specific binding rather than broad differences in accessibility.

Although supercoiling-mediated feedback offers a compelling mechanism for the observed coupling of adjacent genes, there remain limits to and alternative explanations for this model. For example, collisions of RNA polymerases undergoing transcriptional readthrough may reduce expression in the convergent and tandem syntaxes (*102*). If a sufficient fraction of RNA polymerases read past the polyadenylation signal, as observed in our site-specific hiPSC lines, then supercoiling may be displaced beyond the end of the expected polymerase termination site. Additionally, we observed nonmonotonic changes in reporter expression with increasing adjacent gene length, a variable predicted to chiefly increase the amount of generated supercoiling. However, as circuit sequences can affect RNA processing (*52*), it remains challenging to develop an experimental system where gene length can be changed without modifying other parameters. The local transcriptional neighborhood also affects transcript isoforms and processing (*103*), potentially explaining the observed differences in expression for the downstream tandem syntax between hiPSCs and HEK293T cells. Beyond RNA processing, studies in other organisms suggest that perturbations to levels of topoisomerases, enzymes that curate DNA supercoiling, nonmonotonically affect transcription rates (*104*, *105*). As yet, the field lacks a definitive model for topoisomerase recruitment and its differential targeting of positive and negative supercoiling in human cells. We expect future work will uncover how cell type–and species-dependent features of gene regulation affect the degree of biophysical coupling.

Despite the clean, abstract way that synthetic circuits are often drawn, integration into the genome wraps synthetic circuitry in layers of native regulation. Biochemical interactions and biophysical forces combine to shape our genomes. By harnessing both layers of control, leveraging supercoiling-mediated feedback can enhance the predictability, performance, and functional range of engineered gene circuits.

Materials and methods

Bioinformatic analysis of intergene spacing across organisms

Genome annotations for *Saccharomyces cerevisiae*, *Mus musculus*, *Homo sapiens*, *Drosophila melanogaster*, *Caenorhabditis elegans*, and *Danio rerio* were downloaded from Ensembl, Release 110 (July 2023). Annotations with the type *gene*, *ncRNAgene*, or *pseudogene* were selected and gene pair information (intergene spacing and syntax) was calculated for all gene pairs and gene trios. Gene pairs were split into equal-quantile bins based on intergene spacing, and the fraction of gene pairs with each syntax (divergent, tandem, or convergent) was computed for each bin. The frequency of the tandem syntax was normalized by dividing by two to account for the two possible syntaxes (downstream tandem and upstream tandem) that are otherwise combined in this measurement. For fig. S1D, a null hypothesis distribution for gene trios was needed. Our null hypothesis is that any gene trio distribution (A/B/C) is solely described by the two adjacent gene pairs (A/B and B/C). To test this, we compared the syntax and intergene spacing distributions for all of the adjacent gene trios in the genome (A/B/C) to "synthetic" gene trios, where two gene pairs (A/B and C/D) with genes B and C aligned in the same direction are randomly selected and treated as a gene trio (A/BC/D).

Cloning of genetic constructs

All plasmids were constructed using a combination of scarless NEB HiFi assembly (NEB E2621X) and an in-house Golden Gate cloning scheme that allows for facile multi-level assembly of gene cassettes and multi-cassette plasmids. The fluorescent proteins used for each construct are listed in table S1. All construct designs and source plasmid identifiers for every figure panel are listed in table S2. Plasmid descriptions are found in tables S3 to S5. See data and materials availability for plasmid sequences.

Human iPSC transfection and PiggyBac integration

iPS11 cells (Alstem, episomal HFF-derived) were maintained in mTeSR1, mTeSR Plus, or eTeSR media (StemCell Technologies) supplemented with 0.5% penicillin/streptomycin (Gibco 15140122). Cells were grown in normoxia conditions (20% O_2, 37°C, 5% CO_2) on tissue culture-treated plastic plates coated for 30-60 min with Geltrex (Gibco) or Cultrex (Bio-Techne). For routine passaging, hiPSCs were dissociated to small clusters by (i) incubating in TrypLE Express (Gibco) for 2 to 4 min at 37°C, followed by quenching with mTeSR or eTeSR and light pipetting, or (ii) incubating in ReLeSR (STEMCELL Tech) according to manufacturer's instructions. On thaw or passage with TrypLE, cells were treated with 5 μM ROCK inhibitor (ROCKi) Y-27632 (STEMCELL Tech).

For transfections, hiPSCs were collected and seeded at 75×10^3 to 100×10^3 cells/mL in mTeSR1, mTeSR Plus, or eTeSR supplemented with 5 μM ROCKi Y-27632. The following day, cells were fed with fresh media and transfected with 80 ng (96-well plate), 480 ng (24-well plate), or 960 ng (12-well plate) DNA complexed at a 1:3 ratio of μg DNA: μL Lipofectamine Stem Reagent (ThermoFisher STEM00015). The DNA mixtures typically comprised 6:1:1:1 ratio (by mass) of plasmids respectively encoding the PiggyBac transposon, hyperactive PiggyBac transposase (*106*), Puromycin resistance gene (*pac*), and constitutive transfection marker (mKO2). On days 1 and 2 after transfection, cells were fed with fresh media supplemented with 0.5 μg/mL puromycin (Sigma P8833) to select for transfected cells transiently expressing *pac* from

a nonintegrating plasmid, thereby enriching for cells with PiggyBac integrations up to 90% purity. On subsequent days, cells were fed and passaged normally without puromycin, and subsampled during passages for flow cytometry.

Derivation of cell lines with matrix of constitutive promoters

Freshly passaged HEK293T cells (ATCC CRL-3216) maintained in DMEM + 10% FBS were seeded at 160,000 cells per well onto 0.1% gelatin-coated 24-well plates. The following day (0 dpt), cells were transfected with a 4:1 mass ratio of donor plasmid to PiggyBac supertranspoase, with a total transfected plasmid mass of 450 ng. Donor plasmids express two genes: mRuby2 and PuroR-T2A-mGreenLantern (plasmids 35-44 in table S4). At 1 day post transfection (dpt), cells were media changed into fresh media containing 1 μg/mL puromycin. Selection was maintained for two days (until 3 dpt), and surviving cells were passaged onto 6-well plates. After around a week of outgrowth (until each cell line was ~30% confluent), 1 μg/mL puromycin was maintained for around two days, until no visible surviving cells in an untransfected control well were observed.

One day prior to sorting, single color control plasmids were transfected into fresh HEK293T cells for use in compensation. A Sony MA900 cell sorter was used to polyclonally sort cells. The majority of cell lines were double-positive sorted, using gates that exclude an untransfected control. Cell lines containing PGK, a very low-expressing promoter, were sorted in a single-positive manner, where a cell was included if it was positive for mRuby2 or mGreenLantern. Cells were sorted into conditioned media, containing 50% conditioned media from a confluent plate of HEK293T cells (0.2-micron–filtered) and 50% fresh DMEM + 10% FBS, supplemented with 0.5% penicillin/streptomycin (Gibco 15140122). The resulting cells were outgrown and tested negative for mycoplasma.

Lentivirus production

To produce all lentiviral vectors, HEK293T Lenti-X cells (Takara 632180) were seeded at 7.0 to 7.5 million cells per 10cm dish coated with 0.1% gelatin. The following day (0 dpt), each plate was transfected with 6 μg transfer plasmid, 6 μg packaging plasmid (psPAX2, Addgene #12260), and 12 μg envelope plasmid (VSVG, Addgene #12259). Six hours later, each 10cm dish was media changed into 6.5 mL of HEPES-buffered (25 mM HEPES at pH 7.0) DMEM + 10% FBS. The following day (1 dpt), this media was collected, and fresh buffered media was added. The following day (2 dpt), these two aliquots were combined, filtered through a 0.45-μm PES filter, combined with Lenti-X Concentrator (Takara 631232) overnight, and concentrated the following morning (3 dpt) according to manufacturer instructions.

Transduction of tandem syntax lentivirus

Freshly passaged HEK293T cells were seeded at 15,000 cells per well onto 0.1% gelatin-coated 96-well plates. The following day, cells were media changed into media containing 5 μg/mL polybrene (hexadimethrine bromide, Sigma-Aldrich, H9268-5G) and a serial dilution of concentrated lentivirus over 3.5 orders of magnitude (highest concentration: 5.0 μL concentrated virus per well). After two days, cells were dissociated and flowed. From the titration, representative concentrations were chosen with an MOI of approximately 0.5 for plotting in fig. S3C.

Generation of monoclonal HEK293T cell lines

Freshly passaged HEK293T cells were seeded at 20,000 cells per well onto 0.1% gelatin-coated 96-well plates. The following day, cells were transfected with a total of 340 ng of DNA, with a 1:1:1 mass ratio of PiggyBac supertransposase, rtTA and PuroR donor (CMV-rtTA-βglobin_pA-CMV-PuroR-bGH, plasmid 3 in table S3), and two-gene donor. On 1 dpt, 2 dpt, and 3 dpt, cells were media changed into fresh media containing 1 μg/mL puromycin. On 4 dpt, cells were passaged to 24-well scale and left to outgrow in media without puromycin. On 14 dpt, cells were passaged onto a 6-well plate. On 17 dpt, cells were passaged at high dilution to a new 6-well plate and maintained for the next ten days in media containing doxycycline (Sigma-Aldrich D3447).

One day prior to sorting, single color control plasmids were transfected for compensation. A Sony MA900 cell sorter was used to monoclonally sort double-positive cells, using gates that exclude an untransfected control. Specifically, individual cells were sorted into wells of a fresh 96-well plate with conditioned media supplemented with 0.5% penicillin/streptomycin (Gibco 15140122) as described in the previous sections. Cells were allowed to outgrow over a period of two weeks. The resulting monoclonal cell lines tested negative for mycoplasma.

Characterization of fluorescent protein expression in monoclonal lines

Thirty-thousand cells per well of each monoclonal cell line were seeded onto 0.1% gelatin-coated 96-well plates. The next day, media was changed into DMEM + 10% FBS containing 0 to 316 ng/mL dox. Two days later, cells were prepared for flow cytometry.

Dox titration series and time course induction

The monoclonal cell lines as described above were seeded at low confluency, 20,000 cells per well, onto 0.1% gelatin-coated 24-well plates, in DMEM + 10% FBS containing 316 ng/mL dox. Independent wells were seeded for every experimental day. On each subsequent day from day 1 to day 13, cells were dissociated with trypsin and flowed as described in the Flow Cytometry section below. Cells were media changed into media without dox at day 4. At day 7, the remaining relatively confluent cells were passaged onto fresh 24-well plates, at 12,500 cells per well, in media containing dox. At day 10, cells were media changed into media without dox.

Characterization of mRNA profile in monoclonal lines

One-hundred and fifty thousand cells per well of each monoclonal line were seeded onto 0.1% gelatin-coated 12-well plates. The next day, fresh media was exchanged, with half the wells supplemented with 316 ng/mL dox. Two days later, cells were resuspended in PBS for HCR RNA-FISH.

We used the optimized HCR RNA-FISH protocol described in Peterman *et al.* (*52*) with Molecular Instruments probe sets for TagBFP (compatible with B1 amplifiers conjugated to Alexa Fluor 647) and mRuby2 (compatible with B2 amplifiers conjugated to Alexa Fluor 514). Briefly, after suspension in PBS, cells were transferred to 96-well v-bottom plate for HCR Flow-FISH. After each resuspension, spins were performed at 500 rcf for 5 min with default settings, unless otherwise noted. Cells were first fixed by incubation in 4% PFA for 15 min at room temperature. After spinning, cells were then permeabilized using 0.5% Tween-20 for 15 min at room temperature. Next, cells were spun and resuspended in hybridization buffer for 30 min at 37°C. During this incubation, probe set stock solution was diluted in hybridization buffer to a concentration of 14 nM for transfected cells or 28 nM for integrated cell lines. Cells were spun and resuspended in this probe solution for incubation overnight at 37°C. Due to the viscosity of the hybridization buffer, these spins were performed with reduced deceleration speed to minimize cell loss.

Following hybridization, cells were spun and resuspended in wash buffer for 15 min at 37°C. Then, cells were spun and resuspended in 5X SSCT for 5 min at room temperature. After these washes, cells were spun and resuspended in amplification buffer for 30 min at room temperature. Amplifier solution was prepared by combining separately snap-cooled hairpins h1 and h2 (Molecular Instruments) at a concentration of 130 nM in amplification buffer. Cells were spun and then incubated with this amplifier solution overnight at room temperature.

Following amplification, cells were spun and resuspended in 5X SSCT for one 30-min incubation and one 5-min incubation at room temperature. Lastly, cells were spun and resuspended in PBS for flow cytometry.

Generation of hiPSC lines with circuits integrated at *CLYBL* or *AAVS1*

The STRAIGHT-IN Dual platform was used to integrate the all-in-one inducible circuits at both alleles of *CLYBL* in the landing pad line derived from LUMC0099iCTRL04 (*55*). A single copy of the all-in-one inducible circuit with each syntax was separately integrated into a "GT" STRIAGHT-IN landing pad located within intron 2 of one allele of *CLYBL*. Following the STRAIGHT-IN Dual protocol, 600 ng of the donor plasmid ("GT" plasmids 7-14 in table S3) were transfected along with 400 ng of Bxb1-expressing plasmid (Addgene #51271) into 100,000 cells of the parental landing pad hiPSCs using Lipofectamine Stem Reagent (ThermoFisher STEM00015). The selection and excision of the lines was performed using the STRAIGHT-IN Dual protocol (*55*). These heterozygous cell lines were used for the timecourse induction experiment in Fig. S8B.

Next, a second copy of the all-in-one inducible circuit was integrated into a "GA" STRAIGHT-IN landing pad at the other allele of *CLYBL*. For this, donor plasmids ("GA" plasmids 7 to 14 in table S3) were used, following the same protocol. These homozygously integrated lines were then used for the HCR RNA Flow-FISH, RNA-seq, RCMC, GapRUN, and CUT&Tag assays.

The same donor plasmids and protocol were used to integrate the circuits at a single allele of *AAVS1*, beginning with a parental hiPSC line containing the STRAIGHT-IN landing pad at this locus. Lastly, the circuits with varying gene lengths (donor plasmids 60 to 71 in table S4) in were integrated at a single allele of *CLYBL* following the same protocol.

These lines were maintained in StemFlex Medium (Thermo Scientific A3349401) with 0.5% Penicillin-Streptomycin (Gibco 15140122) on plates coated with 5 μg/mL Laminin-521 (STEMCELL Technologies 200-0117). Cells were passaged using Gentle Cell Dissociation Reagent (STEMCELL Technologies 100-1077) and cultured with media containing a 1:200 dilution of RevitaCell Supplement (Thermo Scientific A2644501) for 24 hours after plating. Media was replaced with fresh StemFlex + Pen/Strep every 2 to 3 days, and cells were grown at 37°C with 5% CO_2.

Characterization of mRNA profile in homozygous hiPSC lines

The four hiPSC lines with two-gene circuits homozygously integrated at *CLYBL* were cultured with or without 1 μg/mL dox for three days. Then, the cells were non-enzymatically dissociated using Gentle Cell Dissociation Reagent (STEMCELL Technologies 100-1077) and resuspended in PBS for HCR RNA-FISH. Molecular Instruments probe sets for mTagBFP2 (compatible with B1 amplifiers conjugated to Alexa Fluor 647) and mScarlet (compatible with B2 amplifiers conjugated to Alexa Fluor 514) were used, and the same protocol as for the monoclonal HEK293T lines was followed. The STRAIGHT-IN landing pad line without a circuit integrated was used as the parental condition to control for background RNA-FISH signal.

RNA-seq

The four hiPSC lines with two-gene circuits homozygously integrated at *CLYBL* were cultured with or without 1 μg/mL dox for three days. Then, the cells were non-enzymatically dissociated using Gentle Cell Dissociation Reagent (STEMCELL Technologies 100-1077), washed in PBS, and counted. 300,000 cells were collected per condition, and RNA was extracted using the Monarch Total RNA purification kit (NEB T2010) according to manufacturer's instructions. For each sample, 2 μL of a 1:100 dilution of ERCC spike-in RNA (Mix 1, Thermo Fisher 4456740) was added during the lysis step. RNA samples were sent to the MIT BioMicro Center for processing, using the NEB Ultra II Directional RNA with Poly(A) selection kit followed by library prep with unique dual indexes.

The pooled libraries were sequenced using 2x75bp paired reads on a single lane of an AVITI Cloudbreak Freestyle High chip (500M reads). Paired-end reads were trimmed using *trim-galore* (version 0.6.10). Trimmed paired-end reads were aligned to these genomes using *bowtie2* (version 2.5.4) using the *--very-sensitive-local* preset. Reads were deduplicated using *gatk*'s *MarkDuplicatesSpark* (version 4.6.2.0) and were cell-number normalized based on the number of ERCC-mapped reads. Normalized bigwig files were generated using *deeptools* (version 3.5.6).

Region Capture Micro-C

Three capture regions of interest, each roughly 0.5 Mb, around three common landing pad integration sites were selected: *CLYBL* (chr13, 99,422,000-100,031,000), *AAVS1* (chr19, 54,810,00055,715,000), and Rogi2 (chr3, 22,542,000-22,964,000) (*107*). A custom panel of 80-mer probes targeting these regions and all synthetic parts inserted into these loci was designed and ordered from Twist Bioscience. Probes were selected based on a medium-stringency filter to reduce off-target pull-down, with some key areas near native TAD boundaries included using a low-stringency filter.

The homozygous hiPSC lines were expanded and outgrown in 6-well plates, with one plate for each of the sixteen conditions (four syntaxes, two induction conditions, and two biological replicates). Cells were dissociated with Gentle Cell Dissociation Reagent (STEMCELL Technologies 100-1077) according to the manufacturer's instructions and counted. From each of the conditions, 15M cells were collected and treated as described in Goel *et al.* (*57*). An additional 25M cells were collected for the MNase titration. Briefly, cells were washed in PBS and crosslinked using DSG (ThermoFisher 20593) and formaldehyde. After quenching, cells were washed, resuspended in PBS and counted, then resuspended in Micro-C buffer #1. Cell counts after resuspension per condition varied between 6M and 13M cells.

A key variable in Micro-C is the ratio of MNase to cells. To identify ideal digestion concentrations, a titration of MNase (Worthington Biochem LS004798) was performed on the separated aliquot of cells. Increasing amounts of MNase were added and samples were purified and gel-separated. The optimal amount of MNase digests chromatin to primarily mononucleosomal fragments, with few but visible dinucleosomal and trinucleosomal bands, here around 6U per million cells. Using the optimal ratio, samples were digested with MNase, end-repaired, blunted, and labeled with biotinylated nucleotides. The biotin-labeled chromatin was then proximity ligated overnight. After enzymatic cleanup steps, the chromatin was then reverse crosslinked overnight. Dinucleosomes were selected using a gel extraction, and T1 Streptavidin beads (Invitrogen 65601) were used to purify labeled fragments.

In order to determine the minimum number of cycles required to reach the desired library concentration while minimizing polymerase chain reaction (PCR) duplicates, a test amplification was performed with a small aliquot of each sample for a range of cycle numbers. The resulting PCRs were run on an agarose gel and quantified by imaging and by Qubit. Using this quantification, each sample was amplified to reach a target mass of 200 ng. NEB Multiplex Oligos for Illumina Primer Set 1 (NEB E7335) and NEBNext® HighFidelity 2X PCR Master Mix (NEB M0541) were used for all PCRs, and sample barcodes were selected following NEB recommendations. The resulting libraries were purified using AmPure XP beads (Beckman Coulter A63880), quantified via Bioanalyzer, and quantified via qPCR using the NEBNext Library Quant kit for Illumina (NEB E7630).

The resulting libraries were mixed in equal-mass proportions and region-captured following Twist Bioscience's Standard Hybridization Target Enrichment Protocol, with the modification that a test PCR was performed using the same reagents as above to identify an appropriate number of amplification cycles. The resulting region-capture libraries were purified and quantified via Bioanalyzer and qPCR. The pooled library was sequenced either via paired-end 2x75 cycle sequencing using Element's AVITI Cloudbreak Freestyle High flowcell (direct Illumina anchor sequencing without index conversion) for the divergent and downstream tandem conditions or the 2x150 cycle sequencing using a single lane of a NovaSeq X 10B flowcell for the convergent and upstream tandem conditions. Both methods gave about 500M reads per condition.

RCMC bioinformatics

For each integrated syntax, custom human genome references were generated by editing the GRCh38 genome to contain the inserted synthetic construct at the *CLYBL* landing pad. Paired-end reads were trimmed using *trim-galore* (version 0.6.10). Trimmed paired-end reads were aligned to these genomes using *bowtie2* (version 2.5.4) using the *--very-sensitive-local* preset. Then, *pairtools* (version 1.1.3) was used to identify Hi-C pairs (with *--walks-policy mask* and *--min-mapq 2*) and deduplicate them (with *--max-mismatch 1*). The resulting reads were converted to the .mcool format using *cooler* (version 0.10.4). The resulting matrices were ICE balanced (within each capture region for the majority of this work, and globally for fig. S28B) and binned at both 500- and 2000-bp resolutions.

To evaluate the reproducibility of this method, the stratum-corrected correlation coefficient as implemented in Yang *et al.* (*108*) was used to evaluate the similarity of all samples, both within the capture region of interest (fig. S28A) and in distal regions (fig. S28C). Based on the high reproducibility observed, reads from the two biological replicates for each syntax and induction condition were merged for the rest of this work. Two distal, unmodified capture regions did not show induction-dependent changes (fig. S28C).

Using the balanced contact matrices, fold changes in contact probability upon induction are calculated by dividing these matrices by each other. The sliding-window insulation score in Fig. 3D is calculated using the insulation function in *cooler* and uses a sliding window of 50 kb. The anti-diagonal score presented in Fig. 3E sums the contact probability along the anti-diagonal (i.e., perpendicular to the main diagonal) up to a given distance, centered at a given genomic coordinate. Specifically, we use the balanced contact matrices, binned at 500-bp resolution, and sum bins within 5 kb of the target location. For a given bin at location x, this means summing the probability of the $(x - 500\text{bp})$ bin contacting the $(x + 500\text{bp})$ bin to the probability of the $(x - 1000\text{bp})$ bin contacting the $(x + 1000\text{bp})$ bin.

Producing nanobody-MNase fusion protein

The following protocol is modified and scaled down from the protein production protocol in Koidl *et al.* (*109*) and the GapRUN protocol in Longo *et al.* (*17*). GapRUN relies on an MNase-nanobody fusion protein that is not commercially available. However, the protein can be reliably produced at a scale sufficient for roughly 24 reactions without needing a FPLC or sonicator. At a high level, protein production proceeds by inducing bacterial cells overnight at 18°C, lysing the cells, clarifying the lysate, and binding the fusion protein to glutathione spin columns. After successive washes, the fusion protein is cleaved off the column using biotin-tagged thrombin protease. The protease is removed from the eluate using streptavidin beads, and the resulting fusion protein is concentrated and buffer is exchanged using spin columns.

The following buffers were prepared. First, sample buffer is 10% glycerol, 2% SDS, 50 mM Tris, 20 mM EDTA, and 1% β-mercaptoethanol (for 10 mL, this is 2 mL of 50% glycerol, 500 µL of 1 M Tris pH 6.8, 2 mL 10% SDS, 400 µL 0.5 M EDTA, and 100 µL of β-mercaptoethanol, with Milli-Q grade water added to 10 mL). The β-mercaptoethanol should be added shortly before use. Bromophenol blue dye can optionally be added to give the buffer color, which is useful when loading protein gels. Second, the protein purification wash buffer is 125 mM Tris, 150 mM NaCl at pH 8.0.

An isopropyl-β-D-thiogalactopyranoside (IPTG)–inducible protein production plasmid encoding GST-LaG16-MNase (Addgene 170978) was transformed into BL21 (DE3) competent cells. The resulting bacteria were streaked to single colonies, and a single colony was used to start a 10 mL overnight culture at 37°C in LB-Amp media. The following day, 800 mL of LB-Amp (split into 200 mL volumes distributed across 4 baffled 1-liter flasks) was inoculated with 8 mL of the overnight culture (1:100 dilution). The cells were grown to an OD600 of 0.5, which takes about two hours. Once the flasks reached an OD of 0.5 mL, a 1.5 mL "pre-induction" sample was taken, spun down, and resuspended in 300 µL of sample buffer, then stored at -20°C for later analysis. Each flask containing 200 mL of media was induced with 200 µL of 1M IPTG (sterile-filtered with 0.2-micron filters) and the flasks were placed back in the shake incubator at a temperature of 18°C overnight. The lower temperature is required to maintain solubility of the produced protein. The following morning, the OD600 was measured on a 5-fold diluted sample, and found to be around 6.0. A "post-induction" 500 µL sample was also taken, spun down, and resuspended in 300 µL of sample buffer, and stored at -20°C for later analysis.

Cells were pelleted at maximum speed in a fixed-angle rotor. After combining pellets together, the cells were resuspended in complete B-Per buffer (Thermo Fisher 78248) plus EDTA-free protease inhibitor (Thermo Fisher A32965). Specifically, every gram of cell pellet was resuspended in 4 mL of B-Per plus 2 µL of lysosome and DNAse I (both included in the B-Per kit) plus 40 µL of 100x protease inhibitor cocktail (1 protease tablet in 500 µL of Milli-Q grade water). After incubation at room temperature for 15 min, the slurry was subjected to two freeze thaw cycles at -80°C to further lyse the cells. The resulting lysate was spun at 14k x g in a fixed-angle rotor for 30 min at 4°C. A 50 µL sample of the clarified lysate was diluted to 300 µL in sample buffer and stored at -20°C for later analysis.

The resulting clarified lysate was diluted 2:1 with protein purification wash buffer (for every 2 mL of lysate, add 1 mL of wash buffer). Two 0.2-mL glutathione spin columns (Thermo Fisher 16106) were washed with wash buffer as directed by the manufacturer instructions, then the diluted clarified lysate was loaded onto the columns with sequential spins. After loading, the columns were washed successively with two column-volumes (400 µL) of wash buffer until the A280 absorbance (measured with a NanoDrop) dropped to background levels, about 20 column-volumes needed in total. To cleave the fusion protein from the column, 100 units of biotin-tagged thrombin protease (Sigma-Aldrich SAE0147-5KU) diluted to 200 µL in wash buffer was added to each capped spin column and incubated overnight at 4°C.

The following day, the columns were spun, collecting "elution 1." One column-volume (200 µL) of wash buffer was added and the columns were again spun, producing "elution 2," and so on for a third elution. 10 µL samples of the elutions were combined with 10 µL of sample buffer for later analysis. The A280 absorbance of these elutions were checked, and the first two elutions were combined. To remove the thrombin protease, the combined elution (400 µL) was mixed in low-binding 1.7-mL tubes with 60 µL of T1 streptavidin beads (Thermo Fisher 65601) that had been washed three times with PBS (each wash consisting of magnetically separating the beads, removing the supernatant, and resuspending in 200 µL of PBS). The resulting bead slurry was rotated at 4°C for 30 min. The beads were magnetically removed, and the elution fraction was transferred to fresh low-binding tubes. A 10 µL sample of the combined elution was mixed with 10 µL of sample buffer for later analysis.

Fresh 1M dithiothreitol (DTT) was prepared and used to make Buffer A: 20 mM K_2PO_4, 10% glycerol, 0.5 mM EDTA, 1 mM DTT (for 5 mL, this is 1 mL 0.1 M K_2PO_4, pH 7.0, 0.5 mL glycerol, 5 µL 0.5 M EDTA, and 5 µL 1 M DTT). After sterilization with a 0.22-micron filter, 100x protease inhibitor cocktail was spiked into the buffer.

To concentrate and buffer-exchange the protein, the elution fraction was added to 10 kDa MWCO protein concentrator spin columns (Thermo Fisher 88513) and concentrated to a volume of approximately 100 µL. The concentrated protein was buffer-exchanged into Buffer A by adding prepared Buffer A on top and concentrating four times (e.g., if concentrated to 100 µL, add 100 µL, concentrate back to 100 µL, add 100 µL, concentrate to 100 µL, and so on). Finally, the protein was concentrated to a volume of 75 µL, removed from the concentrator, and mixed with 75 µL of 100% glycerol to reach 150 µL of purified protein, to be stored at -20°C.

To confirm proper protein production, an acrylamide protein gel was cast. 10 µL aliquots of each sample saved from above were briefly

heated to 95°C and cooled to room temperature, and these samples were loaded, run on the protein gel, and stained with Coomassie to confirm protein purification. A single band was visible in the elution samples.

Nanobody-MNase activity titration

An MNase activity analysis was performed to estimate the activity of the purified fusion protein. hiPSC cells were collected following non-enzymatic detachment as described above, crosslinked only with formaldehyde, quenched, washed, and flash frozen in aliquots of 5M cells. Cell pellets were resuspended in Micro-C Buffer #1, split into 1M aliquots, and then incubated with a range of either 1) commercial MNase or 2) the purified LaG16-MNase fusion protein. The cells were incubated, quenched, and reverse crosslinked, then DNA was purified as described in the MNase titration step in Goel *et al.* (*57*). Benchmarking the LaG16-MNase activity to the commercial MNase, we determined around 8 units of LaG16-MNase was required per million cells (in our case, about 2 µL of the purified protein sample per million cells).

Measuring positive supercoiling with GapRUN

Lentiviral vectors containing the GapR-GFP fusion protein (EF1α-GapR-FLAGx3-NLS-EGFP, plasmid 15 in table S3) were cloned. Plasmids for the constructs in Longo *et al.* (*17*) were not available on Addgene, so a DNA fragment (Twist Bioscience) was ordered containing a human-codon-optimized sequence encoding GapR-3xFLAG-NLS-EGFP. The GapR sequence was derived from the cDNA for CCNA 03428, a.k.a. GapR as identified in Guo *et al.* (*110*). This fragment was cloned into a Golden-Gate–compatible donor plasmid via HiFi assembly, which was then assembled with Golden Gate assembly alongside the EF1α promoter and the bGH polyadenylation signal into a second-level donor plasmid. This expression unit was Golden Gate assembled into a LentiX1 backbone. Lentivirus was produced as described above, then titer was computed by performing a serial dilution and transducing HEK293T Lenti-X cells seeded at 40k cells per well of a 96-well plate. These cells were flowed three days later, gated on positive GFP signal, and the dilution series was fit to a Poisson distribution to calculate the infectious units per µL.

To prepare cells for GapRUN, hiPSCs homozygously integrated with the two-gene circuits at *CLYBL* were cultured with or without 1 µg/mL dox for three days. On the second day of induction, cells were spinfected with the GapR virus. Namely, fresh media containing virus at an MOI of 0.8 plus 5 µg/mL polybrene (hexadimethrine bromide, Sigma-Aldrich H9268), with or without dox, was added to the cells, and the plate was spun at 1,500xg at 32°C for 90 min. Conditions without virus and without dox were included, giving 12 conditions total (virus and dox, virus only, or neither for each syntax). The day after spinfection, cells were changed to fresh media with or without dox. The following day, cells were non-enzymatically dissociated using Gentle Cell Dissociation Reagent (STEMCELL Technologies 100-1077), washed in PBS, and counted.

In advance, stock solutions of 1M HEPES-NaOH at pH 7.5, 500 mM spermidine, 5 M NaCl, 2.5 M $CaCl_2$, 0.5 M EDTA, and 0.5 M EGTA were prepared. A 100x solution of protease inhibitor cocktail (PIC, Thermo Fisher A32965) was prepared by dissolving one tablet in 500 µL of 20 mM HEPES-NaOH and 150 mM NaCl.

On the first day, 700 µL of Wash Buffer per sample was prepared: Wash Buffer is 20 mM HEPES-NaOH, 150 mM NaCl, and 0.5 mM spermidine (for 5 mL, this is 100 µL 1 M HEPES-NaOH, 150 µL 5 M NaCl, and 5 µL 500 mM spermidine). Digitonin (Cell Signaling Technologies 16359) was warmed to room temperature, pipetted to mix, then heated briefly to 95°C (e.g., in PCR tubes) before being cooled on ice. When mentioned below, Wash Buffer + PIC (100 µL Wash Buffer plus 1 µL PIC) or Complete Wash Buffer (100 µL Wash Buffer plus 1 µL PIC plus 2.5 µL digitonin) was prepared immediately before use.

10 µL Concanavalin A beads (Cell Signaling Technology 93569) per reaction were activated by magnetically separating the beads, removing the supernatant, and resuspending each in 100 µL of activation buffer (included with CST 93569). After 10 min at room temperature, the activation step was repeated, then the beads were separated and resuspended in 10 µL of activation buffer. Aliquots of 500k cells (dissociated and counted above) were washed twice with 100 µL of Wash Buffer + PIC, then resuspended in 100 µL of Wash Buffer + PIC. Each aliquot was combined with the 10 µL of activated ConA beads, mixed via trituration, and placed on a Nutator at room temperature for ten minutes.

The beads were then separated and resuspended in 50 µL of Complete Wash Buffer. Around 8 units (according to the MNase titration) of LaG16-MNase was spiked into the mixture, mixed well via trituration, and nutated overnight at 4°C.

The following day, 500 µL of Wash Buffer was prepared per sample. The beads were separated and washed twice with 200 µL of Complete Wash Buffer, transferring the beads to new PCR tubes after the first wash to reduce background signal. The beads were resuspended in 50 µL of Complete Wash Buffer, mixed gently, and placed on ice for at least two minutes. 1 µL of 150 mM $CaCl_2$ was spiked into each reaction while still on ice, and the samples were nutated at 4°C for two hours.

Before the 2 hours were up, 55 µL of Stop Buffer was prepared per sample. Stop Buffer is 340 mM NaCl, 20 mM EDTA, 10 mM EGTA, 2.5% digitonin, 50 µg/mL glycogen, and 100 µg/mL RNase A (for 500 µL, this is 17 µL 5 M NaCl, 20 µL 500 mM EDTA, 10 µL 500 mM EGTA, 12.5 µL digitonin, 1.25 µL 20 mg/mL glycogen, and 2.5 µL 20 mg/mL RNase A). The glycogen and RNase A was added last, shortly before use.

Samples were removed from the Nutator and placed on ice. 50 µL of Stop Buffer was added to each sample, mixed well via trituration, and incubated on a thermocycler for 10 min at 37°C. After transferring the samples to new low-binding 1.7-mL tubes, DNA was extracted following the Monarch Spin PCR & DNA Cleanup kit instructions for small-fragment retention (NEB T1130). DNA was eluted in 50 µL of 1x TE.

The resulting libraries were prepared following the NEBNext Ultra II DNA library kit instructions (NEB E7645), not performing size selection by following step 3B instead of 3A. Test PCRs (PCRs on 1 µL samples of the resulting pre-amplification library) were performed to determine the number of PCR cycles required to reach sequencing submission requirements, here around 13 cycles. The resulting libraries were uniquely dual-indexed and pooled for sequencing. The pooled libraries were sequenced using 2x75bp paired reads on an entire AVITI Cloudbreak Freestyle High chip (1B reads).

Paired-end reads were trimmed using *trim-galore* (version 0.6.10). Trimmed paired-end reads were aligned to the edited genomes described above using *bowtie2* (version 2.5.4) using the *--very-sensitive-local* preset. Reads were deduplicated using *gatk*'s *MarkDuplicatesSpark* (version 4.6.2.0). Bigwig files were generated using *deeptools* (version 3.5.6).

Genomic tracks were compared to control conditions that were not transduced with the GapR lentivirus. Signal in these control conditions was significantly lower than in the experimental conditions (fig. S29).

Measuring polymerase occupancy and histone marks with CUT&Tag

hiPSCs homozygously integrated with the two-gene circuits at *CLYBL* were cultured with or without 1 µg/mL dox for three days. Cells were then non-enzymatically dissociated using Gentle Cell Dissociation Reagent (STEMCELL Technologies 100-1077), washed in PBS, and counted. Four rabbit antibodies were used, targeting the following: Pol II (ser2) (Cell Signaling Technologies 13499S, RRID:AB_2798238), H3K27ac (Active Motif 39133, RRID:AB_2561016), H3K27me3 (Active Motif 91167, RRID:AB_2793791), and H3K4me3 (Active Motif 39915, RRID:AB_2687512). Aliquots of 500k cells per condition and per antibody were processed following manufacturer instructions for the CUT&Tag-IT Express kit (Active Motif 53177), with the following exceptions. First, because we had four antibody conditions per cell condition, "pre-aliquots" of 2M

cells were made with spike-in *Drosophila* nuclei (Active Motif 53168) added prior to splitting into 500k aliquots, in order to reduce spike-in noise across antibody conditions. Second, instead of using Q5 polymerase and a fixed number of cycles, we used NEBNext Ultra II Q5 (NEB M0544) and did an initial test PCR (PCRs on 1 μL samples of the pre-amplification library) to determine the number of PCR cycles. Finally, Nextera-compatible combinatorial dual-index primers (Active Motif 53155) were used to index the libraries. The pooled libraries were sequenced using 2x75bp paired reads on an entire AVITI Cloudbreak Freestyle High chip (1B reads).

Paired-end reads were trimmed using *trim-galore* (version 0.6.10). Trimmed paired-end reads were aligned to these genomes using *bowtie2* (version2.5.4) using the *--very-sensitive-local* preset. Reads were deduplicated using *gatk*'s *MarkDuplicatesSpark* (version 4.6.2.0) and were cell-number normalized based on the number of *Drosophila*-mapped reads from the spike-in nuclei. Normalized bigwig files were generated using *deeptools* (version 3.5.6).

Generation of antibody producer cell lines

To integrate two-gene antibody production cassettes, we used a Bxb1-mediated landing pad line with attP receptor site at Rogi2 in HEK293T cells (*52*). The landing pad functions analogously to the STRAIGHT-IN landing pad (*55*). The landing pad contains a truncated puromycin resistance gene missing the promoter and start codon. Upon Bxb1-mediated recombination between the attB site on the donor plasmid and attP site in the landing pad, an EF1α promoter and start codon is placed in-frame of the resistance gene, conferring recombinant cells resistance to puromycin.

To integrate the donor plasmids, the landing pad line was seeded at 100k cells per well onto 0.1% gelatin-coated 24-well plates. The following day, the cells were transfected using 450 ng of the two-gene donor plasmid and 300 ng of a CAG-Bxb1 plasmid (gift from the Wong Lab at Boston University). At 1 dpt, the cells were media changed. At 2 dpt, the cells were passaged to 0.1% gelatin-coated 6-well plates. At 3 dpt, the cells were media changed into media containing 1 μg/mL puromycin. Selection was maintained until an untransfected well was fully selected against (around 1.5 weeks). Once confluent (5–6 days of puromycin administration), cells were passaged at a split ratio of 1:10 to dilute out residual donor plasmid, at which point cells were ready for use in downstream analyses.

Measuring antibody production yields

After outgrowth and passaging of the antibody producer lines, triplicates were seeded on 6-well plates at 500k cells per well. The day after, cells were media changed into 2 mL of fresh DMEM + 10% FBS. After six days of outgrowth, 1.1 mL of supernatant was collected from every condition and centrifuged at 10k x g for 10 min to remove cell debris. The top 1.0 mL of clarified supernatant was transferred to Pierce 35 kDa PES protein concentrator columns (Thermo Scientific 88502). Each sample was centrifuged to a final volume less than 75 μL. Each concentrated sample was diluted to 75 μL with pH 7.4 PBS.

The resulting concentrated samples were processed following manufacturer instructions using a Human IgG (Total) ELISA kit (Thermo Scientific BMS2091) and an Easy-Titer Human IgG (H+L) kit (Thermo Scientific 23310). Absorbance was measured on a Tecan Infinite M1000 Pro at 450nm (ELISA) and 340nm (Easy-Titer).

Lentiviral transduction of two-gene cassettes

Lentiviruses were produced as described above. To calculate lentiviral titer, a two-fold serial dilution of the concentrated lentivirus was combined with 5 μg/mL polybrene (hexadimethrine bromide, Sigma-Aldrich H9268) and 20,000 HEK293T cells per well in a 0.1% gelatin-coated 96-well plate. The following day, cells were changed into fresh DMEM + 10% FBS. Two days later, cells were flowed. The fraction of expressing cells in each dilution condition was used to compute viral titer, assuming a Poisson process for infection. Viral titers were then used to calculate the volume of concentrated virus needed to infect cells at the desired MOI.

On the day of transduction, 5,000 HEK293T cells in suspension were co-infected with virus expressing the two-gene cassettes with each syntax at MOI of 0.8, and 3 μL of lentivirus expressing rtTA-P2A-mGreenLantern at high MOI. Cells were plated into a 96-well plate with DMEM + 10% FBS containing 5 μg/mL polybrene (hexadimethrine bromide, Sigma-Aldrich H9268). The following day, media was replaced with fresh DMEM + 10% FBS. At three days post infection, cells were passaged into 6-well plates. Once confluent, cells were flow-sorted on the Sony MA900 cell sorter for double-positive cells expressing the constitutive reporter gene and rtTA-P2A-mGreenLantern. The polyclonal sorted lines where then re-plated post-sorting and passaged consistently to maintain cells at 80% confluence or lower.

To evaluate inducibility, the post-sorted, integrated HEK293T cell lines were re-plated into a 96-well plate at 39k cells/well with DMEM + 10% FBS. The day after plating, media was replaced with DMEM + 10% FBS containing various concentrations of doxycycline from 0–1 μg/mL. Cells were flowed at three days post doxycycline treatment. Biological replicates represent different passages of the post-sorted, integrated cell lines.

Lentiviral transduction of the engineered all-in-one inducible circuits

Lentiviruses were produced as described above. To calculate lentiviral titer, a two-fold serial dilution of the concentrated lentivirus was combined with 5 μg/mL polybrene (hexadimethrine bromide, Sigma-Aldrich H9268) and 20,000 HEK293T cells per well in a 0.1% gelatin-coated 96-well plate. The following day, cells were media changed into fresh DMEM + 10% FBS containing 1 μg/mL doxycycline. Two days later, cells were flowed. The fraction of expressing cells in each dilution condition was used to compute viral titer, assuming a Poisson process for infection. Viral titers for iPS11 cells and mouse embryonic fibroblasts (MEFs) were estimated as two-fold greater or four-fold lower, respectively, than for HEK293T cells. Viral titers were then used to calculate the volume of concentrated virus needed to infect cells at an MOI of 0.3.

To transduce HEK293T cells, 20,000 cells were combined with 5 μg/mL polybrene and the calculated amount of concentrated virus. The next day, cells were media changed into fresh DMEM + 10% FBS with or without 300 ng/mL dox. Two days later, cells were flowed.

To transduce iPS11 cells, cells were dissociated with Gentle Cell Dissociation Reagent according to manufacturer's instructions, then seeded at 15,000 cells/well in a Geltrex-coated 96-well plate with mTeSR-Plus and 5 μM ROCKi. The next day, the media was replaced with fresh mTeSR-Plus containing the calculated amount of concentrated virus and 5 μg/mL polybrene. Plates were then spun at 1500 × g for 90 min. The following day, media was changed to fresh mTeSR-Plus with or without 300 ng/mL dox. Two days later, cells were imaged and flowed.

To transduce MEFs, passage 1 primary MEFs—isolated from E12.5–E14.5 embryos of C57BL/6 mice, as described in Wang *et al.* (*92*)—were thawed and allowed to recover for 1–2 days in DMEM + 10% FBS. Cells were then dissociated with Trypsin-EDTA and seeded at 10k cells per well in a 0.1% gelatin-coated 96-well plate. The following day, the media was replaced with fresh DMEM + 10% FBS containing the calculated amount of concentrated virus and 5 μg/mL polybrene. Plates were then spun at 1500 × g for 90 min. The following day, media was changed to fresh DMEM + 10% FBS with or without 300 ng/mL dox. Two days later, cells were flowed. Biological replicates include cells from multiple independent isolations.

Flow cytometry

Hanks' Balanced Salt Solution (HBSS) supplemented with 2% FBS (PiggyBac-integrated iPS11 cells) or PBS (all others) was used as Flow buffer. Cells were washed once with PBS, then dissociated with Trypsin-EDTA (HEK293T, MEFs), TrypLE Express (iPS11), or Gentle Cell Dissociation Reagent (iPS11). After dissociation, cells were quenched with

Flow buffer or media, then spun down for 5 min at 300–500 × g. Cells were resuspended in Flow buffer and acquired on CytoFLEX LX N3-V5-B3-Y5-R3-I0 (Beckman Coulter) or Attune NxT Flow Cytometer (Thermo Fisher). Data were gated for single cells on FlowJo (v10.X; BD Biosciences) or CytExpert (v2.6; Beckman Coulter) software, then gated events were exported for plotting and additional analysis.

Intrinsic and extrinsic noise analysis

For every figure except fig. S23, we first log-transform each of the gene expression levels before computing the intrinsic and extrinsic noise. This log-transform ensures that changes in the values correspond to fold change in protein concentration independent of fluorescent protein quantum yield and PMT values for cytometry channels. We calculate the variance

$$\mathrm{var}(\vec{x}) = \frac{1}{n}\sum_{i=1}^{N}(x_i - \bar{x})^2$$

of the sum and difference of the values for each gene. The intrinsic noise is the variance of the difference of the log-transformed expression levels. The extrinsic noise is the variance of the sum of the log-transformed expression levels. The intrinsic and extrinsic noise between genes a and b is thus:

$$n_{\mathrm{intrinsic}} = \mathrm{var}\left[\log(\vec{a}) - \log(\vec{b})\right]$$

$$n_{\mathrm{extrinsic}} = \mathrm{var}\left[\log(\vec{a}) + \log(\vec{b})\right]$$

Dividing the intrinsic noise by the extrinsic noise gives the intrinsic-to-extrinsic noise ratio. For fig. S23, we do not log-transform the data, and instead compute:

$$n_{\mathrm{intrinsic}} = \mathrm{var}(\vec{a} - \vec{b})$$

$$n_{\mathrm{extrinsic}} = \mathrm{var}(\vec{a} + \vec{b})$$

$$\mathrm{noise\ ratio} = n_{\mathrm{intrinsic}} / n_{\mathrm{extrinsic}}$$

Copy number quantification with droplet digital PCR

The copy number of the PiggyBac-integrated fluorescent reporter lines (fig. S30A) and the Rogi2-integrated antibody production lines (fig. S30B) was evaluated using Bio-Rad's QX200 Droplet Digital PCR system.

Briefly, two sets of fluorescent PCR probes were ordered, targeting the *mRuby2* coding sequence with the FAM fluorophore and targeting *RPP30*, a native gene on chromosome 10, with the HEX fluorophore. Genomic DNA was isolated from the cell lines of interest and diluted to an appropriate concentration for PCR. The Bio-Rad droplet digital PCR (ddPCR) system was used to generate nanoliter-sized reaction droplets, perform PCR, and read out the resulting droplet fluorescence. Then, the fractions of the double-positive and single-positive populations were fit to a Poisson distribution. Because the *RPP30* gene has a known copy number (~2.7 in HEK293T cells), the Poisson fits give an estimate of the mean and variance in copy number of the *mRuby2* gene. As the *mRuby2* gene is present once in each of the integrated constructs, this allows us to calculate the total number of integrations.

For the PiggyBac integrated lines (fig. S30A), we observe copy numbers between 4 and 18, with the divergent syntax having the lowest copy number despite having the highest expression. For the Rogi2 antibody production lines (fig. S30B), we expect a single integration and observe copy numbers between 1 and 1.4. The fractional copy numbers come from the relative genomic instability of the HEK293T cells. As the HEK293T cells divide, chromosomal rearrangements and duplications can occur, making the population heterogeneous. Still, the antibody production lines with the highest titer have the lowest copy number.

REFERENCES AND NOTES

1. F. Darbellay *et al.*, The constrained architecture of mammalian *Hox* gene clusters. *Proc. Natl. Acad. Sci. U.S.A.* **116**, 13424–13433 (2019). doi: 10.1073/pnas.1904602116; pmid: 31209053
2. S. E. Murphy, A. N. Boettiger, Polycomb repression of Hox genes involves spatial feedback but not domain compaction or phase transition. *Nat. Genet.* **56**, 493–504 (2024). doi: 10.1038/s41588-024-01661-6; pmid: 38361032
3. O. Q. H. Zinani, K. Keseroğlu, A. Ay, E. M. Özbudak, Pairing of segmentation clock genes drives robust pattern formation. *Nature* **589**, 431–436 (2021). doi: 10.1038/s41586-020-03055-0; pmid: 33361814
4. A. Gherman, R. Wang, D. Avramopoulos, Orientation, distance, regulation and function of neighbouring genes. *Hum. Genomics* **3**, 143–156 (2009). doi: 10.1186/1479-7364-3-2-143; pmid: 19164091
5. N. D. Trinklein *et al.*, An abundance of bidirectional promoters in the human genome. *Genome Res.* **14**, 62–66 (2004). doi: 10.1101/gr.1982804; pmid: 14707170
6. J. O. Korbel, L. J. Jensen, C. von Mering, P. Bork, Analysis of genomic context: Prediction of functional associations from conserved bidirectionally transcribed gene pairs. *Nat. Biotechnol.* **22**, 911–917 (2004). doi: 10.1038/nbt988; pmid: 15229555
7. C. P. Johnstone, K. E. Galloway, Supercoiling-mediated feedback rapidly couples and tunes transcription. *Cell Rep.* **41**, 111492 (2022). doi: 10.1016/j.celrep.2022.111492; pmid: 36261020
8. S. Brahmachari, S. Tripathi, J. N. Onuchic, H. Levine, Nucleosomes play a dual role in regulating transcription dynamics. *Proc. Natl. Acad. Sci. U.S.A.* **121**, e2319772121 (2024). doi: 10.1073/pnas.2319772121; pmid: 38968124
9. Y.-P. Tsao, H.-Y. Wu, L. F. Liu, Transcription-driven supercoiling of DNA: Direct biochemical evidence from in vitro studies. *Cell* **56**, 111–118 (1989). doi: 10.1016/0092-8674(89)90989-6; pmid: 2535966
10. R. Janissen, R. Barth, M. Polinder, J. van der Torre, C. Dekker, Single-molecule visualization of twin-supercoiled domains generated during transcription. *Nucleic Acids Res.* **52**, 1677–1687 (2024). doi: 10.1093/nar/gkad1181; pmid: 38084930
11. H. P. Patel *et al.*, DNA supercoiling restricts the transcriptional bursting of neighboring eukaryotic genes. *Mol. Cell* **83**, 1573–1587.e8 (2023). doi: 10.1016/j.molcel.2023.04.015; pmid: 37207624
12. M. Ancona, A. Bentivoglio, C. A. Brackley, G. Gonnella, D. Marenduzzo, Transcriptional Bursts in a Nonequilibrium Model for Gene Regulation by Supercoiling. *Biophys. J.* **117**, 369–376 (2019). doi: 10.1016/j.bpj.2019.04.023; pmid: 31103229
13. Y. Geng *et al.*, A spatially resolved stochastic model reveals the role of supercoiling in transcription regulation. *PLOS Comput. Biol.* **18**, e1009788 (2022). doi: 10.1371/journal.pcbi.1009788; pmid: 36121892
14. J. Ma *et al.*, Transcription factor regulation of RNA polymerase's torque generation capacity. *Proc. Natl. Acad. Sci. U.S.A.* **116**, 2583–2588 (2019). doi: 10.1073/pnas.1807031116; pmid: 30635423
15. J. Qian *et al.*, Chromatin Buffers Torsional Stress During Transcription. bioRxiv 2024.10.15.618270 [Preprint] (2024); https://doi.org/10.1101/2024.10.15.618270.
16. M. Bhola *et al.*, RNA interacts with topoisomerase I to adjust DNA topology. *Mol. Cell* **84**, 3192–3208.e11 (2024). doi: 10.1016/j.molcel.2024.07.032; pmid: 39173639
17. G. M. C. Longo *et al.*, Type II topoisomerases shape multi-scale 3D chromatin folding in regions of positive supercoils. *Mol. Cell* **84**, 4267–4281.e8 (2024). doi: 10.1016/j.molcel.2024.10.007; pmid: 39486417
18. J. Lee *et al.*, Chromatinization modulates topoisomerase II processivity. *Nat. Commun.* **14**, 6844 (2023). doi: 10.1038/s41467-023-42600-z; pmid: 37891161
19. S. Saha, Y. Pommier, R-loops, type I topoisomerases and cancer. *NAR Cancer* **5**, zcad013 (2023). doi: 10.1093/narcan/zcad013; pmid: 37600974
20. D. Sutormin *et al.*, Interaction between transcribing RNA polymerase and topoisomerase I prevents R-loop formation in E. coli. *Nat. Commun.* **13**, 4524 (2022). doi: 10.1038/s41467-022-32106-5; pmid: 35927234
21. T. T. Le *et al.*, Synergistic Coordination of Chromatin Torsional Mechanics and Topoisomerase Activity. *Cell* **179**, 619–631.e15 (2019). doi: 10.1016/j.cell.2019.09.034; pmid: 31626768
22. Q. Yao, L. Zhu, Z. Shi, S. Banerjee, C. Chen, Topoisomerase-modulated genome-wide DNA supercoiling domains colocalize with nuclear compartments and regulate human gene expression. *Nat. Struct. Mol. Biol.* **32**, 48–61 (2025). doi: 10.1038/s41594-024-01377-5; pmid: 39152238
23. S. Corless, N. Gilbert, Effects of DNA supercoiling on chromatin architecture. *Biophys. Rev.* **8**, 245–258 (2016). doi: 10.1007/s12551-016-0210-1; pmid: 27738453
24. Y. J. Achar, M. Adhil, R. Choudhary, N. Gilbert, M. Foiani, Negative supercoil at gene boundaries modulates gene topology. *Nature* **577**, 701–705 (2020). doi: 10.1038/s41586-020-1934-4; pmid: 31969709
25. C. Naughton *et al.*, Transcription forms and remodels supercoiling domains unfolding large-scale chromatin structures. *Nat. Struct. Mol. Biol.* **20**, 387–395 (2013). doi: 10.1038/nsmb.2509; pmid: 23416946
26. A. Revyakin, R. H. Ebright, T. R. Strick, Promoter unwinding and promoter clearance by RNA polymerase: Detection by single-molecule DNA nanomanipulation. *Proc. Natl. Acad. Sci. U.S.A.* **101**, 4776–4780 (2004). doi: 10.1073/pnas.0307241101; pmid: 15037753

27. I. Boulas *et al.*, Assessing in vivo the impact of gene context on transcription through DNA supercoiling. *Nucleic Acids Res.* **51**, 9509–9521 (2023). doi: 10.1093/nar/gkad688; pmid: 37667073
28. J. F. Marko, Torque and dynamics of linking number relaxation in stretched supercoiled DNA. *Phys. Rev. E Stat. Nonlin. Soft Matter Phys.* **76**, 021926 (2007). doi: 10.1103/PhysRevE.76.021926; pmid: 17930084
29. S. A. Sevier, H. Levine, Mechanical Properties of Transcription. *Phys. Rev. Lett.* **118**, 268101 (2017). doi: 10.1103/PhysRevLett.118.268101; pmid: 28707908
30. W. C. Hacker, A. H. Elcock, spotter: A single-nucleotide resolution stochastic simulation model of supercoiling-mediated transcription and translation in prokaryotes. *Nucleic Acids Res.* **51**, e92 (2023). doi: 10.1093/nar/gkad682; pmid: 37602419
31. S. Chong, C. Chen, H. Ge, X. S. Xie, Mechanism of transcriptional bursting in bacteria. *Cell* **158**, 314–326 (2014). doi: 10.1016/j.cell.2014.05.038; pmid: 25036631
32. E. Yeung *et al.*, Biophysical Constraints Arising from Compositional Context in Synthetic Gene Networks. *Cell Syst.* **5**, 11–24.e12 (2017). doi: 10.1016/j.cels.2017.06.001; pmid: 28734826
33. S. S. Teves, S. Henikoff, Transcription-generated torsional stress destabilizes nucleosomes. *Nat. Struct. Mol. Biol.* **21**, 88–94 (2014). doi: 10.1038/nsmb.2723; pmid: 24317489
34. M. S. Guo, R. Kawamura, M. L. Littlehale, J. F. Marko, M. T. Laub, High-resolution, genome-wide mapping of positive supercoiling in chromosomes. *eLife* **10**, e67236 (2021). doi: 10.7554/eLife.67236; pmid: 34279217
35. H.-S. Li *et al.*, Multidimensional control of therapeutic human cell function with synthetic gene circuits. *Science* **378**, 1227–1234 (2022). doi: 10.1126/science.ade0156; pmid: 36520914
36. K. S. Love *et al.*, Model-guided design of microRNA-based gene circuits supports precise dosage of transgenic cargoes into diverse primary cells. *Cell Syst.* **16**, 101269 (2025). doi: 10.1016/j.cels.2025.101269; pmid: 40300600
37. J. H. Cho *et al.*, Engineering advanced logic and distributed computing in human CAR immune cells. *Nat. Commun.* **12**, 792 (2021). doi: 10.1038/s41467-021-21078-7; pmid: 33542232
38. A. V. Anzalone *et al.*, Search-and-replace genome editing without double-strand breaks or donor DNA. *Nature* **576**, 149–157 (2019). doi: 10.1038/s41586-019-1711-4; pmid: 31634902
39. P. Mali *et al.*, RNA-guided human genome engineering via Cas9. *Science* **339**, 823–826 (2013). doi: 10.1126/science.1232033; pmid: 23287722
40. L. Cong *et al.*, Multiplex genome engineering using CRISPR/Cas systems. *Science* **339**, 819–823 (2013). doi: 10.1126/science.1231143; pmid: 23287718
41. A. M. Tousley *et al.*, Co-opting signalling molecules enables logic-gated control of CAR T cells. *Nature* **615**, 507–516 (2023). doi: 10.1038/s41586-023-05778-2; pmid: 36890224
42. G. M. Allen *et al.*, Synthetic cytokine circuits that drive T cells into immune-excluded tumors. *Science* **378**, eaba1624 (2022). doi: 10.1126/science.aba1624; pmid: 36520915
43. W. Gao *et al.*, Engineered T cell therapy for central nervous system injury. *Nature* **634**, 693–701 (2024). doi: 10.1038/s41586-024-07906-y; pmid: 39232158
44. V. S. Ganesh *et al.*, Neurodevelopmental Disorder Caused by Deletion of *CHASERR*, a lncRNA Gene. *N. Engl. J. Med.* **391**, 1511–1518 (2024). doi: 10.1056/NEJMoa2400718; pmid: 39442041
45. A. Rom *et al.*, Regulation of CHD2 expression by the Chaserr long noncoding RNA gene is essential for viability. *Nat. Commun.* **10**, 5092 (2019). doi: 10.1038/s41467-019-13075-8; pmid: 31704914
46. J. A. Martens, L. Laprade, F. Winston, Intergenic transcription is required to repress the Saccharomyces cerevisiae SER3 gene. *Nature* **429**, 571–574 (2004). doi: 10.1038/nature02538; pmid: 15175754
47. Z. Tang *et al.*, CTCF-Mediated Human 3D Genome Architecture Reveals Chromatin Topology for Transcription. *Cell* **163**, 1611–1627 (2015). doi: 10.1016/j.cell.2015.11.024; pmid: 26686651
48. M. Liu *et al.*, Genomic discovery of potent chromatin insulators for human gene therapy. *Nat. Biotechnol.* **33**, 198–203 (2015). doi: 10.1038/nbt.3062; pmid: 25580597
49. X.-B. Lu, Y.-H. Guo, W. Huang, Characterization of the cHS4 insulator in mouse embryonic stem cells. *FEBS Open Bio* **10**, 644–656 (2020). doi: 10.1002/2211-5463.12818; pmid: 32087050
50. S. Zhang, N. Übelmesser, M. Barbieri, A. Papantonis, Enhancer-promoter contact formation requires RNAPII and antagonizes loop extrusion. *Nat. Genet.* **55**, 832–840 (2023). doi: 10.1038/s41588-023-01364-4; pmid: 37012454
51. E. Calvo-Roitberg *et al.*, mRNA initiation and termination are spatially coordinated. *Science* **390**, eado8279 (2025). doi: 10.1126/science.ado8279; pmid: 41066574
52. E. L. Peterman *et al.*, High-resolution profiling reveals coupled transcriptional and translational regulation of transgenes. *Nucleic Acids Res.* **53**, gkaf528 (2025). doi: 10.1093/nar/gkaf528; pmid: 40530694
53. H. M. T. Choi, V. A. Beck, N. A. Pierce, Next-generation in situ hybridization chain reaction: Higher gain, lower cost, greater durability. *ACS Nano* **8**, 4284–4294 (2014). doi: 10.1021/nn405717p; pmid: 24712299
54. C. Björkegren, L. Baranello, DNA Supercoiling, Topoisomerases, and Cohesin: Partners in Regulating Chromatin Architecture? *Int. J. Mol. Sci.* **19**, 884 (2018). doi: 10.3390/ijms19030884; pmid: 29547555
55. A. Blanch-Asensio *et al.*, STRAIGHT-IN Dual: A Platform for Dual, Single-Copy Integrations of DNA Payloads and Gene Circuits into Human Induced Pluripotent Stem Cells. bioRxiv 2024.10.17.616637 [Preprint] (2024); https://doi.org/10.1101/2024.10.17.616637.
56. T. Cerbini *et al.*, Transcription activator-like effector nuclease (TALEN)-mediated CLYBL targeting enables enhanced transgene expression and one-step generation of dual reporter human induced pluripotent stem cell (iPSC) and neural stem cell (NSC) lines. *PLOS ONE* **10**, e0116032 (2015). doi: 10.1371/journal.pone.0116032; pmid: 25587899
57. V. Y. Goel, M. K. Huseyin, A. S. Hansen, Region Capture Micro-C reveals coalescence of enhancers and promoters into nested microcompartments. *Nat. Genet.* **55**, 1048–1056 (2023). doi: 10.1038/s41588-023-01391-1; pmid: 37157000
58. N. Abdennur *et al.*, Cooltools: Enabling high-resolution Hi-C analysis in Python. *PLOS Comput. Biol.* **20**, e1012067 (2024). doi: 10.1371/journal.pcbi.1012067; pmid: 38709825
59. M. Zufferey, D. Tavernari, E. Oricchio, G. Ciriello, Comparison of computational methods for the identification of topologically associating domains. *Genome Biol.* **19**, 217 (2018). doi: 10.1186/s13059-018-1596-9; pmid: 30526631
60. D. N. Narducci, A. S. Hansen, Reeling it in: How DNA topology drives loop extrusion by condensin. *Nat. Struct. Mol. Biol.* **29**, 623–625 (2022). doi: 10.1038/s41594-022-00805-8; pmid: 35835869
61. Y. Guo *et al.*, Chromatin jets define the properties of cohesin-driven in vivo loop extrusion. *Mol. Cell* **82**, 3769–3780.e5 (2022). doi: 10.1016/j.molcel.2022.09.003; pmid: 36182691
62. Z. Fu, M. S. Guo, W. Zhou, J. Xiao, Differential roles of positive and negative supercoiling in organizing the E. coli genome. *Nucleic Acids Res.* **52**, 724–737 (2024). doi: 10.1093/nar/gkad1139; pmid: 38050973
63. J. J. Gam, B. DiAndreth, R. D. Jones, J. Huh, R. Weiss, A 'poly-transfection' method for rapid, one-pot characterization and optimization of genetic systems. *Nucleic Acids Res.* **47**, e106 (2019). doi: 10.1093/nar/gkz623; pmid: 31372658
64. K. Rai *et al.*, Ultra-high-throughput mapping of genetic design space. *Nature* **650**, 1035–1044 (2026). doi: 10.1038/s41586-025-09933-9; pmid: 41535463
65. S. Schlatter *et al.*, On the optimal ratio of heavy to light chain genes for efficient recombinant antibody production by CHO cells. *Biotechnol. Prog.* **21**, 122–133 (2005). doi: 10.1021/bp049780w; pmid: 15903249
66. R. Hooft van Huijsduijnen *et al.*, Reassessing therapeutic antibodies for neglected and tropical diseases. *PLOS Negl. Trop. Dis.* **14**, e0007860 (2020). doi: 10.1371/journal.pntd.0007860; pmid: 31999695
67. J. Carver *et al.*, Maximizing antibody production in a targeted integration host by optimization of subunit gene dosage and position. *Biotechnol. Prog.* **36**, e2967 (2020). doi: 10.1002/btpr.2967; pmid: 31965756
68. Z. Lee, J. Wan, A. Shen, G. Barnard, Gene copy number, gene configuration and LC/HC mRNA ratio impact on antibody productivity and product quality in targeted integration CHO cell lines. *Biotechnol. Prog.* **40**, e3433 (2024). doi: 10.1002/btpr.3433; pmid: 38321634
69. S. C. L. Ho *et al.*, Control of IgG LC:HC ratio in stably transfected CHO cells and study of the impact on expression, aggregation, glycosylation and conformational stability. *J. Biotechnol.* **165**, 157–166 (2013). doi: 10.1016/j.jbiotec.2013.03.019; pmid: 23583871
70. E. Ascic *et al.*, In vivo dendritic cell reprogramming for cancer immunotherapy. *Science* **386**, eadn9083 (2024). doi: 10.1126/science.adn9083; pmid: 39236156
71. Z. Chen *et al.*, A synthetic protein-level neural network in mammalian cells. *Science* **386**, 1243–1250 (2024). doi: 10.1126/science.add8468; pmid: 39666795
72. K. Galloway, C. Johnstone, Bringing neural networks to life. *Science* **386**, 1225–1226 (2024). doi: 10.1126/science.adu1327; pmid: 39666818
73. M. B. Elowitz, A. J. Levine, E. D. Siggia, P. S. Swain, Stochastic gene expression in a single cell. *Science* **297**, 1183–1186 (2002). doi: 10.1126/science.1070919; pmid: 12183631
74. M. P. Swaffer *et al.*, RNA polymerase II dynamics and mRNA stability feedback scale mRNA amounts with cell size. *Cell* **186**, 5254–5268.e26 (2023). doi: 10.1016/j.cell.2023.10.012; pmid: 37944513
75. A. Cabrera *et al.*, The sound of silence: Transgene silencing in mammalian cell engineering. *Cell Syst.* **13**, 950–973 (2022). doi: 10.1016/j.cels.2022.11.005; pmid: 36549273
76. K. Yahata *et al.*, cHS4 insulator-mediated alleviation of promoter interference during cell-based expression of tandemly associated transgenes. *J. Mol. Biol.* **374**, 580–590 (2007). doi: 10.1016/j.jmb.2007.09.054; pmid: 17945255
77. P. Guye, Y. Li, L. Wroblewska, X. Duportet, R. Weiss, Rapid, modular and reliable construction of complex mammalian gene circuits. *Nucleic Acids Res.* **41**, e156 (2013). doi: 10.1093/nar/gkt605; pmid: 23847100
78. E. J. K. Kowal, Y. Sakai, M. P. McGurk, Z. J. Pasetsky, C. B. Burge, Sequence-dependent and -independent effects of intron-mediated enhancement learned from thousands of random introns. *Nucleic Acids Res.* **53**, gkaf097 (2025). doi: 10.1093/nar/gkaf097; pmid: 39995040
79. R. V. Desai *et al.*, A DNA repair pathway can regulate transcriptional noise to promote cell fate transitions. *Science* **373**, eabc6506 (2021). doi: 10.1126/science.abc6506; pmid: 34301855
80. C. P. Johnstone, K. E. Galloway, Engineering cellular symphonies out of transcriptional noise. *Nat. Rev. Mol. Cell Biol.* **22**, 369–370 (2021). doi: 10.1038/s41580-021-00359-5; pmid: 33723437

81. F. Kouzine *et al.*, Transcription-dependent dynamic supercoiling is a short-range genomic force. *Nat. Struct. Mol. Biol.* **20**, 396–403 (2013). doi: 10.1038/nsmb.2517; pmid: 23416947
82. K. M. Beal *et al.*, The impact of expression vector position on transgene transcription allows for rational expression vector design in a targeted integration system. *Biotechnol. J.* **18**, e2300038 (2023). doi: 10.1002/biot.202300038; pmid: 37272404
83. L. E. Fry *et al.*, Promoter Orientation within an AAV-CRISPR Vector Affects Cas9 Expression and Gene Editing Efficiency. *CRISPR J.* **3**, 276–283 (2020). doi: 10.1089/crispr.2020.0021; pmid: 32833533
84. B. Castel, L. Tomlinson, F. Locci, Y. Yang, J. D. G. Jones, Optimization of T-DNA architecture for Cas9-mediated mutagenesis in Arabidopsis. *PLOS ONE* **14**, e0204778 (2019). doi: 10.1371/journal.pone.0204778; pmid: 30625150
85. R. Du *et al.*, miRNA modules for precise, tunable control of gene expression. *Mol. Cell* **86**, 194–212.e7 (2026). doi: 10.1016/j.molcel.2025.11.028; pmid: 41421338
86. S. R. Kabaria *et al.*, Programmable promoter editing for precise control of transgene expression. *Nat. Biotechnol.* 1–16 (2025). doi: 10.1038/s41587-025-02854-y; pmid: 41083901
87. M. Mark, F. M. Rijli, P. Chambon, Homeobox genes in embryogenesis and pathogenesis. *Pediatr. Res.* **42**, 421–429 (1997). doi: 10.1203/00006450-199710000-00001; pmid: 9380431
88. J. S. Mattick, Non-coding RNAs: The architects of eukaryotic complexity. *EMBO Rep.* **2**, 986–991 (2001). doi: 10.1093/embo-reports/kve230; pmid: 11713189
89. P. P. Amaral, M. E. Dinger, T. R. Mercer, J. S. Mattick, The eukaryotic genome as an RNA machine. *Science* **319**, 1787–1789 (2008). doi: 10.1126/science.1155472; pmid: 18369136
90. J. M. Engreitz *et al.*, Local regulation of gene expression by lncRNA promoters, transcription and splicing. *Nature* **539**, 452–455 (2016). doi: 10.1038/nature20149; pmid: 27783602
91. S. K. Aoki *et al.*, A universal biomolecular integral feedback controller for robust perfect adaptation. *Nature* **570**, 533–537 (2019). doi: 10.1038/s41586-019-1321-1; pmid: 31217585
92. N. B. Wang *et al.*, Proliferation history and transcription factor levels drive direct conversion to motor neurons. *Cell Syst.* **16**, 101205 (2025). doi: 10.1016/j.cels.2025.101205; pmid: 40086434
93. M. M. K. Hansen *et al.*, A Post-Transcriptional Feedback Mechanism for Noise Suppression and Fate Stabilization. *Cell* **173**, 1609–1621.e15 (2018). doi: 10.1016/j.cell.2018.04.005; pmid: 29754821
94. J. Tycko *et al.*, High-Throughput Discovery and Characterization of Human Transcriptional Effectors. *Cell* **183**, 2020–2035.e16 (2020). doi: 10.1016/j.cell.2020.11.024; pmid: 33326746
95. L. Oesinghaus, S. Castillo-Hair, N. Ludwig, A. Keller, G. Seelig, Quantitative Design of Cell Type-Specific mRNA Stability from microRNA Expression Data. bioRxiv 2024.10.28.620728 [Preprint] (2024); https://doi.org/10.1101/2024.10.28.620728.
96. W. Vanderlinden, E. Skoruppa, P. J. Kolbeck, E. Carlon, J. Lipfert, DNA fluctuations reveal the size and dynamics of topological domains. *PNAS Nexus* **1**, pgac268 (2022). doi: 10.1093/pnasnexus/pgac268; pmid: 36712371
97. E. Kim, A. M. Gonzalez, B. Pradhan, J. van der Torre, C. Dekker, Condensin-driven loop extrusion on supercoiled DNA. *Nat. Struct. Mol. Biol.* **29**, 719–727 (2022). doi: 10.1038/s41594-022-00802-x; pmid: 35835864
98. X. Gao, Y. Hong, F. Ye, J. T. Inman, M. D. Wang, Torsional Stiffness of Extended and Plectonemic DNA. *Phys. Rev. Lett.* **127**, 028101 (2021). doi: 10.1103/PhysRevLett.127.028101; pmid: 34296898
99. S. Corless, C. Naughton, N. Gilbert, Profiling DNA supercoiling domains in vivo. *Genom. Data* **2**, 264–267 (2014). doi: 10.1016/j.gdata.2014.07.007; pmid: 26484106
100. S. Corless, N. Gilbert, Investigating DNA supercoiling in eukaryotic genomes. *Brief. Funct. Genomics* **16**, 379–389 (2017). doi: 10.1093/bfgp/elx007; pmid: 28444308
101. B. J. Visser, D. Bates, "In Vivo Genomic Supercoiling Mapping Using Psora-seq" in *Bacterial Chromatin: Methods and Protocols*, R. T. Dame, Ed. (Springer US, 2024), pp. 147–156.
102. K. E. Shearwin, B. P. Callen, J. B. Egan, Transcriptional interference—A crash course. *Trends Genet.* **21**, 339–345 (2005). doi: 10.1016/j.tig.2005.04.009; pmid: 15922833
103. A. N. Brooks *et al.*, Transcriptional neighborhoods regulate transcript isoform lengths and expression levels. *Science* **375**, 1000–1005 (2022). doi: 10.1126/science.abg0162; pmid: 35239377
104. B. Goldberg, N. Yehya, J. Xiao, S. Meyer, Differential effect of supercoiling on bacterial transcription in topological domains. *PLOS Comput. Biol.* **21**, e1012764 (2025). doi: 10.1371/journal.pcbi.1012764; pmid: 41218075
105. A. K. Morao, A. Chervova, Y. Zhao, S. Ercan, G. Cecere, DNA Supercoiling Modulates Eukaryotic Transcription in a Gene-Orientation Dependent Manner. bioRxiv 2025.01.03.631213 [Preprint] (2025); https://doi.org/10.1101/2025.01.03.631213.
106. K. Yusa, L. Zhou, M. A. Li, A. Bradley, N. L. Craig, A hyperactive piggyBac transposase for mammalian applications. *Proc. Natl. Acad. Sci. U.S.A.* **108**, 1531–1536 (2011). doi: 10.1073/pnas.1008322108; pmid: 21205896
107. E. Aznauryan *et al.*, Discovery and validation of human genomic safe harbor sites for gene and cell therapies. *Cell Rep. Methods* **2**, 100154 (2022). doi: 10.1016/j.crmeth.2021.100154; pmid: 35474867
108. T. Yang *et al.*, HiCRep: Assessing the reproducibility of Hi-C data using a stratum-adjusted correlation coefficient. *Genome Res.* **27**, 1939–1949 (2017). doi: 10.1101/gr.220640.117; pmid: 28855260
109. S. Koidl, H. T. M. Timmers, greenCUT&RUN: Efficient Genomic Profiling of GFP-Tagged Transcription Factors and Chromatin Regulators. *Curr. Protoc.* **1**, e266 (2021). doi: 10.1002/cpz1.266; pmid: 34644460
110. M. S. Guo, D. L. Haakonsen, W. Zeng, M. A. Schumacher, M. T. Laub, A Bacterial Chromosome Structuring Protein Binds Overtwisted DNA to Stimulate Type II Topoisomerases and Enable DNA Replication. *Cell* **175**, 583–597.e23 (2018). doi: 10.1016/j.cell.2018.08.029; pmid: 30220456
111. C. P. Johnstone, K. S. Love, K. E. Galloway, Gene syntax defines supercoiling-mediated transcriptional feedback [dataset], version 1, Zenodo (2026); https://doi.org/10.5281/zenodo.18226480.

ACKNOWLEDGMENTS

We thank M. Oliveira de Souza for providing the antibody-encoding plasmids used for the antibody work. We thank the MIT BioMicro Center for their support with the sequencing-based assays in this study. We thank M. Laub and A. Hansen for their feedback. We thank M. Ehmann, M. Castellanos, and N. Wang for reviewing the manuscript. **Funding:** National Institutes of Health (NIH) NIGMS R35-GM143033 (K.E.G.); NIH R01AI181684 and R21AI166396 (B.J.D.); National Science Foundation (NSF) CAREER 2339986 (K.E.G.) with Institute for Collaborative Biotechnologies W911NF-19-20026 (K.E.G.); Air Force Research Laboratory MURI (FA9550-22-1-0316) (K.E.G.); NSF GRFP 1745302 (K.S.L., S.R.K., E.L.P); Michael Smith Health Research BC trainee award RT-2021-1946 (R.D.J.); MSL Pathway to Independence Award (R.D.J.); Stem Cell Network (P.W.Z.); Canadian Institute for Health Research (P.W.Z.); WellcomeLeap Human Organs, Physiology, and Engineering (HOPE) program (P.W.Z.); Canada Research Chair in Stem Cell Bioengineering (P.W.Z.); Novo Nordisk Foundation renew NNF21CC0073729 (P.W.Z, C.L.M., R.D., A.B.A.); National Cancer Institute, Koch Institute Support (core) Grant P30-CA14051 (BioMicroCenter: core sequencing facility); NIH P30-ES002109 (BioMicroCenter: core sequencing facility). **Author contributions:** Conceptualization: C.P.J., K.S.L., R.D.J., A.B.A., D.S.P., B.J.D., K.E.G.; Methodology: C.P.J., K.S.L., R.D.J., A.B.A., D.S.P., C.G.O., B.J.D., K.E.G.; Investigation: C.P.J., K.S.L., S.R.K., R.D.J., A.B.A., D.S.P., E.L.P., R.L., J.Y.; Validation: C.P.J., K.S.L., K.E.G.; Statistical analysis: C.P.J., K.S.L.; Visualization: C.P.J., K.S.L., R.D.J.; Writing — original draft: C.P.J.; Writing — review & editing: C.P.J., K.S.L., S.R.K., A.B.A., D.S.P., E.L.P., R.L., C.G.O., C.L.M., B.J.D., P.W.Z., K.E.G.; Resources: C.L.M., B.J.D., P.W.Z., K.E.G. K.E.G.; Supervision: C.L.M., P.W.Z., K.E.G.; Funding acquisition: C.L.M., P.W.Z., K.E.G.; Project administration: P.W.Z., K.E.G. **Competing interests:** B.J.D. is an inventor on a provisional patent application related to the anti–yellow fever antibody. **Data, code, and materials availability:** All data, code, and scripts for all figures are deposited at Zenodo (*111*). Data include flow cytometry, ddPCR, and microscopy data as well as processed sequencing data. Code includes all NGS pipelines, data analysis code, and scripts to generate all figures. Raw sequencing reads have been deposited at GEO under the following accession numbers: GSE316692 (RNA-seq), GSE316693 (RCMC), GSE316694 (GapRUN), and GSE316695 (CUT&Tag). All plasmids related to main-text figures have been deposited at Addgene; all other plasmids and materials used in this study will be made available upon request.

SUPPLEMENTARY MATERIALS

science.org/doi/10.1126/science.adw1925
Figs. S1 to S30; Tables S1 to S5; MDAR Reproducibility Checklist; Movie S1
Submitted 22 January 2025; resubmitted 25 November 2025; accepted 30 January 2026
10.1126/science.adw1925

Science
AAAS

Supplementary Materials for

Gene syntax defines supercoiling-mediated transcriptional feedback

Christopher P. Johnstone *et al*.

Corresponding author: Kate E. Galloway, katiegal@mit.edu

Science **392**, eadw1925 (2026)
DOI: 10.1126/science.adw1925

The PDF file includes:

Figs. S1 to S30
Tables S1 to S5

Other Supplementary Material for this manuscript includes the following:

MDAR Reproducibility Checklist
Movie S1

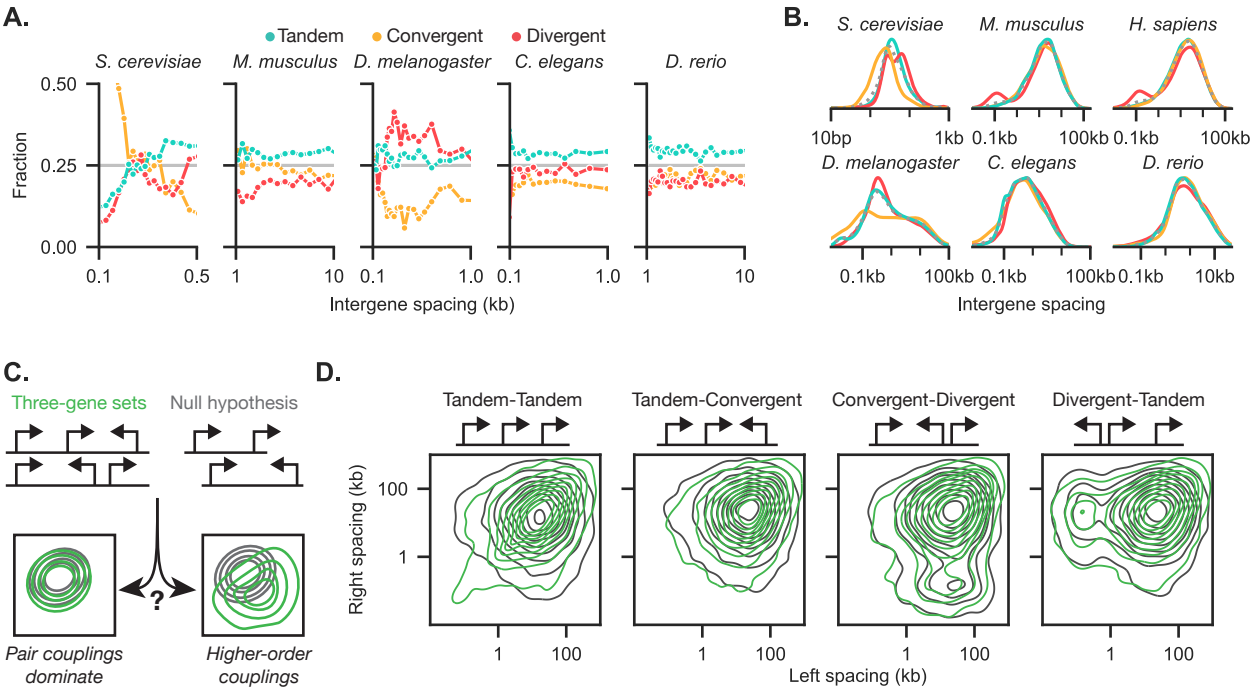

Figure S1: **Bioinformatic analysis of gene pairs and trios in eukaryotic genomes.** (**A**) Syntax distributions for gene pairs binned by intergene spacing are shown for *Saccharomyces cerevisiae*, *Mus musculus*, *Drosophila melanogaster*, *Caenorhabditis elegans*, and *Danio rerio*. (**B**) Instead of binning all gene pairs by intergene spacing as in (A) and Fig. 1B, gene pairs were separated by syntax and the intergene spacing distributions were compared to the overall distribution (gray, dashed). (**C**) Higher order couplings between trios of genes can be evaluated by computing the joint distribution of the left and right intergene spacings for all pairs of genes, compared to a null hypothesis where gene trios are synthetically created by combining gene pairs. (**D**) For the human genome, three-gene pairs can be split into four syntaxes. The distribution of intergene spacings are compared to the null hypothesis where gene pairs are randomly combined to form three-gene trios. The overlap of the distributions indicates that trios were largely explained by the pairs.

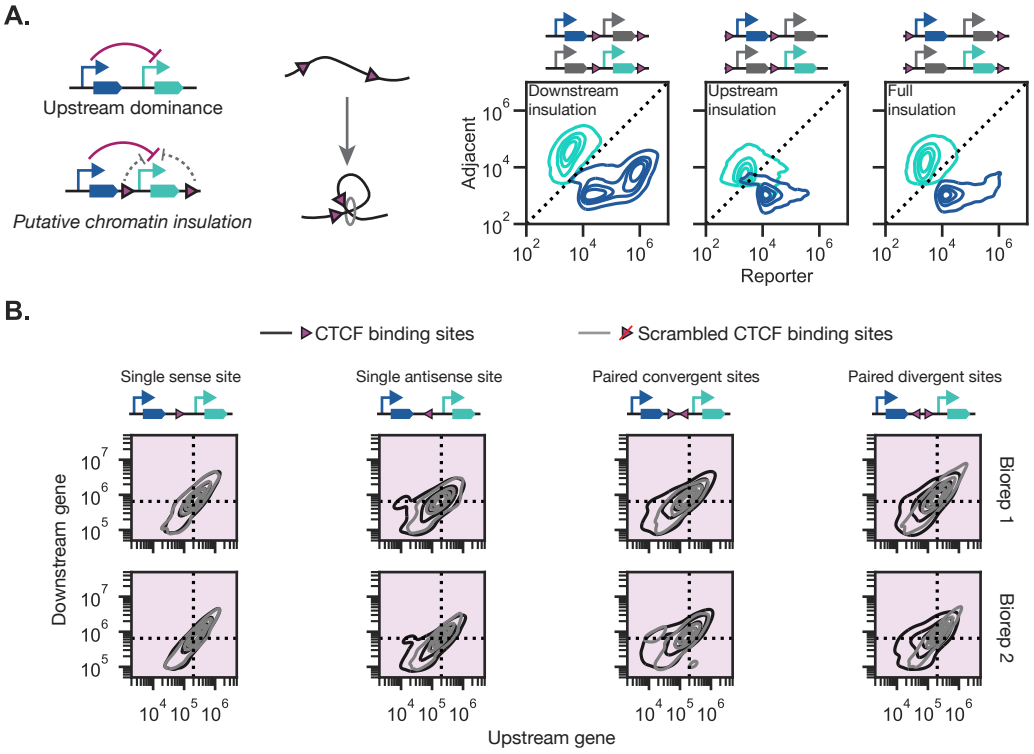

Figure S2: **Flanking CTCF sites do not alter syntax-specific expression profiles.** (**A**) Tandem-oriented CTCF binding sites were introduced flanking the upstream gene, the downstream gene, or the entire construct. Joint distributions of the two genes are shown for PiggyBac-integration into hiPSCs. Addition of these insulators does not eliminate upstream dominance. (**B**) Four variants of CTCF-based insulators were tested for insulation activity. These insulators were also "inactivated" by scrambling the CTCF binding motif. Replacing the insulator sequences with their inactivated form does not change expression profiles.

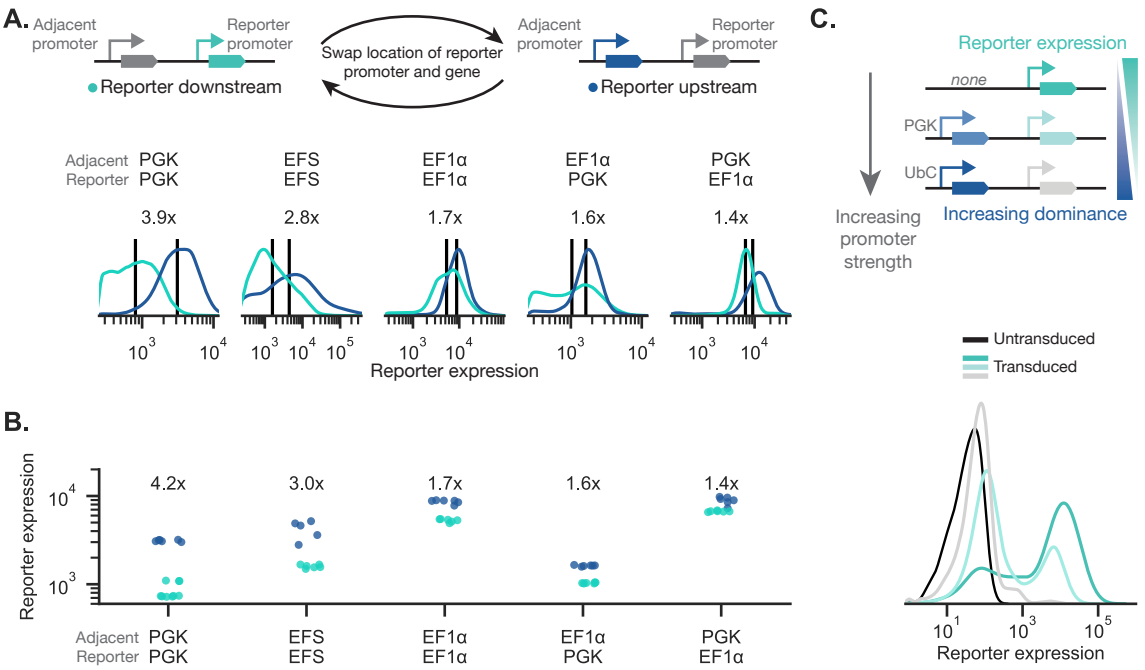

Figure S3: **Pairs of constitutive genes in tandem show upstream dominance in HEK293T cells.** (**A**) Representative distributions are shown for a reporter gene in the upstream or downstream position for different combinations of constitutive promoters with tandem syntax. Constructs were PiggyBac-integrated into HEK293T cells. All promoter pairs demonstrate upstream dominance, i.e., reporter expression is higher when it is in the upstream position. (**B**) The geometric mean of the reporter expression is plotted for five biological replicates, with the median fold change between syntaxes labeled above. (**C**) Three lentiviruses with the same constant downstream reporter but different upstream genes were transduced into HEK293T cells. Stronger upstream expression reduces downstream reporter expression more.

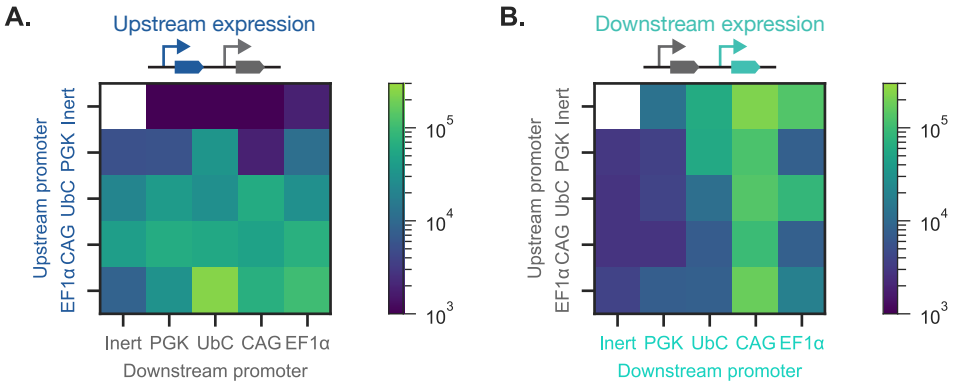

Figure S4: **Pairs of constitutive genes in tandem show upstream dominance in hiPSCs.** A panel of constitutive promoters were placed in both the upstream and downstream positions with tandem syntax and PiggyBac-integrated into hiPSCs. Heatmaps depict averages of measurements from three biological replicates. (**A**) Upstream expression for every tested promoter combination. (**B**) Downstream expression for every tested promoter combination.

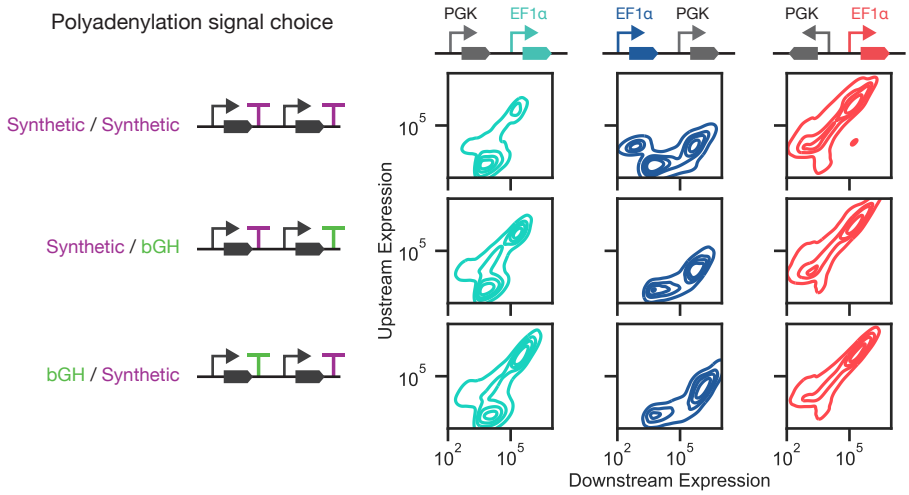

Figure S5: **Choice of polyadenylation signal (PAS) does not affect syntax-specific trends in expression.** For three different combinations of upstream and downstream PASs, representative joint distributions for PiggyBac-integrated hiPSCs are shown. The choice of PAS only minimally affects the resulting distributions for each syntax (i.e., each column shows similar joint distributions).

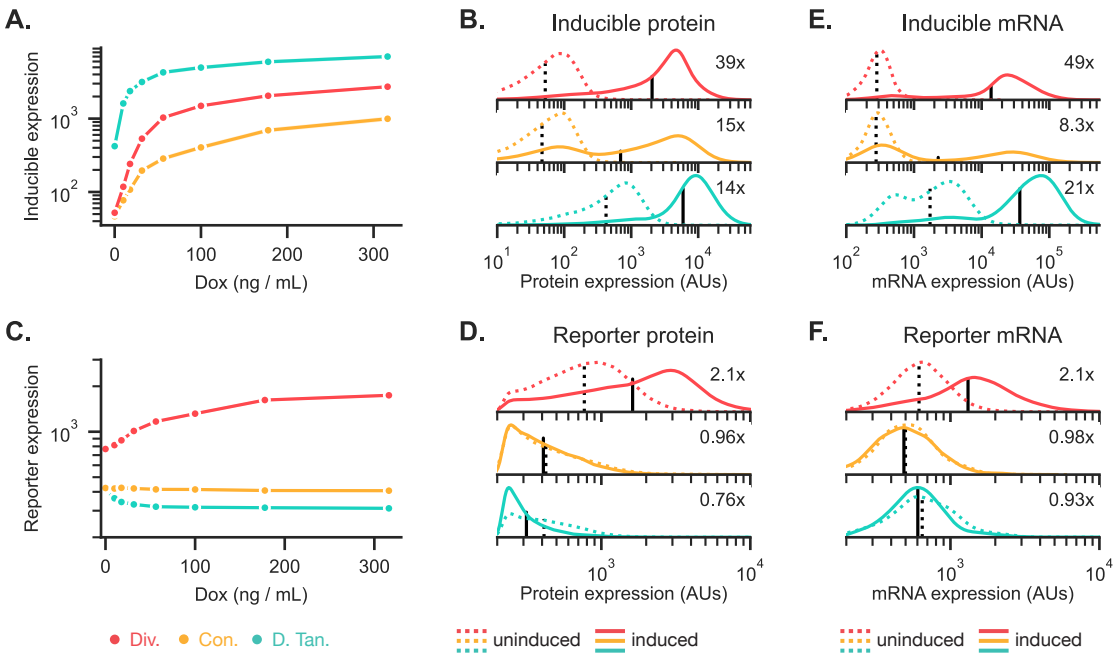

Figure S6: **Circuit syntax affects both mRNA and protein levels.** (**A**) The geometric mean of the un-normalized expression for the inducible gene is shown as a function of dox induction. The geometric mean and 95% confidence interval are calculated over three merged wells. (**B**) Representative protein distributions are shown for the inducible gene in both the uninduced (dashed) and induced (solid) cases. (**C**) The geometric mean of the un-normalized expression for the reporter gene is shown as a function of dox induction. The geometric mean and 95% confidence interval are calculated over three merged wells. (**D**) Representative protein distributions are shown for the reporter gene in both the uninduced (dashed) and induced (solid) cases. (**E–F**) Representative mRNA distributions are shown for the inducible and reporter genes in both the uninduced (dashed) and induced (solid) cases. Labeled fold-changes describe the induced condition relative to the uninduced condition.

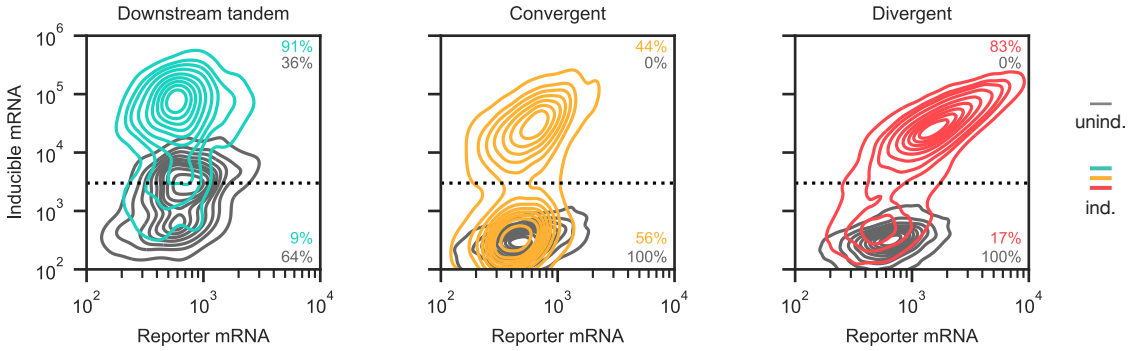

Figure S7: **Joint distributions of mRNA expression are shown for the monoclonal lines presented in Fig. 2.** mRNA profiles were measured by HCR RNA FISH for the uninduced (gray) and induced (colored) conditions. Dashed black lines depict gates used to calculate percentages of cells expressing the inducible gene.

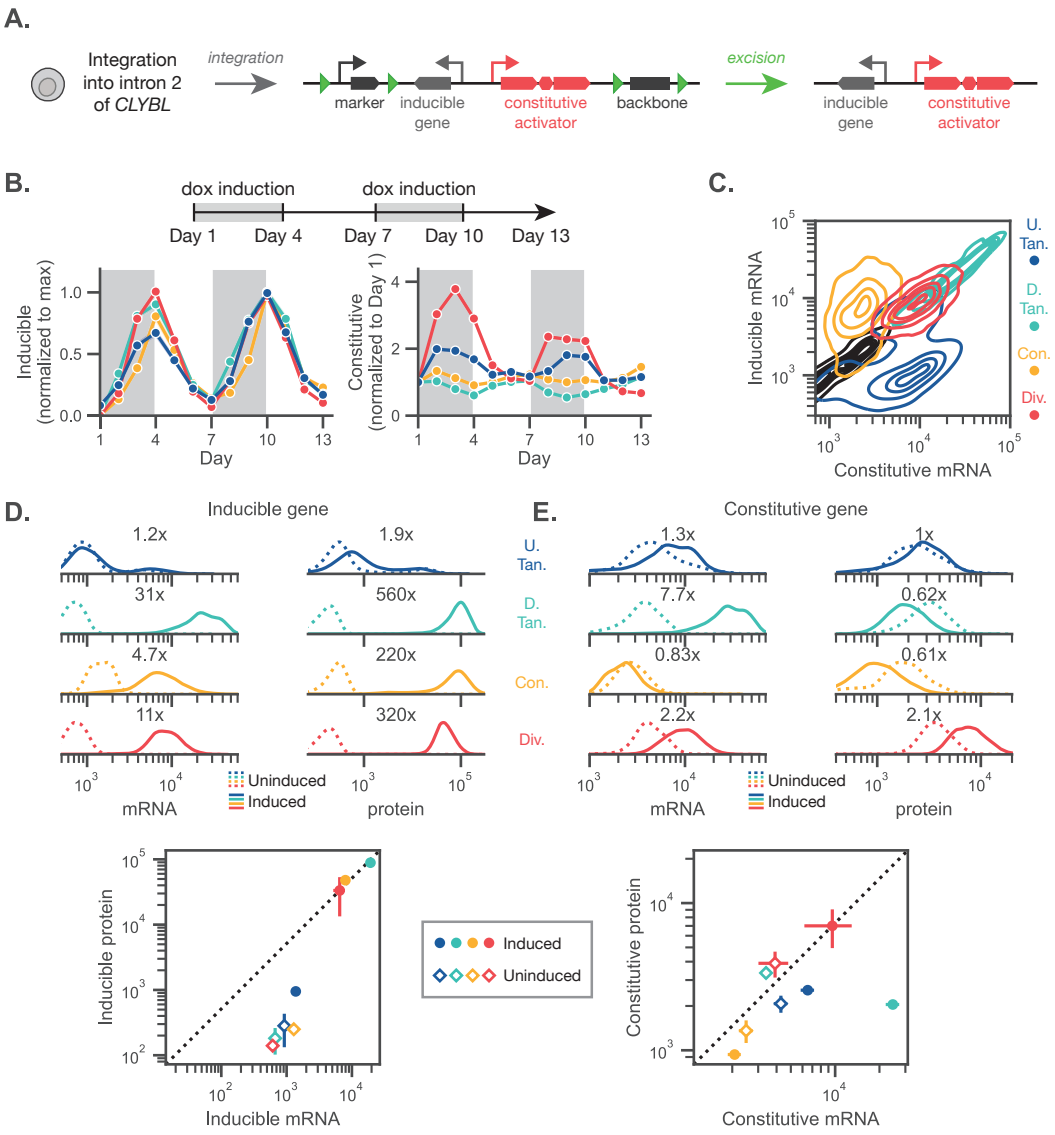
A.
Integration into intron 2 of CLYBL
integration
marker
inducible gene
constitutive activator
backbone
excision
inducible gene
constitutive activator
B.
dox induction
dox induction
Day 1
Day 4
Day 7
Day 10
Day 13
Inducible (normalized to max)
Constitutive (normalized to Day 1)
Day
C.
Inducible mRNA
Constitutive mRNA
U. Tan.
D. Tan.
Con.
Div.
D.
Inducible gene
1.2x
31x
4.7x
11x
1.9x
560x
220x
320x
mRNA
protein
Uninduced
Induced
E.
Constitutive gene
U. Tan.
D. Tan.
Con.
Div.
1.3x
7.7x
0.83x
2.2x
1x
0.62x
0.61x
2.1x
mRNA
protein
Uninduced
Induced
Inducible protein
Inducible mRNA
Induced
Uninduced
Constitutive protein
Constitutive mRNA

Figure S8: **Site-specific integration of synthetic circuits in hiPSCs elicits syntax-specific profiles of expression.** (**A**) The hiPSC lines were created by sequentially integrating a plasmid donor containing the synthetic circuit into each allele of intron 2 of *CLYBL* using STRAIGHT-IN. The plasmid backbone components and auxiliary elements of the STRAIGHT-IN platform are excised to leave the all-in-one circuit, consisting of an inducible gene expressed from the TRE promoter and a constitutive activator cassette expressed from the CAG promoter. (**B**) hiPSCs with the circuit integrated at a single allele were repeatedly induced over a period of two weeks. The inducer was added from day 1 to 4 and from day 7 to 10, as in Fig. 2E. The hiPSC lines display both upstream dominance and divergent amplification, similar to the cell lines in Fig. 2E. The geometric mean and 95% confidence interval are calculated over three merged wells. (**C**) HCR RNA FISH combined with flow cytometry was performed on the homozygously integrated hiPSC lines. For a representative biological replicate, the mRNA joint distributions are shown for each of the four syntaxes and for the parental line with no synthetic construct integrated. The downstream tandem syntax shows high correlation in expression of the two genes, potentially indicating readthrough. (**D**) Top: For a representative biological replicate, the marginal distributions of the inducible mRNA and protein levels are shown. Bottom: The geometric means of the mRNA and protein levels are plotted, where points represent mean ± standard deviation across three biological replicates. (**E**) The same plots as in **D** are shown for the constitutive gene. When cells with the downstream tandem syntax are induced, the mRNA and protein levels of the constitutive gene are uncorrelated (i.e., off the dashed diagonal line), potentially due to the presence of unproductive transcripts.

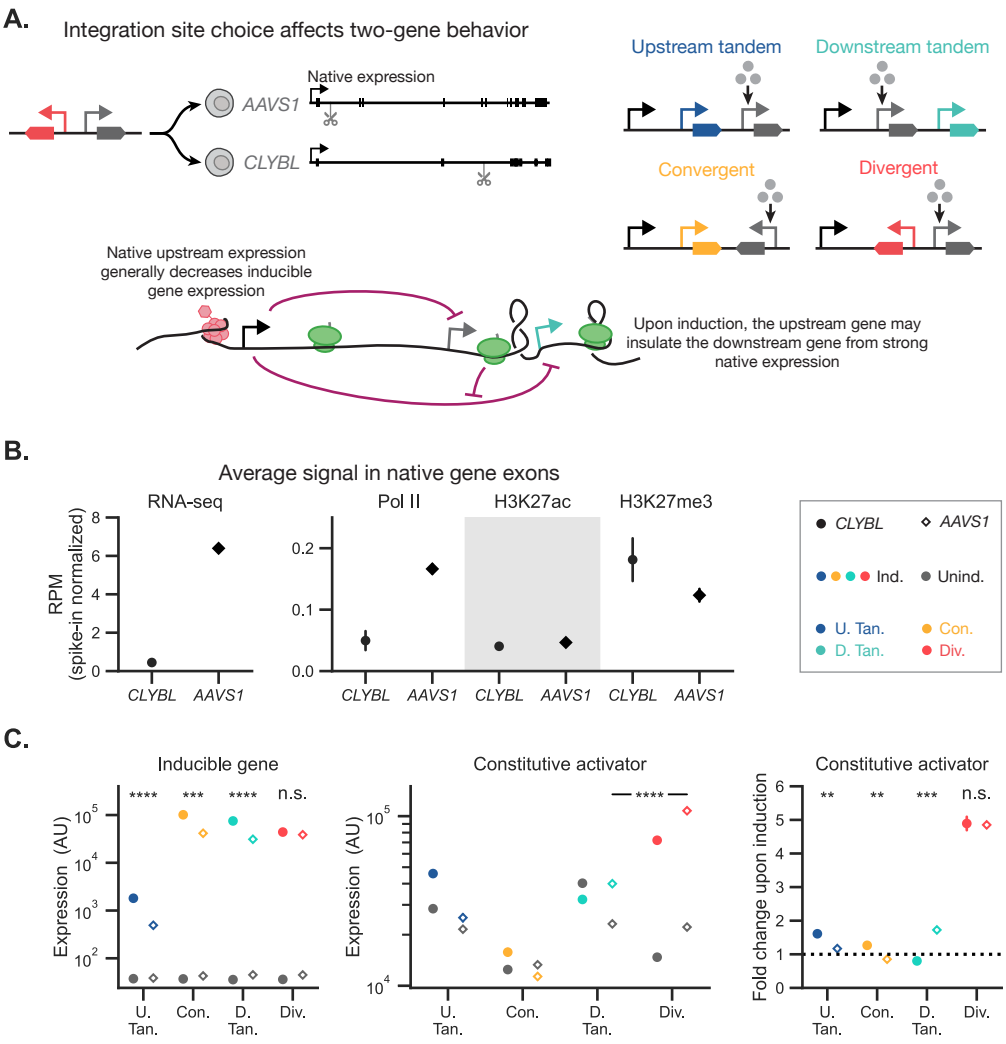

Figure S9: **Safe-harbor integration site affects expression levels of two-gene circuits.** (**A**) The two safe-harbor loci used in this work, *CLYBL* and *AAVS1*, are located within introns of endogenous genes. Therefore, activity of the native promoter of these genes may affect the expression of our integrated circuits, potentially affecting syntax-specific trends in expression. For instance, stronger expression from the native promoter may suppress expression of the upstream gene in the synthetic circuit, while the upstream gene may shield the downstream gene from these effects. (**B**) The RNA-seq read count, CUT&Tag signal from actively elongating RNA Pol II, and CUT&Tag signal for two relevant histone marks are averaged over the annotated exons of the native genes. We find that the *AAVS1* locus is more transcriptionally active and has reduced heterochromatin marks. (**C**) The expression of the inducible and constitutive genes are compared for the uninduced and induced conditions. Expression of the inducible gene is generally lower when integrated into the *AAVS1* locus. The fold-change expression of the constitutive activator upon induction is also shown. Fold changes are similar between integration loci across syntaxes, with the exception of the downstream tandem syntax. Statistics are two-sided Student's t-tests. n.s.: $p > 0.05$, * : $p < 0.1$, ** : $p < 0.01$, *** : $p < 0.001$, **** : $p < 0.0001$

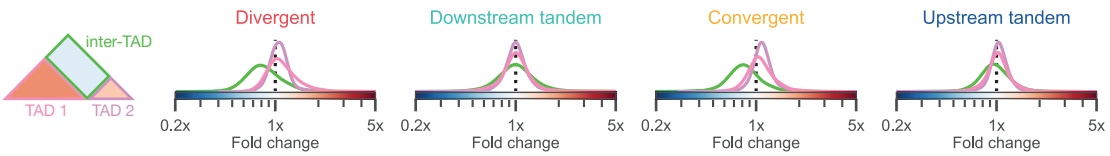

Figure S10: **Region capture Micro-C TAD interaction distributions.** For the four integrated syntaxes, the change in the inter- and intra-TAD contacts upon induction are shown. The divergent and convergent syntaxes show a strong decrease in inter-TAD interactions upon induction, whereas the tandem syntaxes do not show strong changes in TAD interactions.

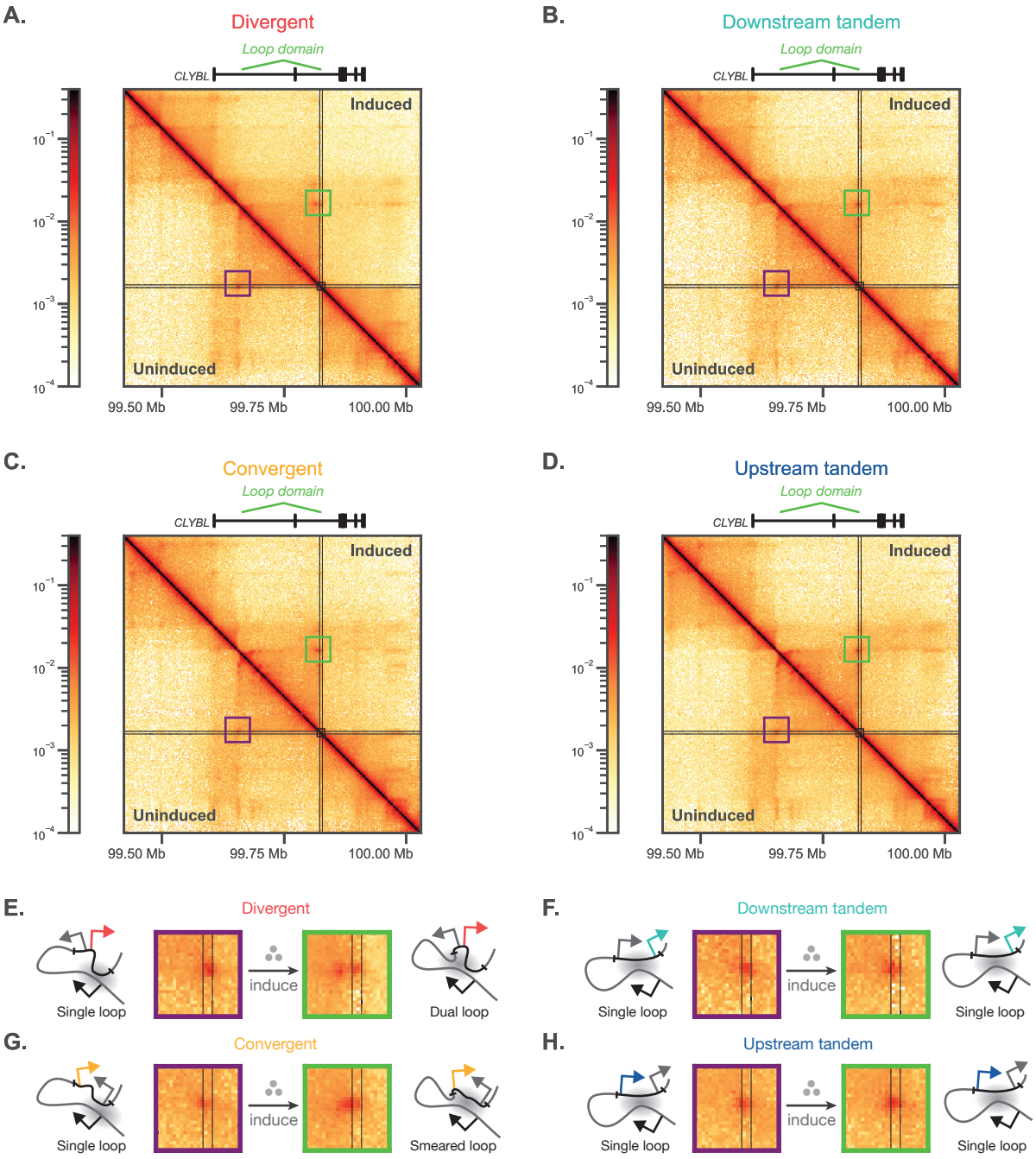

Figure S11: **Induction of transcription perturbs a 200-kb loop domain.** (**A–D**) Within the capture region, one clear loop domain (identified by a "corner dot") is visible, representing a loop contact between the first intron of *CLYBL* and the integration location. (**E–H**) Upon induction, the loop domain is perturbed in both the divergent and convergent syntaxes. This perturbation does not occur in the tandem syntaxes, highlighting that large-scale changes in 3D chromatin structure can be syntax-specific.

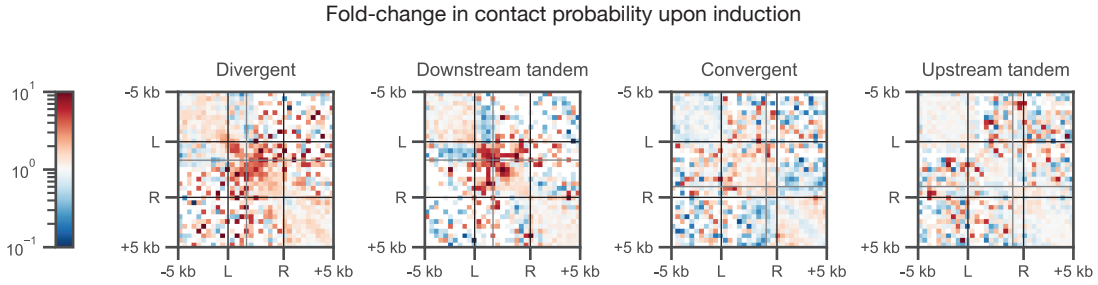

Figure S12: **Changes in contact probability upon induction show anti-diagonal stripes.** The fold change in contact probability upon induction in the local region around the integration site is shown for the four syntaxes. The divergent and downstream tandem syntaxes have the strongest changes in contact probability, visible as anti-diagonal stripes of increasing contact. Nevertheless, a diffuse increase in anti-diagonal contact probability is still visible in the convergent and upstream tandem syntaxes. These changes in contact probability are animated in Movie S1.

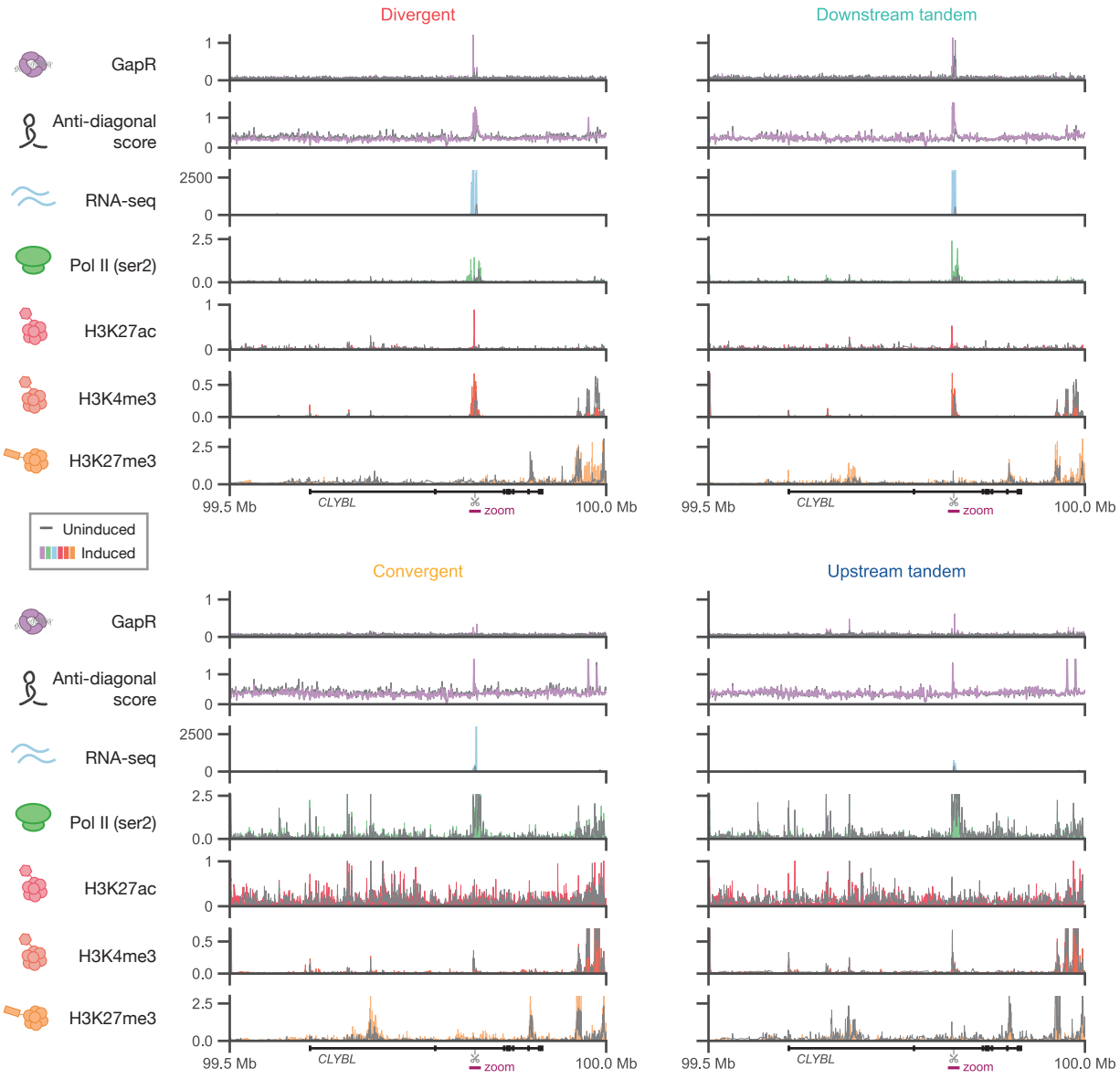

Figure S13: **1D chromatin state varies across the entire capture region.** For the GapRUN data (GapR), RCMC data (anti-diagonal score), and the four CUT&Tag datasets (Pol II ser2, H3K27ac, H3K4me3, H3K27me3), the signal across the entire capture region considered in Fig. 3 is shown for both the uninduced (gray) and induced (colored) conditions. The region encompassing the integration site and 5 kb on either side (as shown in Fig. 4) is noted in magenta with the label "zoom". Most signal appears at the integration locus.

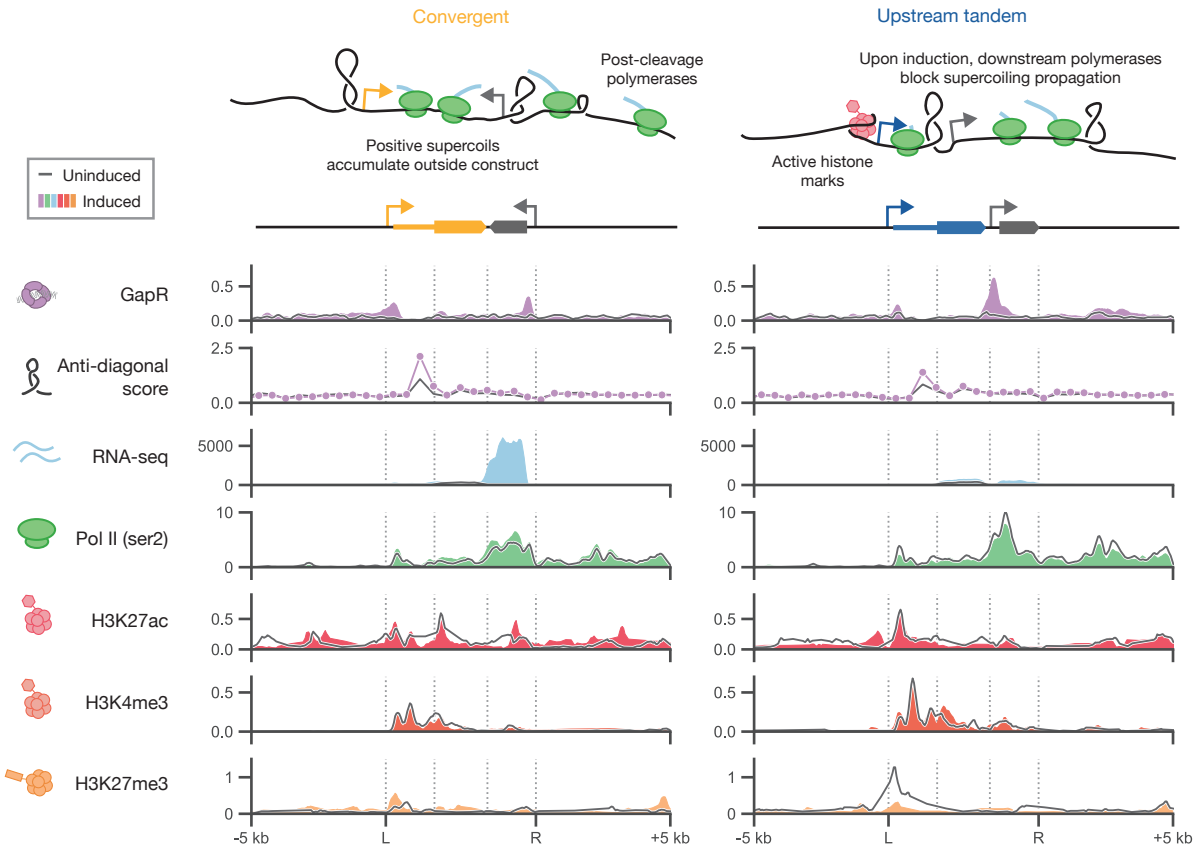

Figure S14: **Transcription induces syntax-specific chromatin structures in the convergent and upstream tandem syntaxes.** While both the convergent and upstream tandem syntaxes show induction-dependent supercoiling signals, only small changes in the histone marks and RNA Pol II occupancy are visible.

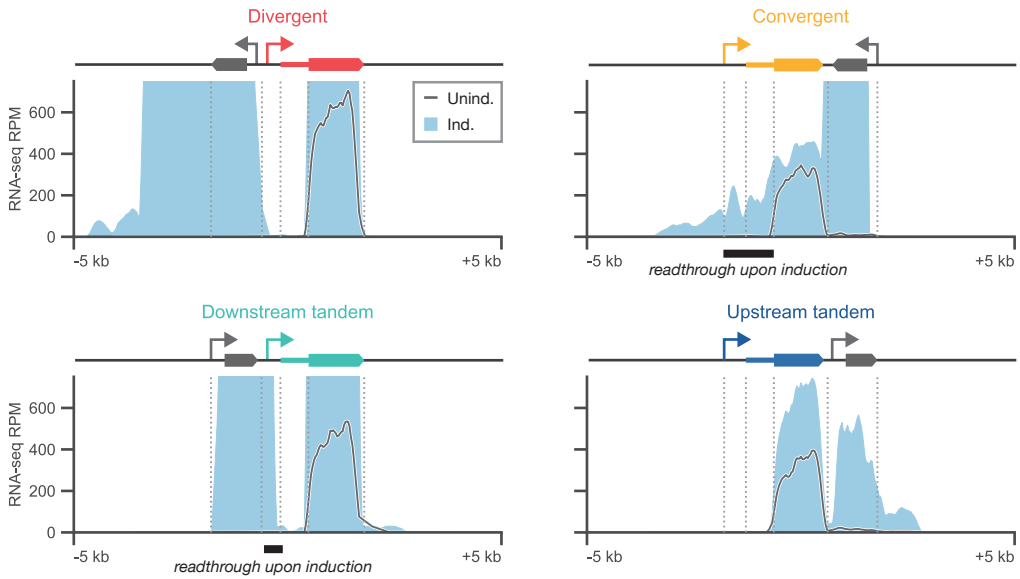

Figure S15: **RNA-seq data shows putative readthrough upon induction for downstream tandem and convergent syntaxes.** Plots show a zoom-in of the RNA-seq read counts (reads per million, RPM) for induced and uninduced conditions. Dashed lines mark the start and end of the entire synthetic construct, the middle of the intergenic region, and the start and end of the intron in the promoter of the reporter gene. Annotations (black rectangles) indicate putative readthrough transcripts from the inducible gene upon induction—namely, reads in the promoter of the constitutive reporter gene not present in the uninduced condition.

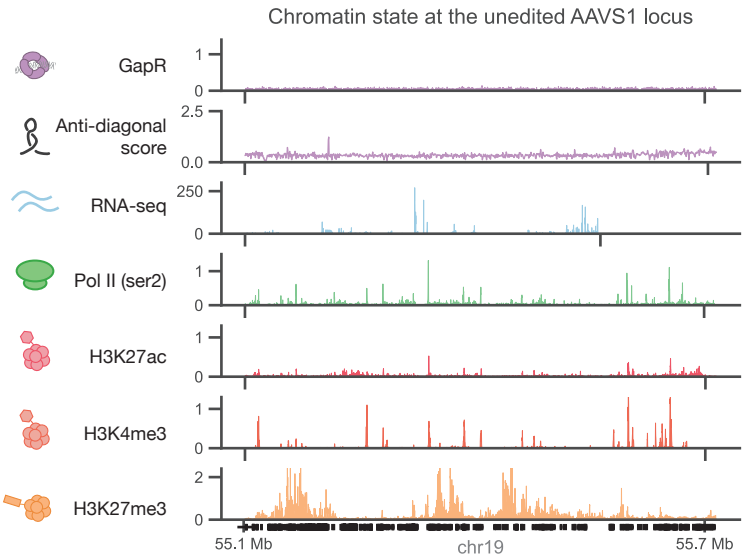

Figure S16: **Chromatin state at the unedited *AAVS1* locus demonstrates minimal supercoiling signal.** As a comparison to the *CLYBL* locus where synthetic constructs were integrated, the chromatin state at the unedited *AAVS1* locus was examined. Plots show data from one representative condition (the cell line where the divergent construct was integrated at the *CLYBL* locus). No strong supercoiling signals were detected, while some background expression and histone marks were observed throughout the relatively gene-dense *AAVS1* locus.

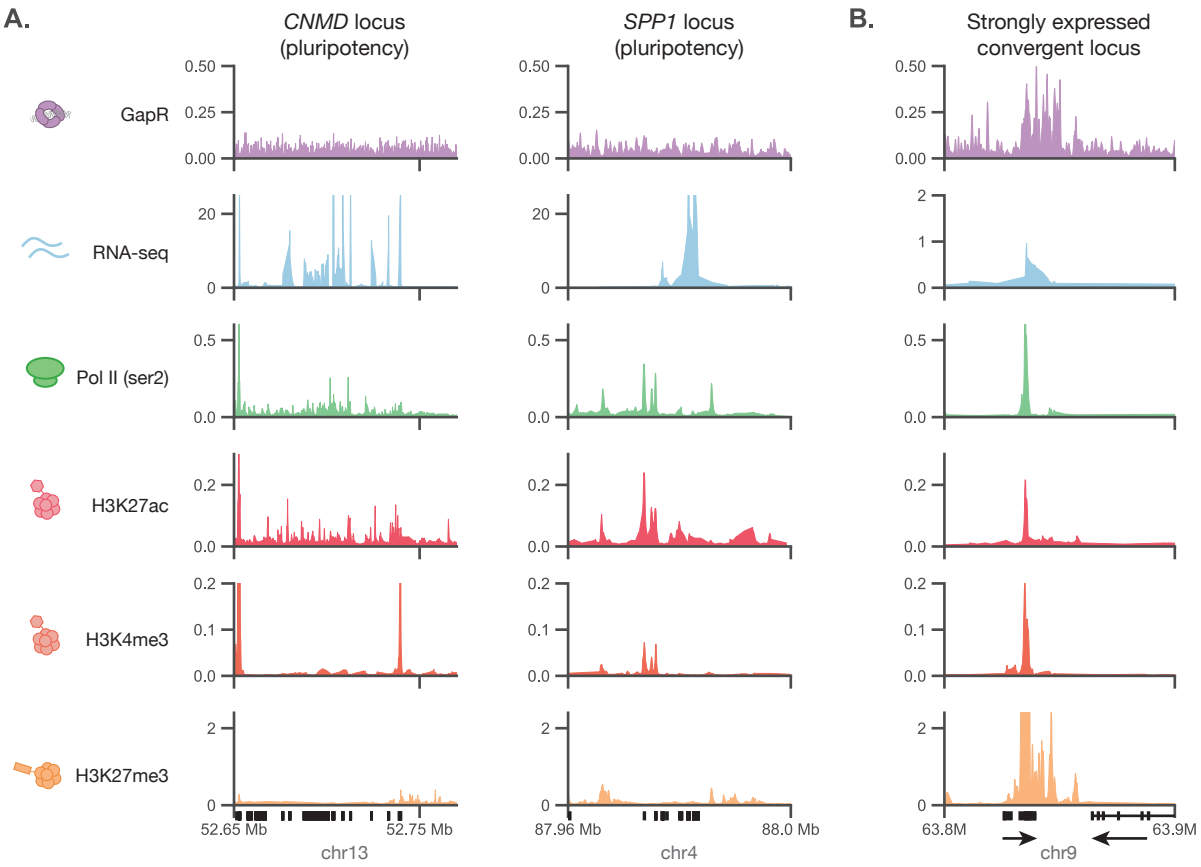

Figure S17: **Chromatin state at distal regions show signatures of transcription.** (**A**) Chromatin state measurements for two genes associated with pluripotency are shown. We observe high transcript counts at these loci. However, due to low expression of the surrounding genes, we detect no supercoiling signal above background. (**B**) Filtering for native intergenic regions with high supercoiling signal, we identify a convergent pair of transcripts on chr9, expressing a lncRNA (arrow on left) and FRG1JP (arrow on right). Strong positive supercoiling as measured by GapR is present in the intergenic region.

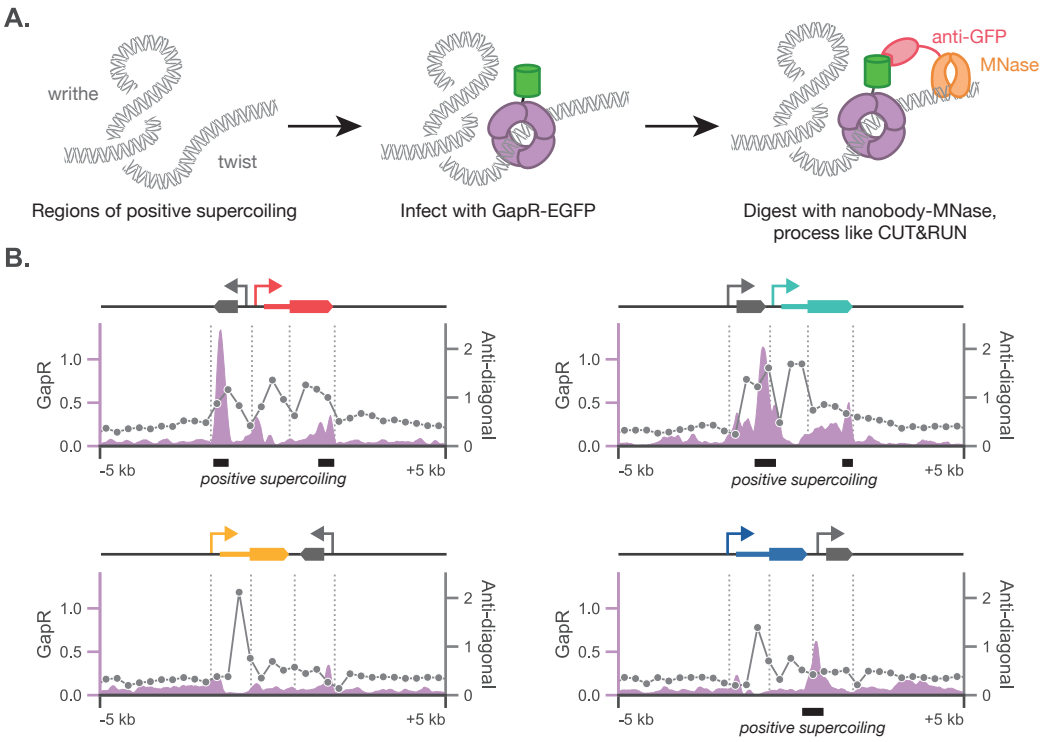

Figure S18: **GapRUN measures positive supercoiling.** (**A**) Positive supercoiling interconverts between twist, average rotation per base pair, and writhe, large-scale intertwined loops. Positive twist can be bound by a GapR, a bacterially derived protein (purple), which in GapRUN is fused to EGFP. We expressed this fusion protein in cells via lentiviral delivery. Using MNase fused to a nanobody targeting GFP, the genome can be selectively digested where the GapR protein is bound, resulting in fragments that can be processed as in CUT&RUN. (**B**) The anti-diagonal score computed from the RCMC contact probabilities (gray line), which putatively reflects formation of both positive and negative plectonemes, is compared to the GapR signal (solid purple). Regions where a high anti-diagonal score overlaps with strong GapR signal suggests the presence of positive supercoiling (black rectangles).

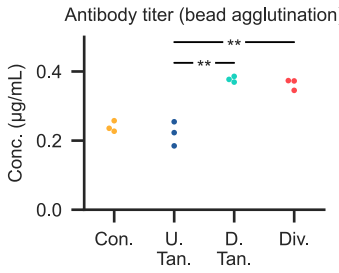

Figure S19: **Antibody titer measured by an orthogonal assay shows the same syntax-specific trends.** Antibody titer, as measured by a bead agglutination assay, for cell lines in Fig. 5A. Points depict three biological replicates (separately maintained passages of isolated lines). Statistics are two-sided Student's t-tests. n.s.: $p > 0.05$, * : $p < 0.1$, ** : $p < 0.01$

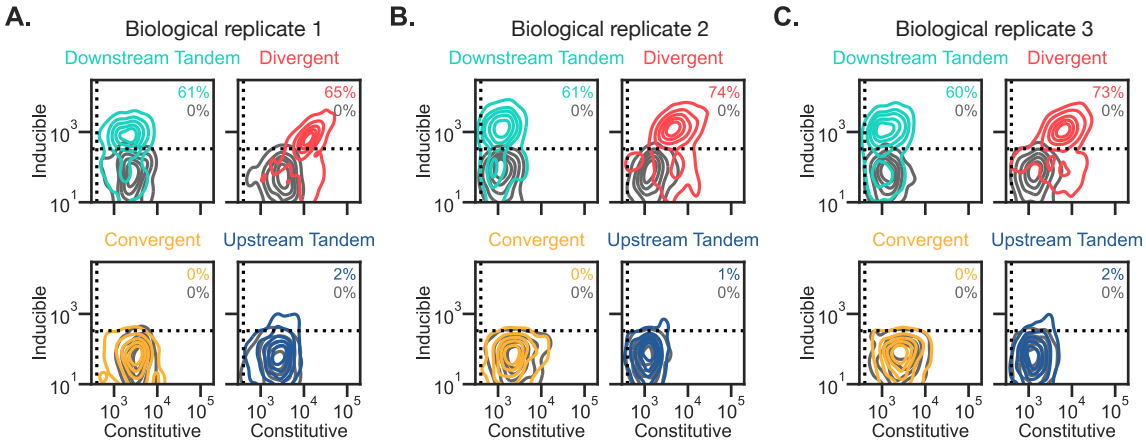

Figure S20: **Transduction of two-gene lentiviral circuits show repeatable syntax-specific trends in expression.** Joint distributions depict three additional biological replicates of the lentiviral transductions in HEK293T cells presented in Fig. 5B.

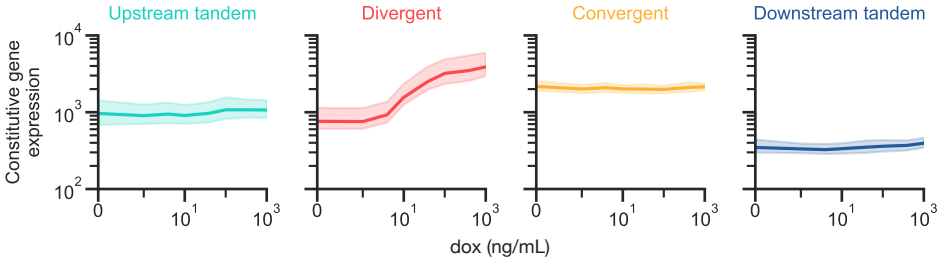

Figure S21: **For two-gene lentiviral transductions, expression of the constitutive gene increases upon induction for the divergent syntax.** Constitutive gene expression as a function of inducer (doxycycline, dox) concentration for the lentiviral transductions of HEK293T cells presented in Fig. 5B. Constitutive gene expression remains constant for the tandem and convergent syntaxes but increases with dox for the divergent syntax. Shading represents the 95% confidence interval across four biological replicates.

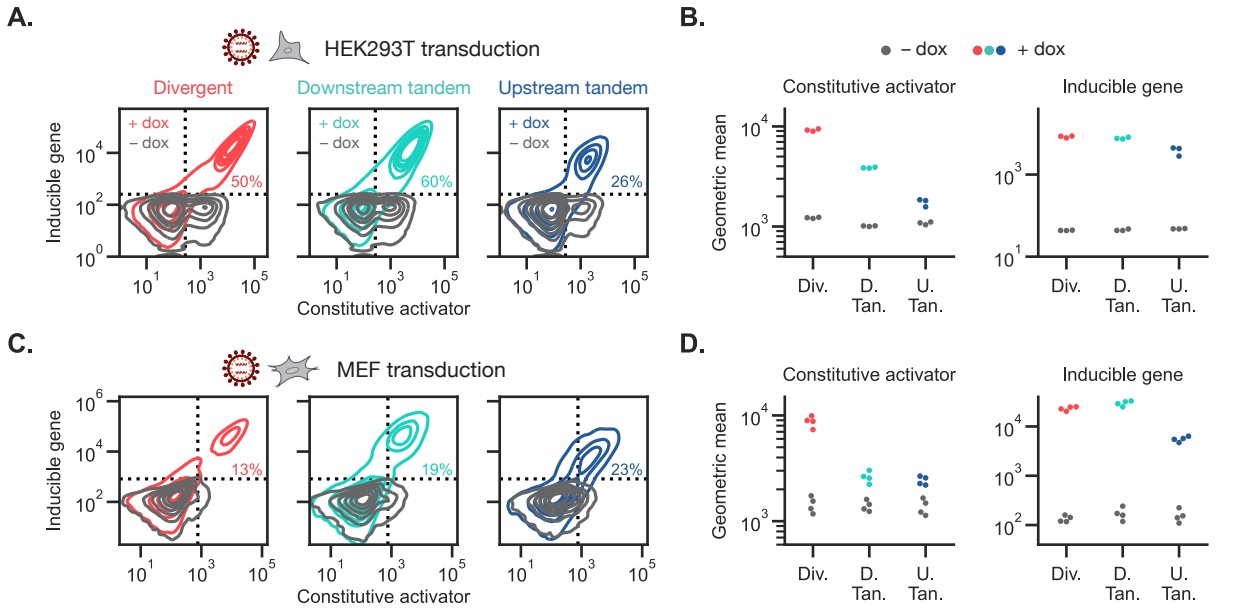

Figure S22: **All-in-one inducible circuits perform similarly across cell types.** (**A**) Joint distributions of the constitutive activator and the inducible gene for a representative biological replicate are shown for the inducible all-in-one circuits in Fig. 6A. Circuits were lentivirally transduced into HEK293T cells. (**B**) Geometric means of constitutive activator and inducible gene expression for populations from **A** gated on cells expressing the constitutive activator. The dashed vertical line in **A** shows this gate. Points depict three biological replicates. (**C**) Representative joint distributions of the constitutive activator and inducible gene are shown for the same circuits lentivirally transduced into primary mouse embryonic fibroblasts (MEFs). (**D**) Data from **C** displayed as in **B** for four biological replicates.

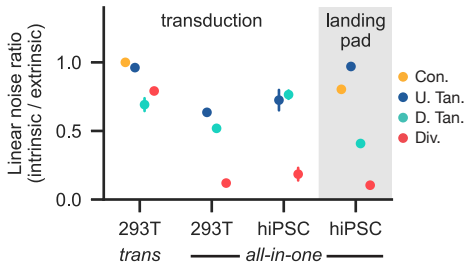

Figure S23: **The intrinsic to extrinsic noise ratio shows similar syntax-dependent trends when computed in linear space.** Computing the intrinsic and extrinsic noise on flow cytometry data in linear space gives a noise ratio that can depend on mean values (i.e., is sensitive to expression level). The divergent syntax minimizes the linear noise ratio for the all-in-one integrated circuits.

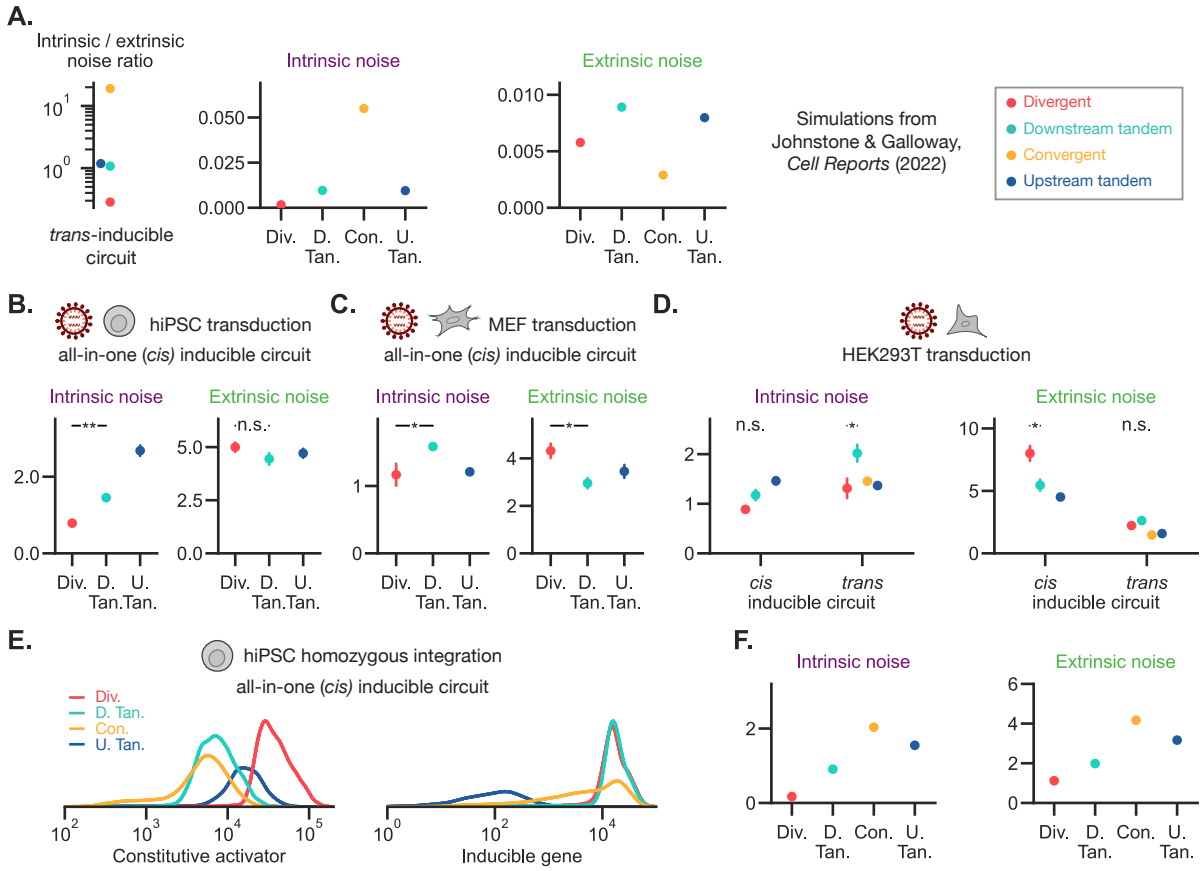

Figure S24: **Noise varies across syntaxes for inducible circuits.** (**A**) For populations comprising 2,000 simulations of the *trans*-inducible circuit modeled in Johnstone *et al.* (*7*), the intrinsic noise, extrinsic noise, and the intrinsic-to-extrinsic noise ratio is calculated for each syntax. (**B–C**) Noise analysis for lentiviral transduction of the *cis*-inducible circuit in human induced pluripotent stem cells (hiPSCs) or mouse embryonic fibroblasts (MEFs) induced with 300 ng/mL doxycycline (dox). Noise was calculated for the double-positive population. Points represent mean ± standard error for four biological replicates. (**D**) The extrinsic noise component is shown for the lentiviral transduction of either the *cis* all-in-one designs or the *trans* designs, as in Fig. 5B. Points represent mean ± standard error for four biological replicates for the *cis* design and three biological replicates for the *trans* design. (**E**) For constructs homozygously integrated at the *CLYBL* locus in hiPSCs, marginal distributions are shown for each syntax with induction (1000 ng/mL dox), as in fig. S8C. (**F**) Intrinsic and extrinsic noise is computed from the distributions in **E**. The divergent syntax has the lowest intrinsic and extrinsic noise, whereas the convergent syntax has the greatest noise. Statistics are two-sided Student's t-tests. n.s.: $p > 0.05$, * : $p < 0.05$, ** : $p < 0.01$, *** : $p < 0.001$, **** : $p < 0.0001$

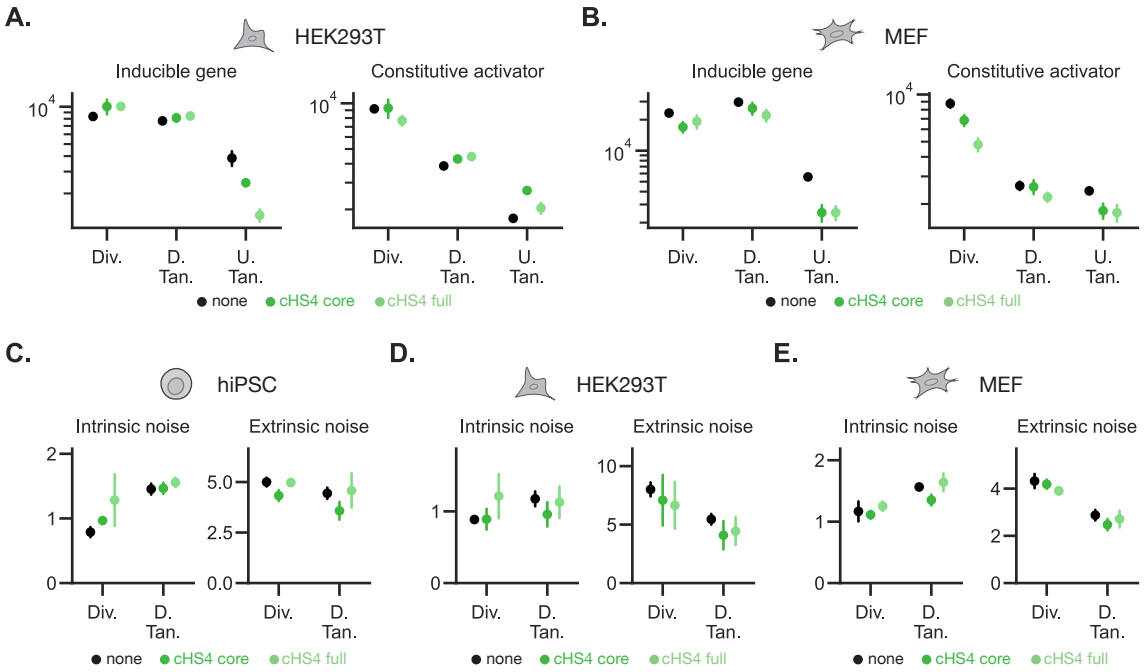

Figure S25: **The cHS4 insulator does not eliminate the effects of syntax in lentiviral delivery of an all-in-one inducible circuit.** (**A**) The circuits in Fig. 6F were lentivirally transduced into HEK293T cells. Geometric mean expression of the inducible gene and constitutive activator are shown for populations induced with 300 ng/mL doxycycline (dox). Points represent mean ± standard error for four biological replicates. (**B**) The circuits in Fig. 6F were also lentivirally transduced into mouse embryonic fibroblasts (MEFs) with five biological replicates. (**C**–**E**) Noise analysis for the circuits transduced into hiPSCs in Fig. 6F, HEK293T cells in **A**, and MEFs in **B**, respectively. All pairwise comparisons between insulators for each syntax are not significant, two-sided Student's t-tests, $p > 0.05$.

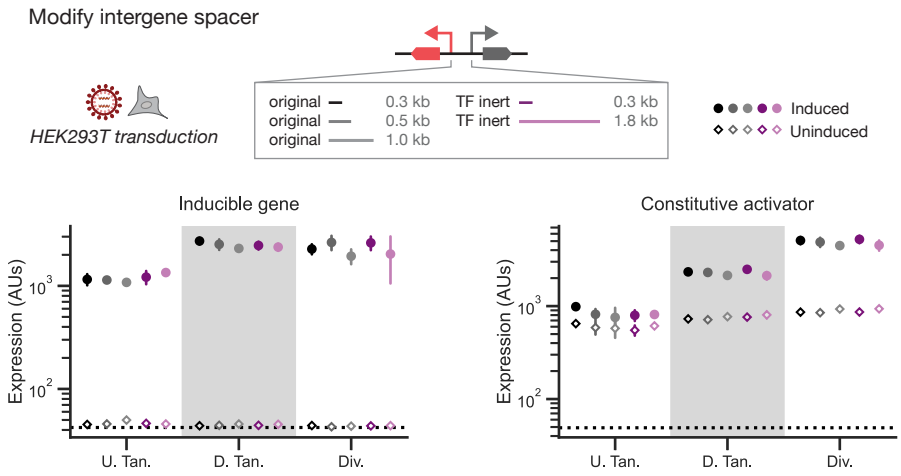

Figure S26: **Intergene spacer identity only moderately affects expression of lentivirally transduced circuits.** The circuits in Fig. 6A were modified to include the following intergenic sequences: three spacers of various length derived from a frame-shifted, reverse-complement of a coding sequence ("original"), and two spacers designed *de novo* to lack mammalian transcription factor binding sites ("TF inert"). For HEK293T cells lentivirally transduced with these circuits and treated with or without inducer, the geometric mean is shown for the inducible and constitutive genes. Points represent mean ± standard error for three biological replicates (separately produced lentivirus). Dashed black line depicts the geometric mean of untransduced cells. Spacer identity only mildly changes expression levels, and gene syntax determines the relative ordering of constitutive expression upon induction.

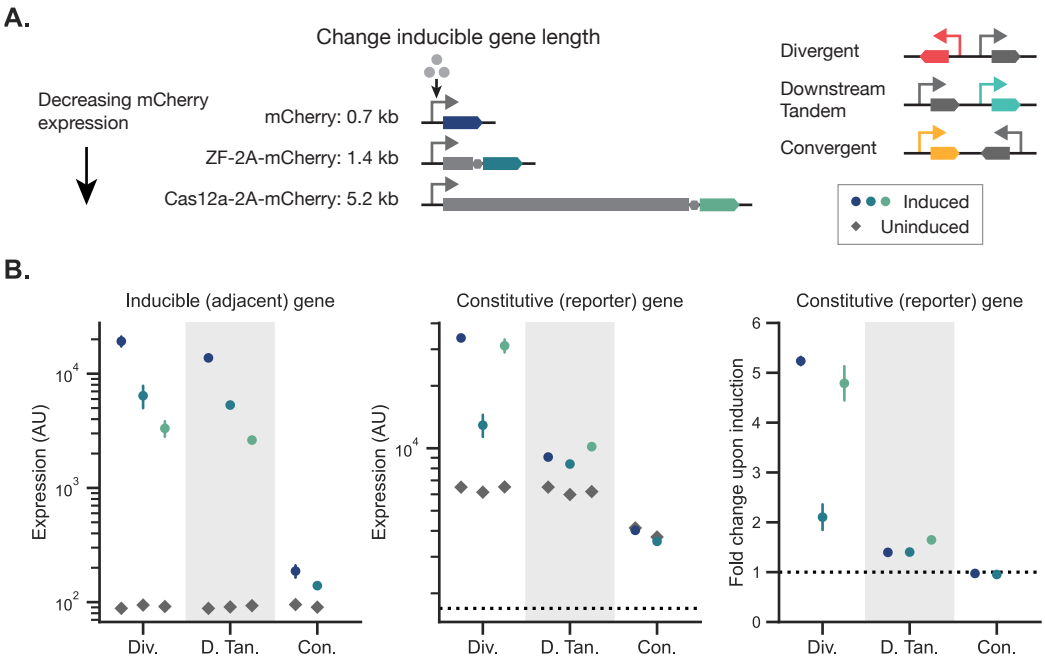

Figure S27: **Length of the inducible gene affects expression non-monotonically.** (**A**) To investigate the relationship between gene length and supercoiling-mediated biophysical coupling, we integrated two-gene circuits with three different inducible genes (all containing the fluorescent protein mCherry) into the *CLYBL* safe-harbor locus of hiPSCs. Expression level of each gene was measured for cells cultured with or without inducer. Populations were gated on cells expressing the constitutive reporter above the 95th percentile of the parental line, and conditions with only a small fraction of such cells were excluded. (**B**) The geometric mean expression of the inducible and constitutive gene is shown as a function of circuit syntax and gene length. The fold change in expression of the constitutive gene upon induction is also shown. Points represent mean ± standard error for three biological replicates (separate splits of singly integrated cell lines). Increasing the length of the inducible gene decreases expression for these constructs; however, it is possible that sequence-specific features affect these trends. For all syntaxes, the constitutive gene is least affected by the intermediate (1.4 kb) gene length, suggesting a potentially non-monotonic tradeoff between supercoiling generation, polymerase loading, and polymerase stalling.

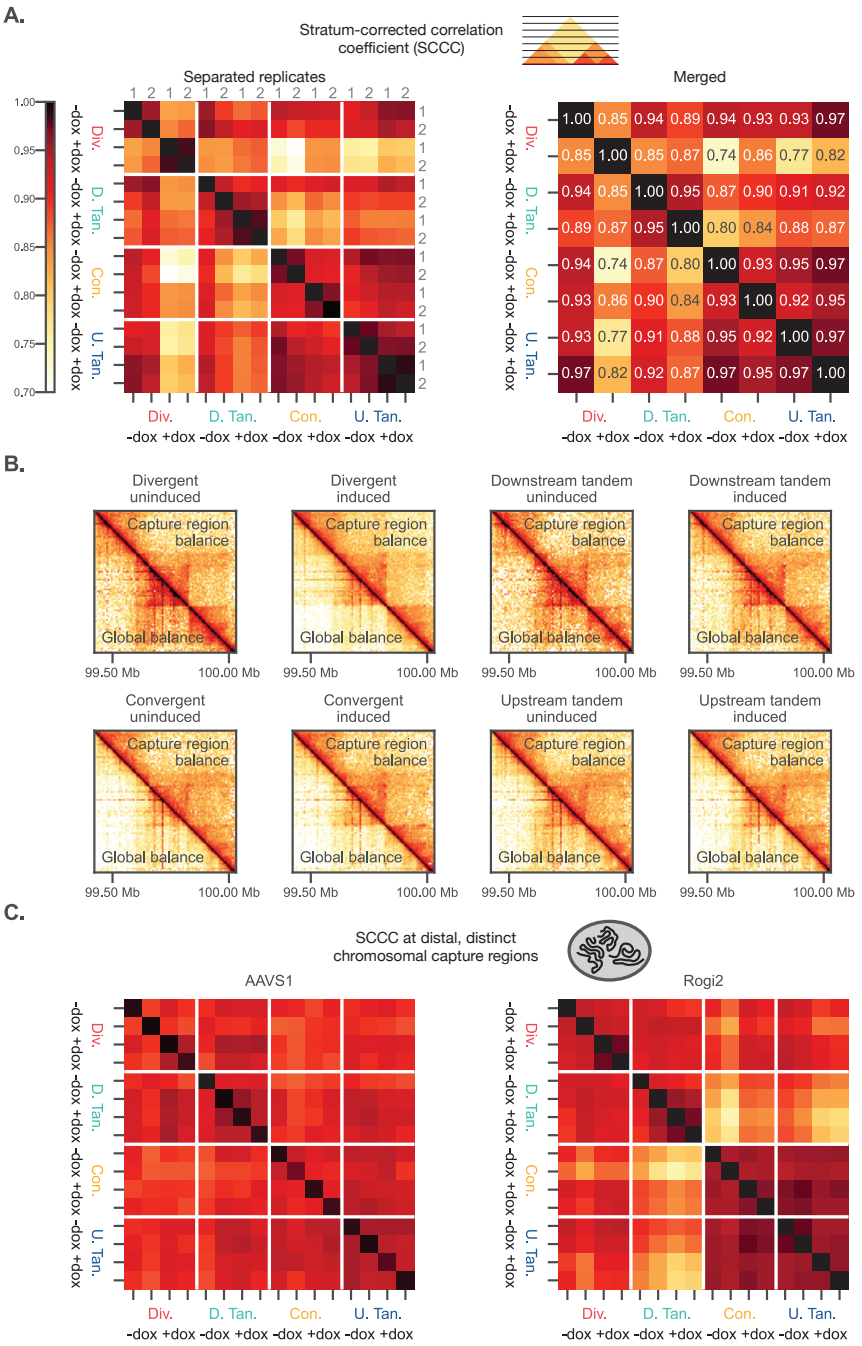
A.
Stratum-corrected correlation coefficient (SCCC)
Separated replicates
Merged
Div.
D. Tan.
Con.
U. Tan.
-dox +dox
B.
Divergent uninduced
Divergent induced
Downstream tandem uninduced
Downstream tandem induced
Convergent uninduced
Convergent induced
Upstream tandem uninduced
Upstream tandem induced
Capture region balance
Global balance
99.50 Mb
100.00 Mb
C.
SCCC at distal, distinct chromosomal capture regions
AAVS1
Rogi2

Figure S28: **Region Capture Micro-C validation.** (**A**) The stratum-corrected correlation coefficient (SCCC) measures the similarity between two interaction matrices while more heavily weighting short-distance genomic contacts. The SCCC is shown for each biological replicate and for the post-merged matrices. (**B**) The eight resulting merged RCMC genomic contacts were iteratively balanced (i.e., normalized such that every row and column sums to 1 and can be interpreted as a probability distribution), both across the entire genome and only within the capture region. Capture-region balancing provided cleaner contact probability distributions. (**C**) Two distal regions, *AAVS1* and Rogi2, were largely unaffected either by integration of the synthetic construct at *CLYBL* or by dox induction, as measured with the SCCC.

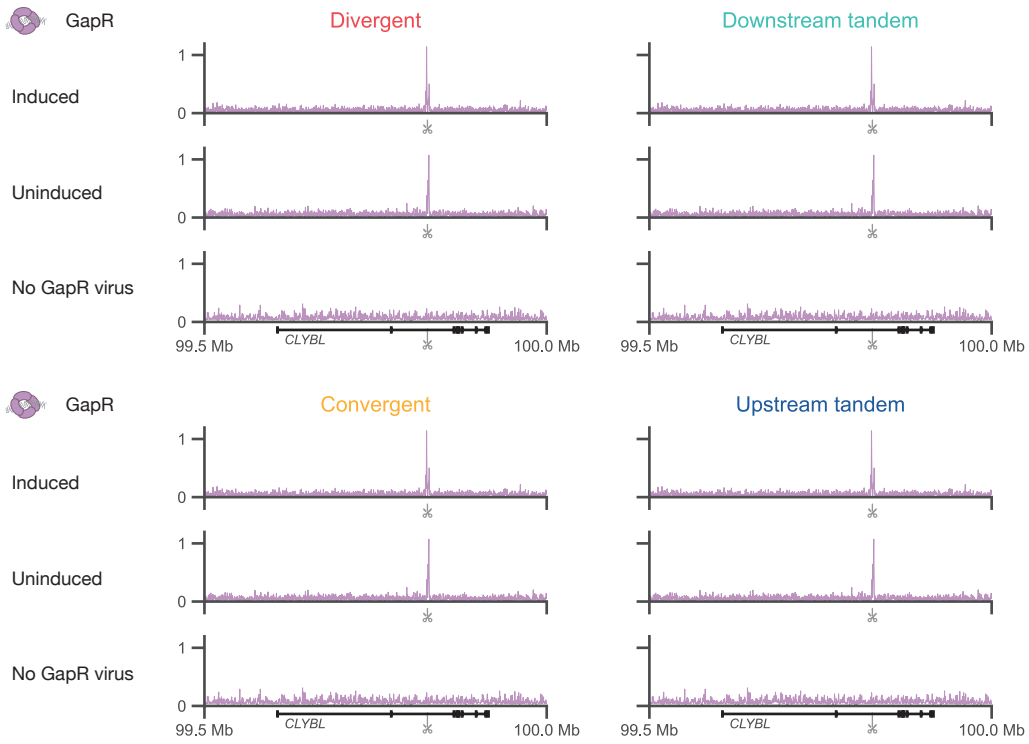

Figure S29: **The positive twist signal is detectable above background only when the GapR virus is present.** The GapR signal across the integration locus is shown for the following conditions: cells transduced with GapR virus and induced with doxycycline, cells transduced with GapR virus and uninduced, and untreated cells (no GapR virus and uninduced). The untreated control cells only show background levels of positive supercoiling signal for all syntaxes.

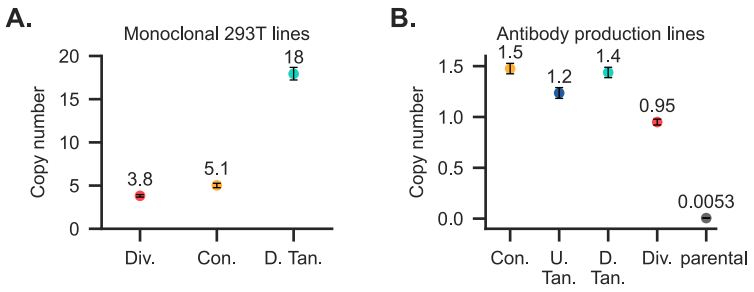

Figure S30: **Copy number was measured via ddPCR.** (**A**) Copy number of the synthetic circuit is shown for the monoclonal PiggyBac lines presented in Fig. 2. Copy number was computed from ddPCR data, normalizing measurements for the *mRuby2* gene to the reference gene *RPP30*. Error bars show the 95% confidence interval. (**B**) Copy number is shown for the antibody circuits integrated at a landing pad in HEK293T cells presented in Fig. 5A. Copy number was computed from ddPCR data, normalizing measurements for the *mRuby2* gene (located downstream of the antibody light chain) to the reference gene *RPP30*. The parental line lacking integration of the antibody components is included for comparison. Error bars show the 95% confidence interval. Due to genome instability, fractional copy numbers above 1 may occur for HEK293T cells.

Table S1: **Mapping between described genes and fluorophores.** For each figure panel, the fluorophores used to measure expression of each gene in the synthetic circuits are listed.

Figure	Reporter / Constitutive	Adjacent / Inducible
Fig. 1C; figs. S2 and S5	TagBFP	mNeonGreen
Figs. 2B, 2C, 2E, 5B, 5C, 5D, and 6E; figs. S6A, S6B, S6C, S6D, S20, S21, and S23	mRuby2	TagBFP
Fig. 2D; figs. S6E, S6F, and S7	Alexa Fluor™ 514	Alexa Fluor™ 647
Fig. 6; figs. S3A, S3B, S22, S23, S24B, S24C, S24D, S25, and S26	mGreenLantern (mGL)	mRuby2
Fig. 6E; figs. S8B, S8D, S8E, S9C, S23, S24E, and S24F	mTagBFP2	mScarlet
figs. S8C, S8D, and S8E	Alexa Fluor™ 647	Alexa Fluor™ 514
fig. S27	mGL	mCherry
Figure	Upstream	Downstream
fig. S3C	none	mRuby2
fig. S4	TagBFP	mNeonGreen

Table S2: **Constructs, cell type, and integration method.** Information about cell lines is listed for each figure panel. Refer to tables S3–S5 for a description of the contents of the plasmids.

Figure	Cell type	Plasmids	Integration	Selection information
Fig. 1C	iPS11	1 (DT), 2 (UT)	PiggyBac	Transient puromycin
Fig. 2; figs. S6, S7, and S30A	HEK293T	3 + {4 (DT), 5 (C), 6 (D)}	PiggyBac	Puromycin, monoclonal sort
Figs. 3, 4, and 6E; figs. S8C, S8D, S8E, S9, S10, S11, S12, S13, S14, S15, S16, S17, S18, S23, S24E, S24F, S28, and S29	STRAIGHT-IN hiPSC	{7, 8 (DT); 9, 10 (D); 11, 12 (UT); 13, 14 (C)} ± 15	Bxb1 landing pad	STRAIGHT-IN
Fig. 5A; fig. S19	Rogi2 landing pad HEK293T	16 (UT), 17 (DT), 18 (C), 19 (D)	Bxb1 landing pad	Puromycin
Figs. 5B, 5C, 5D, and 6E; figs. S20, S21, and S23	HEK293T	20/21 + {22 (UT), 23 (DT), 24 (C), 25 (D)}	Lentivirus	Polyclonal sort
Figs. 6B, 6C, 6D, 6E, and 6F; figs. S23, S24B and S25C	iPS11	26 (DT), 27 (Div), 28 (UT)	Lentivirus	None
Fig. 6E; figs. S22A, S22B, S23, S24D, S25A, S25D, and S26	HEK293T	26 (DT), 27 (Div), 28 (UT)	Lentivirus	None
Fig. 6F; fig. S25C – cHS4 core	iPS11	29 (D), 30 (DT), 31 (UT)	Lentivirus	None
Fig. 6F; fig. S25C – cHS4 full	iPS11	32 (D), 33 (DT), 34 (UT)	Lentivirus	None
figs. S3A and S3B, PGK-PGK	HEK293T	35 (UT), 36 (DT)	PiggyBac	Puromycin, polyclonal sort
figs. S3A and S3B, EFS-EFS	HEK293T	37 (UT), 38 (DT)	PiggyBac	Puromycin, polyclonal sort
figs. S3A and S3B – EF1α-EF1α	HEK293T	39 (UT), 40 (DT)	PiggyBac	Puromycin, polyclonal sort
figs. S3A and S3B – EF1α-PGK	HEK293T	41 (UT), 42 (DT)	PiggyBac	Puromycin, polyclonal sort
figs. S3A and S3B – PGK-EF1α	HEK293T	43 (UT), 44 (DT)	PiggyBac	Puromycin, polyclonal sort
fig. S3C	HEK293T	45, 46, 47	Lentivirus	None
fig. S8B	STRAIGHT-IN hiPSC	8 (DT), 10 (D), 12 (UT), 14 (C)	Bxb1 landing pad	STRAIGHT-IN
figs. S22C, S22D, S24C, S25B, and S25E	MEF	26 (DT), 27 (Div), 28 (UT)	Lentivirus	None
fig. S25A and S25D – cHS4 core	HEK293T	29 (D), 30 (DT), 31 (UT)	Lentivirus	None
fig. S25A and S25D – cHS4 full	HEK293T	32 (D), 33 (DT), 34 (UT)	Lentivirus	None
fig. S25B and S25E – cHS4 core	MEF	29 (D), 30 (DT), 31 (UT)	Lentivirus	None
fig. S25B and S25E – cHS4 full	MEF	32 (D), 33 (DT), 34 (UT)	Lentivirus	None
fig. S26 – original 0.5 kb	HEK293T	48 (DT), 49 (D), 50 (UT)	Lentivirus	None
fig. S26 – original 1.0 kb	HEK293T	51 (DT), 52 (D), 53 (UT)	Lentivirus	None
fig. S26 – TF inert 0.3 kb	HEK293T	54 (DT), 55 (D), 56 (UT)	Lentivirus	None
fig. S26 – TF inert 1.8 kb	HEK293T	57 (DT), 58 (D), 59 (UT)	Lentivirus	None
fig. S27 – 0.7 kb	STRAIGHT-IN hiPSC	60 (DT), 61 (D), 62 (UT), 63 (C)	Bxb1 landing pad	STRAIGHT-IN
fig. S27 – 1.4 kb	STRAIGHT-IN hiPSC	64 (DT), 65 (D), 66 (UT), 67 (C)	Bxb1 landing pad	STRAIGHT-IN
fig. S27 – 5.2 kb	STRAIGHT-IN hiPSC	68 (DT), 69 (D), 70 (UT), 71 (C)	Bxb1 landing pad	STRAIGHT-IN
fig. S2A – downstream insulation	iPS11	72 (UT), 73 (DT)	PiggyBac	Transient puromycin
fig. S2A – upstream insulation	iPS11	74 (UT), 75 (DT)	PiggyBac	Transient puromycin
fig. S2A – full insulation	iPS11	76 (UT), 77 (DT)	PiggyBac	Transient puromycin
fig. S2B	iPS11	78–85	PiggyBac	Transient puromycin
fig. S4	iPS11	86–108	PiggyBac	Transient puromycin
fig. S5	iPS11	109, 110, 111 (D); 90, 112, 113 (UT); 1, 114, 115 (DT)	PiggyBac	Transient puromycin

Table S3: **Plasmids used in main-text figures.** Text in parentheses indicates a sequence placed in the antisense direction.

Ref	Identifier	Syntax	Construct	Addgene #
1	aRJ134	D Tan	PGK-mNeonGreen-syn_pA EF1α-TagBFP-syn_pA	252538
2	aRJ135	U Tan	EF1α-TagBFP-syn_pA PGK-mNeonGreen-syn_pA	252539
3	pKG1701	Tan	CMV-rtTA-βglobin_pA CMV-PuroR-bGH	252540
4	pKG1416	D Tan	TRE-TagBFP-bGH EF1α-mRuby2-SV40	252541
5	pKG1417	Con	TRE-TagBFP-bGH (EF1α-mRuby2-SV40)	252542
6	pKG1418	Div	(TRE-TagBFP-bGH) EF1α-mRuby2-SV40	252543
7	pKG3039	D Tan	GA allele, TRE3G-mScarlet-WPRE CAG-rtTA-T2A-mTagBFP2-bGH	229792
8	pKG4156	D Tan	GT allele, TRE3G-mScarlet-WPRE CAG-rtTA-T2A-mTagBFP2-bGH	229794
9	pKG3037	Div	GA allele, (TRE3G-mScarlet-WPRE) CAG-rtTA-T2A-mTagBFP2-bGH	229791
10	pKG4154	Div	GT allele, (TRE3G-mScarlet-WPRE) CAG-rtTA-T2A-mTagBFP2-bGH	252544
11	pKG3040	U Tan	GA allele, CAG-rtTA-T2A-mTagBFP2-bGH TRE3G-mScarlet-WPRE	229793
12	pKG4157	U Tan	GT allele, CAG-rtTA-T2A-mTagBFP2-bGH TRE3G-mScarlet-WPRE	252545
13	pKG3038	Con	GA allele, CAG-rtTA-T2A-mTagBFP2-bGH (TRE3G-mScarlet-WPRE)	229790
14	pKG4155	Con	GT allele, CAG-rtTA-T2A-mTagBFP2-bGH (TRE3G-mScarlet-WPRE)	252546
15	pKG4062	n/a	LentiX1, EF1α-GapR-3xFLAG-NLS-EGFP-bGH	252547
16	pKG3851	U Tan	CMV-mAb17HC-bGH CMV-mAb17LC-P2A-mRuby2-bGH	
17	pKG3852	D Tan	CMV-mAb17LC-P2A-mRuby2-bGH CMV-mAb17HC	
18	pKG3853	Con	CMV-mAb17HC-bGH (CMV-mAb17LC-P2A-mRuby2-bGH)	
19	pKG3854	Div	(CMV-mAb17HC-bGH) CMV-mAb17LC-P2A-mRuby2-bGH	
20	pKG2752	n/a	LentiX1, EFS-rtTA-P2A-mGL-WPRE	252548
21	pKG1522	n/a	LentiX1, CMV-rtTA-βglobin_pA	252549
22	pKG3426	U Tan	LentiX1, EF1α-mRuby2-bGH TRE-TagBFP-bGH	252550
23	pKG3425	D Tan	LentiX1, TRE-TagBFP-bGH EF1α-mRuby2-bGH	252551
24	pKG3427	Con	LentiX1, EF1α-mRuby2-bGH (TRE-TagBFP-bGH)	252552
25	pKG3428	Div	LentiX1, (TRE-TagBFP-bGH) EF1α-mRuby2-bGH	252553
26	pKG1484	D Tan	LentiX1, TRE-mRuby2-bGH original_0.3kb EFS-rtTA-P2A-mGL-WPRE	252554
27	pKG1487	Div	LentiX1, (TRE-mRuby2-bGH) original_0.3kb EFS-rtTA-P2A-mGL-WPRE	252555
28	pKG3549	U Tan	LentiX1, EFS-rtTA-P2A-mGL-WPRE original_0.3kb TRE-mRuby2-bGH	252556
29	pKG3572	Div	LentiX1, (TRE-mRuby2-bGH) cHS4_core EFS-rtTA-P2A-mGL-WPRE	252557
30	pKG3571	D Tan	LentiX1, TRE-mRuby2-bGH cHS4_core EFS-rtTA-P2A-mGL-WPRE	252558
31	pKG3574	U Tan	LentiX1, EFS-rtTA-P2A-mGL-WPRE cHS4_core TRE-mRuby2-bGH	252559
32	pKG3576	Div	LentiX1, (TRE-mRuby2-bGH) cHS4_full EFS-rtTA-P2A-mGL-WPRE	252560
33	pKG3575	D Tan	LentiX1, TRE-mRuby2-bGH cHS4_full EFS-rtTA-P2A-mGL-WPRE	252561
34	pKG3578	U Tan	LentiX1, EFS-rtTA-P2A-mGL-WPRE cHS4_full TRE-mRuby2-bGH	252562

Table S4: **Plasmids used in supplemental figures.** Text in parentheses indicates a sequence placed in the antisense direction.

Ref	Identifier	Syntax	Construct
35	pKG2651	U Tan	PGK-Puro-T2A-mGL-SV40 PGK-mRuby2-bGH
36	pKG2648	D Tan	PGK-mRuby2-bGH PGK-Puro-T2A-mGL-SV40
37	pKG2650	U Tan	EFS-Puro-T2A-mGL-SV40 EFS-mRuby2-bGH
38	pKG2647	D Tan	EFS-mRuby2-bGH EFS-Puro-T2A-mGL-SV40
39	pKG2780	U Tan	EF1α-Puro-T2A-mGL-SV40 EF1α-mRuby2-bGH
40	pKG2649	D Tan	EF1α-mRuby2-bGH EF1α-Puro-T2A-mGL-SV40
41	pKG2921	U Tan	PGK-Puro-T2A-mGL-SV40 EF1α-mRuby2-bGH
42	pKG2993	D Tan	EF1α-mRuby2-bGH PGK-Puro-T2A-mGL-SV40
43	pKG2920	U Tan	EF1α-Puro-T2A-mGL-SV40 PGK-mRuby2-bGH
44	pKG2919	D Tan	PGK-mRuby2-bGH EF1α-Puro-T2A-mGL-SV40
45	pKG1331	n/a	LentiX1, EF1α-mRuby2-WPRE
46	pKG1325	D Tan	LentiX1, PGK-SNAPtag-bGH EF1α-mRuby2-WPRE
47	pKG1327	D Tan	LentiX1, UbC-SNAPtag-bGH EF1α-mRuby2-WPRE
48	pKG4819	D Tan	LentiX1, TRE-mRuby2-bGH original_0.5kb EFS-rtTA-P2A-mGL-WPRE
49	pKG4820	Div	LentiX1, (TRE-mRuby2-bGH) original_0.5kb EFS-rtTA-P2A-mGL-WPRE
50	pKG4821	U Tan	LentiX1, EFS-rtTA-P2A-mGL-WPRE original_0.5kb TRE-mRuby2-bGH
51	pKG4822	D Tan	LentiX1, TRE-mRuby2-bGH original_1.0kb EFS-rtTA-P2A-mGL-WPRE
52	pKG4823	Div	LentiX1, (TRE-mRuby2-bGH) original_1.0kb EFS-rtTA-P2A-mGL-WPRE
53	pKG4824	U Tan	LentiX1, EFS-rtTA-P2A-mGL-WPRE original_1.0kb TRE-mRuby2-bGH
54	pKG4813	D Tan	LentiX1, TRE-mRuby2-bGH TF.inert_0.3kb EFS-rtTA-P2A-mGL-WPRE
55	pKG4814	Div	LentiX1, (TRE-mRuby2-bGH) TF.inert_0.3kb EFS-rtTA-P2A-mGL-WPRE
56	pKG4815	U Tan	LentiX1, EFS-rtTA-P2A-mGL-WPRE TF.inert_0.3kb TRE-mRuby2-bGH
57	pKG4816	D Tan	LentiX1, TRE-mRuby2-bGH TF.inert_1.8kb EFS-rtTA-P2A-mGL-WPRE
58	pKG4817	Div	LentiX1, (TRE-mRuby2-bGH) TF.inert_1.8kb EFS-rtTA-P2A-mGL-WPRE
59	pKG4818	U Tan	LentiX1, EFS-rtTA-P2A-mGL-WPRE TF.inert_1.8kb TRE-mRuby2-bGH
60	pKG4641	D Tan	GA allele, TRE-mCherry-WPRE CAG-rtTA-P2A-mGL-bGH
61	pKG4642	Div	GA allele, (TRE-mCherry-WPRE) CAG-rtTA-P2A-mGL-bGH
62	pKG4643	U Tan	GA allele, CAG-rtTA-P2A-mGL-bGH TRE-mCherry-WPRE
63	pKG4644	Con	GA allele, TRE-mCherry-WPRE (CAG-rtTA-P2A-mGL-bGH)
64	pKG4645	D Tan	GA allele, TRE-VP16-ZF43-P2A-mCherry-WPRE CAG-rtTA-P2A-mGL-bGH
65	pKG4646	Div	GA allele, (TRE-VP16-ZF43-P2A-mCherry-WPRE) CAG-rtTA-P2A-mGL-bGH
66	pKG4647	U Tan	GA allele, CAG-rtTA-P2A-mGL-bGH TRE-VP16-ZF43-P2A-mCherry-WPRE
67	pKG4648	Con	GA allele, TRE-VP16-ZF43-P2A-mCherry-WPRE (CAG-rtTA-P2A-mGL-bGH)
68	pKG4649	D Tan	GA allele, TRE-BEmax-dCas12a-P2A-mCherry-WPRE CAG-rtTA-P2A-mGL-bGH
69	pKG4650	Div	GA allele, (TRE-BEmax-dCas12a-P2A-mCherry-WPRE) CAG-rtTA-P2A-mGL-bGH
70	pKG4651	U Tan	GA allele, CAG-rtTA-P2A-mGL-bGH TRE-BEmax-dCas12a-P2A-mCherry-WPRE
71	pKG4652	Con	GA allele, TRE-BEmax-dCas12a-P2A-mCherry-WPRE (CAG-rtTA-P2A-mGL-bGH)

Table S5: **Plasmids used in PiggyBac-integrated hiPSC supplemental figures.** Text in parentheses indicates a sequence placed in the antisense direction.

Ref	Identifier	Syntax	Construct
72	aRJ137	U Tan	EF1α-TagBFP-syn_pA D1-insulator PGK-mNG-syn_pA E1-insulator
73	aRJ136	D Tan	PGK-mNG-syn_pA D1-insulator EF1α-TagBFP-syn_pA E1-insulator
74	aRJ133	U Tan	D1-insulator EF1α-TagBFP-syn_pA E1-Insulator PGK-mNG-syn_pA
75	aRJ132	D Tan	D1-insulator PGK-mNG-syn_pA E1-insulator EF1α-TagBFP-syn_pA
76	aRJ139	U Tan	D1-insulator EF1α-TagBFP-syn_pA PGK-mNG-syn_pA E1-insulator
77	aRJ138	D Tan	D1-insulator PGK-mNG-syn_pA EF1α-TagBFP-syn_pA E1-insulator
78	aRJ260	Tan	PGK-mNeonGreen D1-CTCF EF1α-TagBFP
79	aRJ261	Tan	PGK-mNeonGreen D1-mutant-CTCF EF1α-TagBFP
80	aRJ262	Tan	PGK-mNeonGreen (E1-CTCF) EF1α-TagBFP
81	aRJ263	Tan	PGK-mNeonGreen (E1-scramble-CTCF) EF1α-TagBFP
82	aRJ264	Tan	PGK-mNeonGreen D1-CTCF (E1-CTCF) EF1α-TagBFP
83	aRJ265	Tan	PGK-mNeonGreen D1-scramble-CTCF (E1-scramble-CTCF) EF1α-TagBFP
84	aRJ266	Tan	PGK-mNeonGreen (E1-CTCF) D1-CTCF EF1α-TagBFP
85	aRJ267	Tan	PGK-mNeonGreen (E1-scramble-CTCF) D1-scramble-CTCF EF1α-TagBFP
86	aRJ211	Tan	PGK-mNeonGreen-syn_pA PGK-TagBFP-syn_pA
87	aRJ212	Tan	PGK-mNeonGreen-syn_pA UbC-TagBFP-syn_pA
88	aRJ213	Tan	PGK-mNeonGreen-syn_pA CAG-TagBFP-syn_pA
89	aRJ214	Tan	EF1α-mNeonGreen-syn_pA EF1α-TagBFP-syn_pA
90	aRJ215	Tan	EF1α-mNeonGreen-syn_pA PGK-TagBFP-syn_pA
91	aRJ216	Tan	EF1α-mNeonGreen-syn_pA UbC-TagBFP-syn_pA
92	aRJ217	Tan	EF1α-mNeonGreen-syn_pA CAG-TagBFP-syn_pA
93	aRJ218	Tan	UbC-mNeonGreen-syn_pA EF1α-TagBFP-syn_pA
94	aRJ219	Tan	UbC-mNeonGreen-syn_pA PGK-TagBFP-syn_pA
95	aRJ220	Tan	UbC-mNeonGreen-syn_pA UbC-TagBFP-syn_pA
96	aRJ221	Tan	UbC-mNeonGreen-syn_pA CAG-TagBFP-syn_pA
97	aRJ222	Tan	CAG-mNeonGreen-syn_pA EF1α-TagBFP-syn_pA
98	aRJ223	Tan	CAG-mNeonGreen-syn_pA PGK-TagBFP-syn_pA
99	aRJ224	Tan	CAG-mNeonGreen-syn_pA UbC-TagBFP-syn_pA
100	aRJ225	Tan	CAG-mNeonGreen-syn_pA CAG-TagBFP-syn_pA
101	aRJ242	Tan	PGK-mNeonGreen-syn_pA Inert-TagBFP-syn_pA
102	aRJ243	Tan	EF1α-mNeonGreen-syn_pA Inert-TagBFP-syn_pA
103	aRJ244	Tan	UbC-mNeonGreen-syn_pA Inert-TagBFP-syn_pA
104	aRJ245	Tan	CAG-mNeonGreen-syn_pA Inert-TagBFP-syn_pA
105	aRJ246	Tan	Inert-mNeonGreen-syn_pA PGK-TagBFP-syn_pA
106	aRJ247	Tan	Inert-mNeonGreen-syn_pA EF1α-TagBFP-syn_pA
107	aRJ248	Tan	Inert-mNeonGreen-syn_pA UbC-TagBFP-syn_pA
108	aRJ249	Tan	Inert-mNeonGreen-syn_pA CAG-TagBFP-syn_pA
109	aRJ210	Div	(PGK-mNeonGreen-syn_pA) EF1α-TagBFP-syn_pA
110	aRJ228	Div	(PGK-mNeonGreen-syn_pA) EF1α-TagBFP-bGH
111	aRJ229	Div	(PGK-mNeonGreen-bGH) EF1α-TagBFP-syn_pA
112	aRJ230	U Tan	EF1α-mNeonGreen-syn_pA PGK-TagBFP-bGH
113	aRJ231	U Tan	EF1α-mNeonGreen-bGH PGK-TagBFP-syn_pA
114	aRJ232	D Tan	PGK-mNeonGreen-syn_pA EF1α-TagBFP-bGH
115	aRJ233	D Tan	PGK-mNeonGreen-bGH EF1α-TagBFP-syn_pA

Caption for Movie S1. Contact probability is animated between the uninduced and induced conditions for hiPSCs integrated with the four syntaxes. For the local region around the integration site, the balanced contact probability without and with induction is shown for each syntax. Dividing the induced probability by the uninduced probability gives fig. S12.

Gene syntax defines supercoiling-mediated transcriptional feedback

Christopher P. Johnstone, Kasey S. Love, Sneha R. Kabaria, Ross D. Jones, Albert Blanch-Asensio, Deon S. Ploessl, Emma L. Peterman, Rachel Lee, Jiyoung Yun, Conrad G. Oakes, Christine L. Mummery, Richard P. Davis, Brandon J. DeKosky, Peter W. Zandstra, and Kate E. Galloway

Science **392** (6797), eadw1925. DOI: 10.1126/science.adw1925

Editor's summary

Transcription reshapes DNA folding within living cells, driving patterns of gene expression. However, this process remains poorly understood, which limits the effectiveness of gene circuits for therapeutic applications. Johnstone *et al*. investigated how transcription generates DNA supercoiling (changes in DNA twist) and how these emergent structures tune the expression of adjacent genes. They found that altering gene syntax, defined by the relative order and orientation of neighboring genes, changed DNA supercoiling and affected both the level and variability of gene expression. This work helps explain patterns of natural gene regulation and may improve the design of gene therapies.
—Di Jiang